ACRES TO ANGSTROMS: CROSS-SCALE STUDIES OF SOIL ORGANIC-MATTER MINERAL INTERACTIONS

A Dissertation

Presented to the Faculty of the Graduate School

of Cornell University

In Partial Fulfillment of the Requirements for the Degree of

Doctor of Philosophy

by

Michael Schmidt

August 2018

ACRES TO ANGSTROMS: CROSS-SCALE STUDIES OF SOIL ORGANIC-MATTER MINERAL INTERACTIONS

Michael Schmidt

Cornell University 2018

Dissolved organic matter (DOM) adsorption on minerals plays an important role in many functions of soils, including the retention of carbon by soils. These interactions exist across scales in the environment, with implications from field to molecular levels. Work spanning these scales is presented, highlighting DOM dynamics in agricultural soils under different management as well as laboratory based studies of model biomolecule-mineral interactions. Field level studies show the amount and characteristics of DOM differ greatly between surface and subsoils. Observed depth trends in DOM are influenced by tillage, with tilled soils exhibiting two discreet distributions in DOM characteristics. A punctuated change from sorptive partitioning of surface DOM inputs to source driven DOM dynamics in subsoils is observed in tilled systems with no-till soils showing a gradual transition between the two. Molecular-level studies of protein (bovine serum albumin (BSA)) and nucleic acid (deoxyribonucleic acid (DNA)) interaction with the common soil minerals montmorillonite and goethite demonstrate the interplay between biomolecular characteristics and the kinetic, equilibrium and conformational aspects of adsorption. Furthermore, studies were conducted with both BSA and DNA in solution together. Under these conditions, assembly of BSA and DNA in solution is shown to impact the

mechanism and quantity of biomolecule adsorption on goethite. These results enhance our understanding of organic matter interaction with soils at two distinct scales, both through probing DOM transformation in agricultural soils and mechanistic studies of biomolecule adsorption on minerals.

BIOGRAPHICAL SKETCH

Raised in the rural town of Nescopeck in Northeastern Pennsylvania by two nuclear power plant employees, the author had an early curiosity toward the environmental and physical sciences. He followed this interest to Lebanon Valley College in Annville, PA, where he graduated with a B.S. in Chemistry in 2011. It was here where he first became exposed to research through studies of the photocatalytic properties of ZnS quantum dots. Continuing down the path of research, he pursued a Ph.D. in Environmental Soil Chemistry at the Pennsylvania State University to work with Dr. Carmen Enid Martínez on fundamental organo-mineral interactions. He eventually transferred to Cornell University and continued to pursue fundamental research probing organo-mineral interactions. While not doing research, he enjoys fishing in the numerous water bodies around Ithaca and spending time with friends outside.

This work is dedicated to the generations of chemists and soil scientists who have collectively toiled for millennia and whose insights have made these studies possible.

ACKNOWLEDGMENTS

I would like to acknowledge a number of people who helped make graduate school a formative and insightful endeavor. First and foremost, I would like to thank my advisor Dr. Enid Martínez for putting up with me for all of these years and continuing to be a great source of guidance throughout. Without Amrita Bhattacharyya, Aubrey Fine, Fiona Kizewski and Carla Rosenfeld, previous members in my research group, I am not sure how I would have fared early in my Ph.D. program. I'd also like to acknowledge Behrooz Azimzadeh, Tapasya Babu, K. Taylor Cyle and Ariel Mollhagen, more recent member of the research group, for their grounding discussions. Angela Possinger has been a great source of support and sanity, I am extremely thankful to her. For my great friends Vinay Bhaskar, Francis Chen, Liang Cheng, Matt Duffy, Marc Falck, Sonam Sherpa and Dr. Herbert Tobias I am eternally grateful. They were an integral part of making graduate school so much more than the work (it thankfully is). There is no way I would have made it through this without any of these aforementioned exemplary individuals.

TABLE OF CONTENTS

LIST OF FIGURES

LIST OF TABLES

LIST OF ABBREVIATIONS

ATR-FTIR	Attenuated total reflectance-Fourier transform infrared
BSA	Bovine serum albumin
CD	Circular dichroism spectroscopy
DNA	Deoxyribonucleic acid
DOM	Dissolved organic matter
EEM	Excitation-emission matrix
FTIR	Fourier transform infrared spectroscopy
GAE	Gallic acid equivalents
MB	Moldboard plowed
NT	No-till
SEM	Scanning electron microscopy
UV/Vis	Ultraviolet/visible spectrophotometry
XANES	X-ray absorption near edge structure
XPS	X-ray photoelectron spectroscopy

PREFACE

"The White Rabbit put on his spectacles. 'Where shall I begin, please your Majesty?' he asked.

'Begin at the beginning,' the King said, very gravely, 'and go on till you come to the end: then stop.'

There was dead silence in the court, whilst the White Rabbit read out these verses:-"

-Lewis Carroll, *Alice's Adventures in Wonderland*

CHAPTER ONE

The Influence of Tillage on the Dynamics of Dissolved Fractions in a Mid-Atlantic Agroecosystem

1. Introduction

Dissolved organic matter (DOM) serves important roles in many key biogeochemical processes within soils.[1,2] For example, DOM is an important substrate for microbial and plant growth, providing carbon, nitrogen, sulfur, potassium and phosphorus necessary for cellular function. DOM also mediates the transport of these constituent elements in soils.[3] Of specific relevance to macronutrient biogeochemistry is the movement of DOM from surface soils into the subsoil and subsequent retention of C and N by the soil matrix.[4] As these fractions move through the soil profile, they may be continually subjected to various modification, influencing the amount and characteristics of DOM in solution, generally resulting in a decrease in DOM with an increase of soil depth. This trend is often attributed to losses of the DOM pool through an interplay of selective adsorption of DOM constituents to the soil matrix, incorporation within minerals during precipitation and microbial processing of DOM, such as decomposition, release and modification of free and mineral-adsorbed DOM.[2,4-8] Differing viewpoints regarding the influence of these different processes, and the subsequent dynamics of DOM in soils, have been posited in the literature. It has been proposed that DOM behavior in solution is controlled by continuous, chromatographic partitioning, with strongly adsorbing components of DOM (i.e. DOM constituents with high molecular weight, more hydrophobic character and

enriched in aromatic, phenolic and carboxylic functionalities) selectively removed, while DOM constituents less likely to adsorb move deeper in soil profiles and eventually leach out into groundwater.[9] Alternatively, microbial transformation of adsorbed and mineral-incorporated DOM has been proposed to play an important role in DOM behavior in soils through release of previously retained DOM from plant and microbial inputs through processing and displacement of retained material.[6] This model results in more plant derived DOM near the surface with microbial byproducts being the dominant components in subsoils. Together, all of these points highlight the importance of the mobile DOM fraction to the ecological functioning of soils and its dynamic nature throughout soil profiles.

Given the dynamic nature of DOM fractions in soils, these species are sensitive to soil management practices, including tillage, amendment addition and extent of soil drainage.[1] Particularly, DOM dynamics have been linked to tillage practices in agroecosystems. Tillage has been observed to alter the amount of DOM in soils, with tillage typically associated with lower amounts of DOM in surface soils compared with no-till soils.[1] This has been attributed to greater renewal of DOM by larger bulk soil organic matter stocks observed in no-till soils.[10] Not all studies, however, show this result, with tillage shown to have no impact or a positive response of DOM concentration to tillage due to enhanced microbial degradation of plant residues.[11] Similar to previous studies on DOM concentration, analyses of tillage influence on DOM molecular composition have yielded mixed results. A previous nuclear magnetic resonance (NMR) and pyrolysis field ionization mass spectrometric study demonstrated a relative increase in carbohydrate, lignin monomer and phenolic species

within a water soluble, hydrophobic resin fractionated DOM fraction in a surface soil tilled regularly compared with a soil converted to a grassland.[12] These observed differences were tied to more rigorous microbial activity and decomposition of plant residues under more intense cultivation. Recent UV/visible and fluorescence spectrometric characterization of DOM extracted from till and no-till soils to a depth of 30 cm suggested that tillage increases the proportion of decomposed and condensed aromatic structures relative to no-till agriculture.[13] Another study, however, showed no significant difference between fluorescence landscapes of DOM extracted from till and no-till surface soils, suggesting the molecular characteristics of DOM are similar.[14] As is evident from variation in previous results and present gaps in our understanding of DOM dynamics with respect to tillage practices, further study is needed to assess the potential influence of tillage on these critical soil components. Furthermore, existing studies focus primarily on surface soils to plow layer depth, rendering studies of the behavior of these mobile species and their associated organic matter in subsoils, where transformations of DOM associated organic matter may propagate, particularly scarce.

The objective of this study is to probe the influence of tillage on dynamics of organic matter associated with DOM fractions throughout agricultural soil profiles. To address this objective, DOM was isolated from five depth intervals up to 72 cm depth. Soils used in this study are part of a long term (40 years) tillage experiment and represent no-till and conventional tillage management practices. C and N within DOM isolated throughout profiles were measured to assess the quantitative implications of tillage on organic matter in these fractions. Furthermore, 0.2 μm extracts were further

characterized by UV/visible spectrophotometry to target the relative aromaticity of these components and by Fourier transform infrared spectroscopy (FTIR) to identify select organic functional groups and mineral constituents. Lastly, the 0.2 μm DOM fractions were probed by fluorescence excitation emission scans to infer sources and partitioning of DOM at sampled depth intervals. These data, interpreted in conjunction with bulk soil properties (i.e. C/N, mineralogy, texture, organic matter functional group composition), are used to develop a novel perspective on the influence of tillage on DOM dynamics throughout the soil profile.

2. Materials and Methods

2.1 Study site and soil sampling. Soil samples were collected from tillage treatment plots initiated in 1978 at the Pennsylvania State University Russell E. Larson Agricultural Research Center in Rock Springs, PA. Two plots were selected for use in this study (40°42′46”N, 77°58′11”W), a plot managed under no-till management (NT) and a plot maintained under moldboard tillage (MB) to a depth of about 20 cm. Soils on these plots are dominated by the Hagerstown silt loam (Fine, mixed, semiactive mesic Typic Hapludalf) soil series with certain portions classified as Nolin silt loam (Fine-silty, mixed, active mesic Dystric Fluventic Eutrudepts) soils. Further details regarding climatological data and historical management practices related to these plots can be found elsewhere.[15] Soils were sampled across one plot for each tillage treatment, with a set of three sample cores collected to a depth of 72 cm at three points across each plot (9 soil cores per treatment). 72 cm was selected as this was the shallowest depth to bedrock observed amongst all points sampled. Cores were then

divided into 5 depth increments, 0-12, 12-20, 20-35, 35-50 and 50-72 cm, and pooled with other cores collected at the same point (3 pooled soil cores per treatment). After collection, pooled samples were air dried, ground and passed through a two mm sieve before further analysis.

2.2 Measurement of bulk soil properties.

2.2.1 Soil pH, texture, organic carbon and total nitrogen. Soil pH was measured using a 1:1 soil to water (w:v) ratio. Particle size distribution was determined using the hydrometer method with sodium hexametaphosphate pretreatment to disperse soils.[16] Organic C and total N content of soils were quantified using a Shimadzu Total Organic Carbon Analyzer TOC-5000A (Shimadzu Corp., Kyoto, Japan) equipped with a solid sample module and an infrared detector. Prior to organic C and total N analysis, soils were ball milled to a fine powder and pre-treated with 2 N HCl at 80°C to remove any inorganic C species potentially present.

2.2.2 Selective extraction of Fe and Al species. Selective extraction of Fe and Al from soils were performed to estimate the quantity of these elements in three fractions: the free (non-silicate) crystalline, poorly-crystalline and organically bound forms of these elements. Prior to performing these extractions, soils were ball milled to a fine powder. Dithionite-citrate extraction of soils, extracting free (non-silicate), crystalline and non-crystalline forms of bound elements, was performed as described previously.[17] Briefly, 25 mL of 0.68 M sodium citrate solution and 0.4 g of sodium dithionite were added to 0.500 g of finely ground soil in a 50-mL centrifuge tube and shaken overnight. The suspension was then centrifuged at 510 rcf for 20 minutes. Collected supernatant was then diluted by a factor of 40 with doubly deionized water

(18.2 MΩ resistance) before analysis by inductively coupled plasma atomic emission spectroscopy (ICP-AES). The poorly-crystalline forms of Fe and Al were determined using the acid ammonium oxalate method.[18] For this method, 10 mL of a 0.2 M ammonium/acid oxalate solution at pH = 3.0 was added to 0.25 g of soil in a 15-mL plastic centrifuge tube and shaken for 4 hours. Shaking was done in the dark to avoid dissolution of crystalline forms from the soil. After shaking, samples were centrifuged for 10 minutes at 10000 rcf. The supernatant was then diluted 30 times with doubly deionized water prior to elemental determination by ICP-AES. Extraction with sodium pyrophosphate was used to quantify the organically-bound fraction of Fe and Al in soils.[19] 9 mL of 0.1 M sodium pyrophosphate was added to 0.300 g of soil in a 50-mL centrifuge tube, representing a 1:30 soil to extractant ratio (m:v) suitable for soils low in pyrophosphate extractable elements, and shaken overnight. Suspensions were then centrifuged at 20000 rcf for 10 minutes and diluted by 10 before ICP-AES analysis. Crystalline Fe and Al were determined by subtracting the amount of these elements released by acid ammonium oxalate extraction from the amount extracted using the dithionite-citrate procedure. Poorly-crystalline forms of Fe and Al were determined by subtracting the sodium pyrophosphate extracted (organically bound) elements from the amount extracted by acid ammonium oxalate.

2.2.3 Carbon K-edge x-ray absorption near edge structure (XANES) spectroscopy of bulk soils. Carbon K-edge XANES spectra of soils at all depth intervals from two sampling locations within the MB and NT plots were collected at the University of Wisconsin Synchrotron Radiation Center in Stoughton, WI USA. Spectra were collected at the HERMON beamline (port 33) on the 0.8 MeV Aladdin storage ring at

250 mA current under vacuum conditions (<1×10^{-7} Torr). Finely ground samples and standards were prepared for XANES analysis by pressing a few tenths of a gram onto a section of indium foil, which was then affixed to the sample holder using a piece of double-sided adhesive tape. Data collection was performed in total fluorescence yield (TFY) mode with a double stacked multi-plate chevron detector and recorded using a varied-line spacing spherical grating monochromator.[20] All spectra were acquired at a resolution of 0.4 eV from 282 to 305 eV (0.10 eV step-size for samples and 0.25 eV step-size for standards). Entrance and exit slits were fixed at 122 and 360 μm, respectively, providing a 1 mm × 0.72 mm beam spot size. After collection, the TFY signal was divided by the reference channel beam current (I_0), yielding current normalized spectra to account for changes to I_0 across sample scans. Further normalization to the edge jump absorbance between the flat regions of the pre-edge and post-edge was performed. Normalized spectra were then energy calibrated to the gold mesh used for I_0 channel collection. All post-hoc modifications to data were made using Athena.[21] Spectra from MB and NT plots shown represent the average of spectra collected from two sites within each plot.

2.3 DOM isolation and speciation

2.3.1 Isolation of DOM from soils. Soils were combined with doubly deionized water at a 1 to 10 soil to water mass ratio and gently shaken overnight in 50-mL centrifuge tubes on a table shaker. Suspensions were then filtered through 0.2 μm polyethersulfone filters which were pre-rinsed with 200 mL of doubly deionized water. Spectroscopic analyses (i.e. fluorescence, UV/Vis and FTIR) of filtrates were conducted immediately after filtering. Otherwise, samples were stored at -20°C and

subsequently thawed before analysis.

2.3.2 Quantification of carbon and nitrogen in DOM fractions. Non-purgeable organic carbon (NPOC) and total dissolved nitrogen (TDN) were measured on a Shimadzu TOC-$V_{CPH/CPN}$ equipped with a non-dispersive infrared gas analyzer for NPOC determination. TDN determination was by reaction with ozone and chemiluminescent gas analyzer at 720°C N detector. Samples were analyzed using high temperature (720°C) catalytic (Pt) oxidation and were acidified and sparged prior to analysis and detection for DOC by non-dispersive infrared gas analyzer (NDIR).

2.3.3 FTIR spectroscopic measurements. FTIR spectra were collected on a Vertex 70 spectrometer (Bruker Inc., Billerica, MA) equipped with a Pike GladiATR (Pike Technologies, Madison, WI) sampling accessory. A single reflection diamond internal reflection element (IRE) with a diameter of 3 mm was used for sample analysis. Spectra were collected on 6 µL aliquots of extracted DOM which were drop cast and dried under argon gas on the IRE. Between samples, the IRE was cleaned with ethanol and rinsed multiple times with deionized water. Spectra were collected from 4000 – 800 cm^{-1} with 4 cm^{-1} resolution and represent an average of 128 scans. After collection, spectra received an atmospheric compensation, smoothing, baseline correction and normalization. Replicate spectra (n = 3) for each depth and tillage treatment were then averaged. Processing of spectra was performed using OPUS 7.2 software (Bruker, Inc., Billerica, MA).

2.3.4 UV/Visible spectroscopic measurements. UV/Vis spectra of 0.2 µm filtered DOM samples were measured with a Shimadzu UV-Vis 2600 spectrometer using a quartz cell with a 1 cm path length. Spectra were collected from 200-400 nm using a

0.1 s accumulation time and 2.0 nm slit widths against a deionized water background. For determination of the relative aromaticity of DOM extracts, samples were interpreted through specific UV absorbance at 254 nm ($SUVA_{254}$). $SUVA_{254}$ values represent the absolute absorbance of DOM at 254 nm normalized against its NPOC concentration.

2.3.5 Fluorescence spectroscopic measurements. Fluorescence excitation-emission matrices (EEMs) of DOM samples were collected on a Photon Technology International Quantamaster 40 spectrofluorometer (Photon Technology International, Lawrenceville, NJ). A xenon excitation source was used, with emission and excitation slits set to a 5 nm band-pass. The lamp was turned on approximately 30 minutes before data collection to allow for stabilization of the source. An integration time of 0.25s was used for all scans. Signals were internally corrected for wavelength effects and lamp fluctuations. EEMs represent a series of emission scans collected at a series of excitation wavelengths. Excitation wavelengths ranged from 220-450 nm, with emission scans collected at 5 nm steps. Emission spectra were collected from 250-550 nm at a 2 nm step size. The starting wavelength of collected emission scans was offset from the excitation wavelength by 30 nm to remove interference from exciting photons. Prior to collection of fluorescence spectra, DOM samples were diluted to an A_{254} value of <0.10 to reduce influence of the inner-filter effect on spectra. For each day data were collected, a water blank was collected to serve as a background for removing Raman scattering and for normalization of EEMs. EEMs were normalized to the area under the water Raman peak from 383-412 nm at an excitation wavelength of 350 nm. Second-order Rayleigh scattering features were accounted for by deletion of

data at the peak wavelength ± 10 nm. Processed EEMs from each replicate of depth and tillage treatment were averaged (n = 3) after processing.

2.3.6 Determination of free phenols in DOM extracts. Quantification of phenols in DOM extracts was determined using a previously described modification of the Folin-Ciocalteu method.[22,23] To 0.5 mL of DOM extracts, 75 µL of 1.9 M Na_2CO_3 and 25 µL Folin-Ciocalteu reagent were added. Sample and reagents were left for 1 hour to allow color to develop. After this time, samples were analyzed with UV/Vis spectrophotometry and quantified using the peak centered at 760 nm. Concentrations were determined against gallic acid standards, with concentration units of samples given as gallic acid equivalents (GAE).

3. Results

3.1 Bulk MB and NT soil properties

3.1.1 Soil pH and texture. Soil particle size distribution and pH results for the MB and NT soils are shown in **Table 1.1**. Soil textures range from clay loam to silt loam with subsoils generally finer than surface soils. Soil pH between both plots at all depth intervals studied is similar, with a pH around 6.0.

3.1.2 Extractable Fe and Al and clay mineralogy. Crystalline Fe and Al is the most prevalent form of extractable Fe and Al, with concentrations ranging from 48.8-68.9 and 24.4-50.6 mg/g soil, respectively (**Figures A1.1 and A1.2**). Poorly-crystalline and short range forms of Fe and Al represent a smaller proportion of these elements across all depths and tillage plot relative to crystalline species, with concentrations ranging from 4.6-14.2 and 3.0-4.5 mg/g soil for Fe and Al, respectively. Organically-bound Fe

and Al represent the smallest pool of extracted forms in soils from both plots, with concentration ranging from 0.1-0.44 and 0.22-0.38 mg/g soil, respectively for Fe and Al. The 0-12 (0.31 mg/g soil) and 12-20 (0.35 mg/g soil) cm depths are similar in the MB soil, with a sharp decrease in concentration to a fairly constant value in subsoils from 20-72 cm (from 0.10-0.15 mg/g soil). The decrease in the NT soil is a gradual decline from 0.44 mg/g soil at 0-12 cm down to 0.09 mg/g soil at 50-72 cm.

FTIR spectra of bulk soils show features associated with specific crystalline aluminosilicate clay minerals, primarily illite and kaolinite (**Figures A1.3** and **A1.4**). In addition to these clay minerals, FTIR spectra show distinct features attributable to quartz in soils from both the MB and NT plots.

3.1.3 Soil C and N contents. Depth trends for organic C and total N are influenced by tillage, with a homogeneous distribution of C and N within plow layer depth (up to 20 cm) and a sharp decrease to a relatively stable value from all depths downward in MB soils (**Table 1.1** and **Figures 1.1a-b)**. Distribution within the equivalent plow layer depth of 20 cm in NT soils is distinct from the MB soils, with the 12-20 cm depth having lower organic C and N concentration relative to the surface soil (0-12 cm). Unlike the MB soils, the NT soils show a more gradual decrease in organic C and total N below 20 cm depth in addition to differences within the equivalent plow layer depth. The C:N ratio of MB (11.1 at 0-12 cm to 5.7 at 50-72 cm) and NT (12.2 at 0-12 cm to 5.4 at 50-72 cm) soils decreases with depth through these profiles (**Figure 1.1c**). Given the variability in sampled soils, the only depth at which a difference between MB and NT soils is observed is at 0-12 cm, where the NT soil has a higher C:N.

3.1.4 Carbon speciation in tilled and no-till soils. Mean carbon K-edge XANES

spectra of soils at all depths from the MB and NT plots are shown in **Figure 1.2** (individual replicate spectra are shown in **Figure A1.5**). Across all of the spectra, there are three regions and associated transitions of organic carbon functionalities observed: a feature at around 285.2 eV resulting from the aromatic C=C $\pi \rightarrow \pi^*$ transition, a region from 286.5-287.5 eV assigned to C $1s \rightarrow \pi^*$ transitions of substituted/heterocyclic aromatic groups as well as the $1s\text{-}3p/\sigma^*$ of aliphatic C-H moieties, and a peak at around 288.6 eV, which is attributed to amide/carboxylic $1s \rightarrow \pi^*$ transition.[24,25] For spectra from both plots and all depth increments, the two features associated with aromatic C=C, and amide/carboxylic groups are the most pronounced. The relative proportion of these two peaks appears to change modestly with depth in both the NT and MB soils, with the aromatic C=C feature at 285.5 eV becoming generally more pronounced with depth relative to the amide/carboxyl peak at around 288.6 eV. In addition to the subtle depth trend associated with the aromatic C=C and amide/carboxyl peaks, the features associated with the region from 286.5-287.5 eV become more enhanced with depth in MB and NT profiles. This manifests as the appearance of a distinct peak around 287.5 eV and a broad increase in the 286.5-287.5 eV portion of the spectrum of the 35-50 and 50-72 cm MB soils. To a lesser extent in NT subsoils, this region becomes somewhat heightened, gradually occupying a greater proportion of the region between the aromatic C=C peak at 285.5 eV and the amide/carboxyl peak at 288.6 eV with depth.

3.2 Properties of DOM extracted from MB and NT soils

3.2.1 Organic carbon and total nitrogen in DOM fractions from MB and NT profiles. Water extractable, non-purgeable organic carbon (NPOC) and total nitrogen (TN)

concentrations for the < 0.2 μm fraction are shown in **Figures 1.3a** and **b**. For both MB and NT soils, the amount of NPOC and TN extracted within the < 0.2 μm DOM fraction decrease with depth. The trend in decrease is similar to that observed for bulk organic C and total N contents, with tillage homogenizing the amount of DOM within the plow layer of MB soils, 0.12 and 0.13 mg NPOC/g soil for 0-12 and 12-20 cm, respectively, followed by a sharp decrease to a relatively constant value in subsoils (0.05-0.04 mg C/g soil). Unlike the MB soils, the amount of NPOC and TN associated with the < 0.2 μm DOM fraction of NT soils follows a relatively gradual decrease. NT soils contain < 0.2 μm extractable NPOC concentrations of 0.24, 0.14 and 0.07 mg C/ g soil at 0-12, 12-20 and 20-35 cm depth, respectively, below which concentrations remain fairly stable (0.05 and 0.04 mg NPOC/g soil at 35-50 and 50-72 cm). Total N in this fraction between MB and NT soils at all depths sampled follows a similar trend, but with overall lower concentrations than NPOC. The MB soils had average water extractable TN concentrations of 0.013 and 0.014 mg N/g soil at 0-12 and 12-20 cm depth and values of 7.6×10^{-3}, 9.5×10^{-3} and 9.1×10^{-3} mg N/g soil at 20-35, 35-50 and 50-72 cm, respectively. NT soils have mean TN contents in the water extractable < 0.2 μm fractions of 0.029, 0.015, 8.5×10^{-3}, 4.5×10^{-3} and 5.3×10^{-3} mg N/g soil at 0-12, 12-20, 20-35, 35-50 and 50-72 cm depths, respectively.

3.2.2 UV/Visible spectrophotometric analysis of < 0.2 μm DOM fractions. $SUVA_{254}$ values of the < 0.2 μm extracts from MB and NT soils show a decrease with soil depth, suggesting DOM becomes relatively depleted in aromatic constituents in subsoils relative to surface soils under both moldboard plowing and no-till management (**Figure 1.4**). For MB soils, the decrease follows a similar trend to other

measured soil properties (bulk soil organic carbon and total nitrogen, extractable DOM), with the 0-12 and 12-20 cm soils yielding $SUVA_{254}$ values of 1.35 and 1.32 L mg^{-1} C m^{-1}, respectively. Values then decrease sharply to 0.61 (20-35 cm), 0.52 (35-50 cm) and 0.58 (50-72 cm) L mg^{-1} C m^{-1}. While the NT soils show a somewhat more gradual decrease in $SUVA_{254}$ values with depth, (1.60 (0-12 cm), 1.33 (12-20 cm), 0.86 (20-35 cm), 0.52 (35-50 cm) and 0.48 (50-72 cm) L mg^{-1} C m^{-1}), these values are largely similar given the variability of values.

3.2.3 FTIR spectroscopy of DOM fractions. Mean FTIR spectra (4000-800 cm^{-1}) of < 0.2 μm DOM fraction from MB and NT soils at all depths show vibrations tentatively assigned to both organic and inorganic constituents of the dissolved fraction (**Table A1.1, Figure 1.5**).[26,27] For both soils, peaks unambiguously associated with organic functionalities become relatively lower in intensity with depth relative to peaks attributable to inorganic species (ν N-O of NO_3^- at ≈1355 and ν S-O of SO_4^{2-} at 1100 cm^{-1}). In the spectra from DOM within the plow layer (0-12 and 12-20 cm) of MB soils, a peak assigned to ν C-C/ ν C-O of polysaccharides and polysaccharide-like organic matter is apparent at 1040 cm^{-1}, but is not apparent at depths below this point. In addition to the feature at 1040 cm^{-1}, other features associated with organic functional groups exhibit changes with soil depth in the MB extract, mainly the amide/ketone ν C=O region from 1660-1630 cm^{-1}, the ν_{as} COO^-/ ν C=C feature at around 1600 cm^{-1} and the ν_s COO^- peak at 1415 cm^{-1}. Namely, the ν_s COO^- peak becomes relatively more intense with depth relative to the other organic vibrations ranging from 1660-1600 cm^{-1}, suggesting an enrichment of carboxylate functionalities in DOM extracted from subsoils relative to other groups. This is corroborated by the

behavior of the ν_{as} COO^- peak at 1600 cm^{-1} at corresponding depths, which becomes enhanced relative to other features in the 1660-1600 cm^{-1} region. While the peak at 1600 cm^{-1} is not solely attributed to carboxylate stretching, the other contributing vibrational mode (aromatic ν C=C) is unlikely to be contributing to a relative increase in peak intensity with depth given the inverse relationship between soil depth and $SUVA_{254}$.

Relative to the MB DOM extracts, FTIR spectra of DOM extracts from NT soils show a relative increase of COO^- related features and decrease of polysaccharide-like ν C-C/ν C-O modes with depth. The presence of a distinct peak at 1040 cm^{-1} extends beyond the equivalent plow layer depth to the 20-35 cm depth interval. The transition to a more carboxylate-rich DOM is also more gradual in the NT profile. Increasing of the ν_s COO^- peak intensity relative to the broad region from 1660-1600 cm^{-1} (containing amide/ketone ν C=O, aromatic ν C=C and ν_{as} COO^- modes) occurs throughout the subsoil as opposed to an abrupt transition delineated by the plow layer.

3.2.4 Fluorescence excitation emission matrices (EEMs) of DOM fractions.

Normalized fluorescence EEMs of < 0.2 μm DOM extracts from both NT and MB soils have 4 primary regions in the fluorescence landscape (**Figure 1.6**). Designated regions 1, 2, 3 and 4 with peaks centered at $220_{ex}/296_{em}$, $220_{ex}/386\text{-}414_{em}$, $265_{ex}/300_{em}$ and $310_{ex}/392\text{-}420_{em}$, respectively, can be assigned to specific fluorescent components of DOM. Region 1 ($220_{ex}/296_{em}$) corresponds with fluorescence of DOM derived from microbiota and soluble microbial byproducts (e.g. proteins, nucleic acids, organic acids, polysaccharides) (Aiken, 2014; Coble, 2007). Regions 2 ($220_{ex}/386\text{-}414_{em}$) and 4 ($310_{ex}/392\text{-}420_{em}$) are located in a portion of the fluorescence landscape often

attributed to conjugated fluorophores (previously linked with high molecular weight, humic and fulvic acid-like constituents from plant sources), resulting in red-shifted fluorescence.[28-30] Region 3 ($265_{ex}/300_{em}$) fluorescence is often attributed to fluorescence of simple phenols, aromatic proteins, nucleic acids and other molecules with single-ring aromatic structures.[28-31]

EEMs of DOM extracts from the MB soils show a few notable trends with depth. Generally, the relative proportion of conjugated fluorophoric constituents of DOM decreases with depth, as indicated by a decrease in region 2 and 4 fluorescence intensities in subsoil extracts relative to surface soil extracts. In addition to becoming lower in intensity, the primary region 4 peak emission wavelength becomes increasingly blue-shifted with soil depth. Accompanying the region 4 fluorophores within DOM at increasing soil depth is a relatively higher proportion of region 1 and 3 peaks.

EEMs of DOM extracted from NT soils show a greater contribution from region 2 and 4 peaks in the surface soils (0-20 cm) than DOM from the MB system. Despite the greater proportion of conjugated fluorescent DOM components, the overall decreasing trend of these features with soil depth is analogous to the trend observed in MB DOM extracts. The change in the fluorescence landscape, however, appears more gradual in the NT DOM relative to the MB extracts. This is shown through region 2 and 4 features remaining more intense up to the 35-50 cm depth increment relative to the MB DOM extracts, which show a sharper decrease in these features, particularly region 4 fluorescence, below the plow layer. Region 1 and 3 fluorescent components undergo a similar proportional increase in subsoil DOM to

that observed in the MB soils, albeit in a more gradual fashion.

3.2.5 Phenolic constituents of DOM. NPOC-normalized concentration of phenols extracted in the DOM fractions from all MB and NT soils are shown in **Figure 1.7**. Quantification of phenols within DOM fractions isolated from NT and MB soils by the Folin-Ciocalteu procedure indicates that phenolic constituents do not change concentration substantially throughout the soil profile for either the NT or MB soils given the variability of values observed.

Discussion

4.1 *Bulk soil properties*

4.1.1 *Tillage influence on organic C, total N, C:N ratio and organic matter speciation of bulk soils.* Depth distribution of organic C and total N contents of MB and NT soils follow a general trend commonly observed when comparing till and no-till soils. Incorporation of crop residue through tillage, as was practiced on the MB plot, may explain this result through dilution of residues throughout the plow layer and spatially diluting residue inputs relative to no-till systems, leading to a more gradual decrease in organic C and total N with depth in the NT soils. The observed decrease in C:N ratios with depth is also a commonly observed trend and is often linked with a larger proportion of decomposed organic matter and an enrichment of microbial biomass and byproducts in subsoils relative to surface horizons.[32,33] The higher C:N ratio in the NT 0-12 cm soil versus the MB 0-12 cm soil corresponds with previous results showing a higher C:N ratio in a surface no-till soil than tilled soil.[34] These authors suggest that this is the result of either a higher concentration of crop residue in the surface soil or

lower decomposition of organic matter under no-till management.

Speciation of organic matter associated with MB and NT soils at all depths shows prominent features associated with carboxylic and aromatic functionalities, suggesting their prevalence in these soils. Recent work characterizing soil organic matter using XANES shows a similar prominence of these functional groups in the clay fraction from a pasture soil.[35] The relative increase in the peak associated with aromatic transitions relative to amide/carboxylic transitions suggests an increase in aromatic functionalities in subsoils relative to amide/carboxylic groups. Enrichment of aromatic functionalities of organic matter from subsoils relative to surface soils has been observed previously using various spectroscopic approaches (i.e. NMR, XANES, FTIR).[35-37] Additionally, the increasing height of substituted/heterocyclic and aliphatic transitions from 286.5-287.5 eV suggests that there is a relative increase in substituted aromatic (e.g. phenolic), heterocyclic and aliphatic functional groups in soil organic matter with depth in the MB and NT soils. An increase of substituted aromatics and heterocyclic character corresponds with the relative increase in the aromatic C=C feature with depth in these soils, as the aforementioned functional groups are related through the presence of aryl structures with conjugated π systems and C=C bonds. Given the development of features in this region with depth in the MB soils, it can be assumed that relative accretion of these functionalities is greater under tillage, which is in line with previous studies suggesting that tillage enhances degradation and microbial processing of organic matter within surface soils, which could lead to conversion of organic matter to aromatic and heterocyclic structures.[38,39] Conversion of organic matter into heterocyclic/aromatic structures may also correspond with the

observed decrease of C:N ratio with depth in both the MB and NT soils, linked to decomposition through microbial processing, which could result in production of aromatic and heterocyclic forms of carbon (e.g. nucleic acids, histidine and tryptophan within proteins).

4.2 *Influence of tillage on DOM isolated from soil profiles*

4.2.1 *Tillage influence on organic C and total N in DOM.* With both NPOC and TN content within the < 0.2 μm DOM fraction, concentrations between MB and NT soils are comparable, with the exception of the 0-12 cm depth. At this depth, NPOC and TN concentrations are notably higher in the NT soil. Surface enrichment of water soluble organic carbon in a no-till versus conventional till soil has been observed in previous work, wherein no till practices were shown to increase dissolved organic carbon (DOC) content by 37% over a conventional tillage (i.e. disking, chiseling and ridging) due to the distinct surface layer of residue present in the no-till system.[40] Similarly to the present study, DOC content of subsoils from this study was not significantly altered by tillage, likely due to a translocation and enhanced breakdown of crop residues, both of which increased DOC levels to near that of the no-till soil.

4.2.2 Influence of tillage on molecular characteristics of DOM. $SUVA_{254}$ results are consistent with a recent study, which shows a decrease in values with depth (up to 30 cm) in both till and no-till systems while not exhibiting a significant difference between tillage managment.[13] A reduction of $SUVA_{254}$ values with depth is often linked with selective depletion of hydrophobic, aromatic moieties from DOM as soil solution percolates downward.[41] Additional support for a relative increase in hydrophilicity of DOM with depth in both soils may be found in the FTIR results,

which suggest that carboxylate groups within DOM become relatively more prevalent in subsoils relative to surface soils. An enrichment of carboxylate groups in DOM with depth in both soils aligns with previous observations of DOM becoming more hydrophilic with depth as carboxylic groups are considered Brønsted-Lowry acids which donate H^+ at pH values above 3-4. At pH values in proximity to those of the studied soils (≈6.0), carboxylate groups would assume a net negative charge, which increases hydrophilicity and affinity for remaining in the DOM fraction. Fluorescence EEMs also suggest an increase in hydrophilic character of DOM with depth in MB and NT soils. This is supported through a loss of region 2 and 4 peaks (associated with conjugated, high-molecular weight DOM constituents of hydrophobic nature). The primary region 4 peak also becomes increasingly blue shifted with depth in MB and NT DOM, which has been previously linked with a decrease in conjugation of fluorophores and an increase in hydrophilic character of DOM.[42,43] These results also agree with $SUVA_{254}$ values, which highlight an overall decrease in the relative aromaticity of DOM with depth. Combined, these results point to a shift from relatively more hydrophobic components of DOM in surface soils to fewer in subsoils. Furthermore, tillage impacts this transition, as evidenced by surface homogeneity and relatively sharp changes to $SUVA_{254}$ values, FTIR spectra and EEMs of MB DOM extracts compared with DOM from NT soils.

In addition to the increase of hydrophilic character of DOM with depth in the MB and NT soils, FTIR, fluorescence EEMs and phenol determination of DOM can provide further insights into the molecular composition of DOM. The peak at 1040 cm^{-1}, a feature attributable to polysaccharide-like materials, such as hemicellulose and

cellulose of plant matter, is observed to decrease with depth in MB and NT soils. In MB soils, this feature is not apparent below the plow layer depth, suggesting soluble forms of these polymers are confined to the surface in tilled soils. In the NT soils, however, the peak at 1040 cm^{-1} extends deeper into the profile, indicating that soluble plant-derived polysaccharide components of DOM are more mobile in the NT soils. This is corroborated by the decrease in region 2 and 4 fluorescence of EEMs (previously linked with plant-derived materials) with depth in both MB and NT soils. Accompanying the reduction in region 2 and 4 fluorophores within DOM at increasing soil depth is a relatively higher proportion of region 1 and 3 peaks. This suggests that soluble microbial products, such as proteins, nucleic acids and/or simple phenols may represent a larger proportion of the DOM pool in subsoils relative to more conjugated fluorophores. Quantification of phenols within DOM fractions by the Folin-Ciocalteu procedure indicates that phenolic constituents do not change concentration substantially throughout the soil profile (**Figure 1.7**). This suggests that phenolic species, which may contribute to fluorescence in regions 1 and 3, are likely not responsible for the presence of these fluorophores. Other DOM fluorophores, thus, are a probable influence on this trend. More specifically, nucleic acid-like fluorophores are likely impacting the change in fluorescence landscape, as tyrosine is detectable using the Folin-Ciocalteu method.[23] Similar to decrease in region 2 and 4 peaks, the increase of region 1 and 3 fluorophores is more gradual in the NT soils compared with the MB soils, which show a punctuated transition.

4.2.3 Influence of tillage on DOM dynamics in soil profiles The increasing hydrophilic characteristics, decreasing aromatic content and decreasing fluorescent conjugation of

DOM with depth in MB and NT soils align with DOM removal from solution by selective adsorption onto the soil matrix.[9,31,41] Given the presence of surface active crystalline and poorly-crystalline Fe and Al oxides in these soils, selective adsorption of aromatic, high molecular weight DOM constituents onto soil particles is conceivable, as these mineral phases are present.[44] Although certain hydrophilic functional groups, the carboxylate group in particular, have been demonstrated to adsorb strongly to mineral surfaces, hydrophilic species have also been shown to be displaced by the adsorption of more hydrophobic DOM, leading to release from the soil matrix.[45-47] This is perhaps partially responsible for the increase of carboxylate functionalities with depth in MB and NT soils in addition to selective adsorption.

The relative increase in microbially-derived fluorophores with depth, however, does not necessarily agree with adsorptive partitioning. Biomolecular components potentially associated with these fluorophores (i.e. proteins, nucleic acids) are known to adsorb strongly onto a wide range of soil solids, including aluminosilicate clays and Fe/Al oxides, through various binding mechanisms, including inner-sphere coordination, electrostatic interaction and van der Waals forces.[48,49] Through strong adsorption to the soil matrix, it is conceivable that microbial products within DOM present in surface soils would be strongly retained and, hence, would not be transported into subsoils with other, less sorbing DOM constituents. It is also conceivable that the observed microbial-type fluorophores and organic acids are generated *in-situ*, pointing toward more source driven DOM dynamics in subsoils after larger, more hydrophobic aromatics have been removed through selective adsorption. Together, these points reinforce the previously proposed concept of two distinct

influences of DOM control in subsoils, selective adsorption of DOM constituents and microbially driven contributions to the DOM pool when organic inputs are limited.[6]

Based on molecular speciation (FTIR, UV/Vis, fluorescence spectroscopy) of DOM extracts, tillage appears to affect the balance between these influences. UV/Visible spectrophotometry, FTIR and EEMs all suggest that tillage punctuates the transition from the DOM composition of surface soils to that of subsoils, a transition from more conjugated aromatic, plant-like DOM to DOM more enriched in hydrophilic and microbial components. It is understood that tillage enhances the breakdown of plant residues within the plow layer, leading to greater decomposition of plant residues within the plow layer and sorption of decomposition products to the soil matrix. Spectroscopic analysis of DOM from the NT soil profiles reveals transport of these features deeper into the soil relative to MB profile, possibly due to greater proliferation of macroporous networks, and, thus, greater infiltration into subsoils of no-till systems relative to tilled soils.[50] As a result, a gradual transition in supply of relatively fresh inputs from surface soils leads to a more progressive shift to a microbially influenced DOM dynamic in the NT soils relative to the MB soils.

5. Conclusions

While bulk carbon, nitrogen and water extractable forms of these elements are only different between MB and NT soils at the 0-12 cm depth, results from this study show that the influence of tillage extends beyond this surficial layer. Evidence from molecular level speciation of the bulk MB and NT soils and their corresponding DOM extracts suggests that tillage of the surface soil influences subsequent DOM dynamics

and bulk carbon speciation within subsoils through manipulation of surface inputs. Despite the fact that these effects have not had a notable influence, either positively or negatively, on storage of C and N in the studied soil profiles, alteration of DOM processing by tillage could potentially impact the spatial partitioning of C and N in agricultural soils. Given the biochemically persistent nature of microbial byproducts adsorbed on mineral surfaces and their role in retention of organic matter in soils, accelerating the transition of labile inputs to microbial residues could lead to a greater accumulation of C and N in subsoils in tilled versus no-till systems. It is also possible that transport of surface DOM in no-till systems could temporally advance further into the subsoil as progressive depths along the sorptive gradient become increasingly saturated, allowing for DOM transport deeper into subsoils, leading to greater sorptive retention in subsoils. Preservation of macropore structure in the no-till soil could also account for accelerated DOM transport into subsoils, potentially enhancing sorption of DOM by deeper subsoils.

Acknowledgements

Financial support was received through an assistantship provided by the Section of Soil and Crop Sciences at Cornell University. This work is based in part upon research conducted at the Synchrotron Radiation Center, which is primarily funded by the University of Wisconsin-Madison with supplemental support from facility users and the University of Wisconsin-Milwaukee. This work made use of Cornell University Biotechnology Resource Center facilities. M.P.S. would like to thank Mark Bissen and Mary Severson at the University of Wisconsin Synchrotron Radiation Center for

assistance with the collection of XANES spectra. M.P.S. would also like to acknowledge Dr. Ephraim Govere at Penn State University for assistance with collection of ICP data and soil C/N analyses. Taylor Cyle also provided assistance with collection of NPOC and TN analyses of DOM.

Table 1.1 pH, organic carbon, total nitrogen and particle size distributions for MB and NT soils. Standard deviations of values are shown in parentheses.

Moldboard plowed	0-12 cm	12-20 cm	20-35 cm	35-50 cm	50-72 cm
pH	5.98 (0.15)	5.91 (0.11)	5.99 (0.07)	5.92 (0.06)	5.91 (0.05)
Organic carbon content (g/kg)	7.36 (0.54)	7.42 (0.53)	2.59 (0.44)	1.55 (0.36)	1.60 (0.56)
Nitrogen content (g/kg)	0.77 (0.05)	0.80 (0.07)	0.39 (0.04)	0.36 (0.04)	0.33 (0.10)
C to N ratio	9.51 (0.94)	9.29 (1.01)	6.69 (1.28)	4.34 (1.09)	4.87 (2.25)
% Clay	27.88 (8.04)	27.30 (6.52)	35.50 (5.73)	38.83 (9.98)	37.03 (12.52)
% Silt	39.84 (6.07)	41.98 (6.48)	35.42 (7.28)	35.44 (5.00)	32.33 (7.80)
% Sand	32.28 (14.03)	30.72 (11.69)	29.08 (10.85)	25.73 (14.44)	30.63 (19.83)
No-till	0-12 cm	12-20 cm	20-35 cm	35-50 cm	50-72 cm
pH	6.14 (0.11)	6.20 (0.08)	6.20 (0.07)	6.25 (0.04)	6.07 (0.04)
Organic carbon content (g/kg)	13.50 (2.35)	9.14 (3.62)	5.85 (3.09)	2.69 (0.85)	1.69 (0.57)
Nitrogen content (g/kg)	1.29 (0.19)	0.87 (0.25)	0.64 (0.20)	0.41 (0.03)	0.35 (0.05)
C to N ratio	10.49 (2.42)	10.48 (5.14)	9.21 (5.66)	6.58 (2.13)	4.77 (1.73)
% Clay	20.97 (1.60)	24.74 (4.85)	31.35 (10.40)	33.45 (10.25)	36.63 (11.59)
% Silt	62.17 (4.38)	56.44 (5.30)	50.94 (2.57)	44.44 (1.83)	36.53 (4.43)
% Sand	16.86 (3.05)	18.81 (1.13)	17.71 (8.20)	22.10 (9.17)	26.84 (12.90)

Figure 1.1 Soil organic carbon a), total nitrogen b) and c) C to N ratios for MB (blue) and NT (red) soils. Light points represent individual measurements while the darker points connected by lines represent the mean of replicates (n = 3).

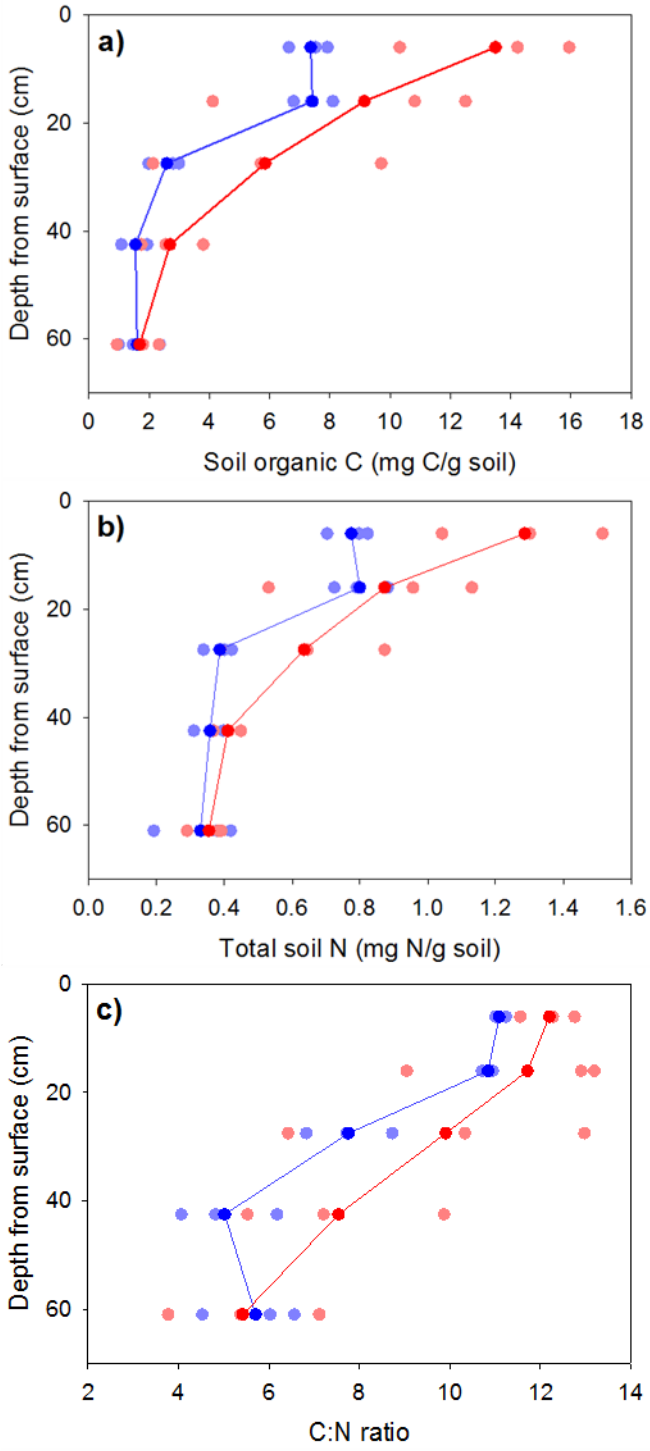

Figure 1.2 Carbon K-edge XANES spectra of soils from all depth increments within MB and NT plots. Dashed lines represent the peak positions for aromatic C=C (285.5 eV, blue), substituted/heterocyclic aromatic (286.5 eV, orange), aliphatic C-H (287.5 eV, green) and carboxyl/amide (288.6 eV, red) functional groups.

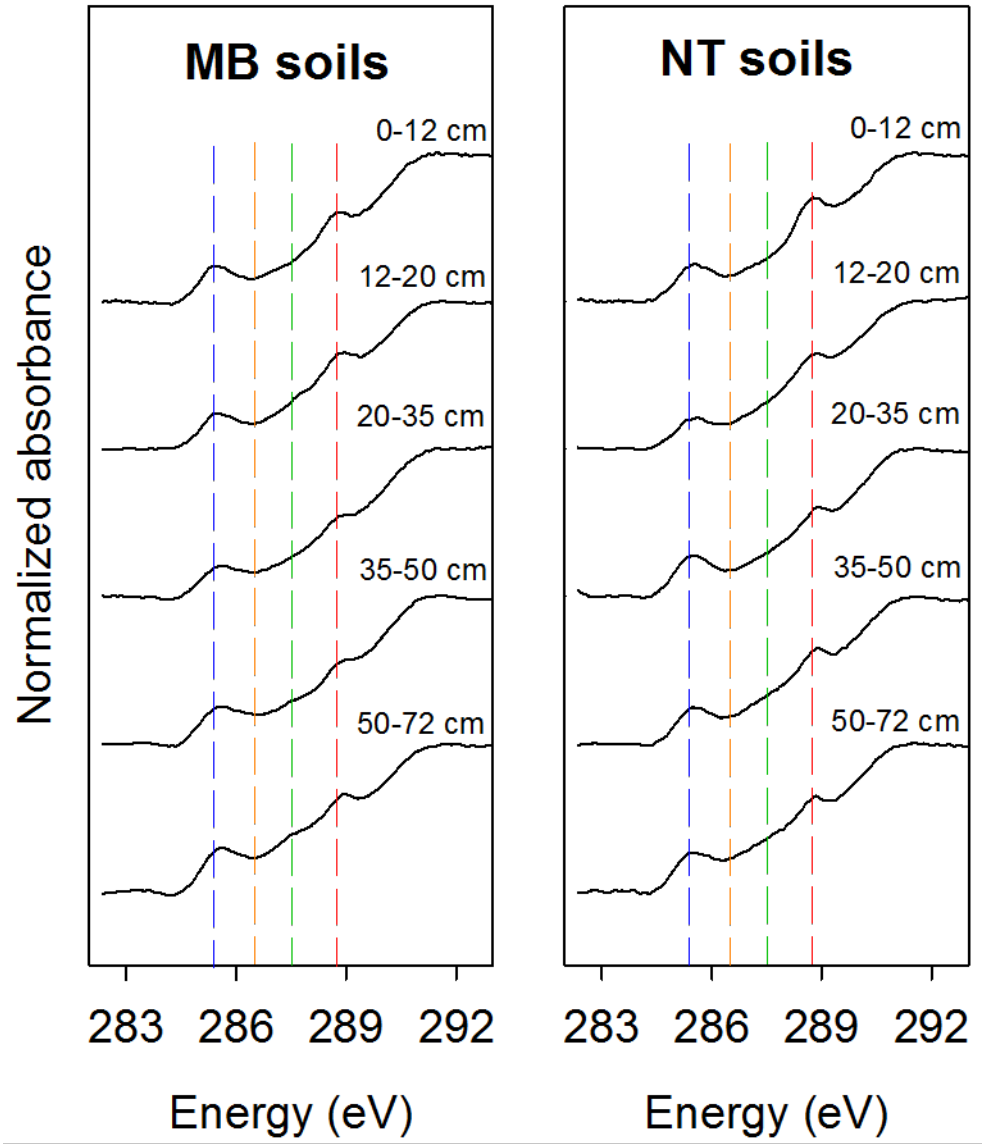

Figure 1.3 a) Non-purgeable organic carbon and b) total nitrogen of the < 0.2 µm water-extractable fractions from MB (blue) and NT (red) plots. Individual replicates are shown by the lighter dots and the mean (n=3) values are represented by the darker dots connected by lines.

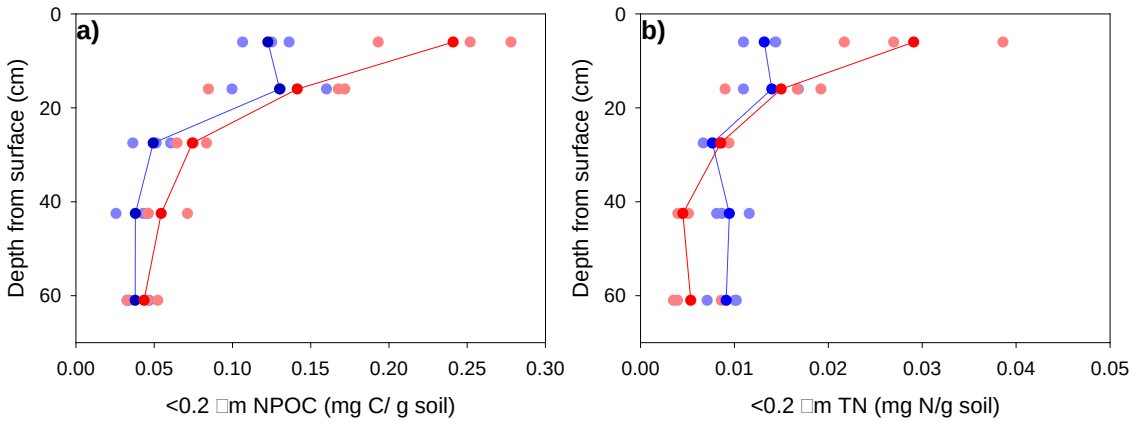

Figure 1.4 $SUVA_{254}$ values for DOM extracts (< 0.2 µm water-extractable fractions) from MB (blue) and NT (red) soils at all sampled depths. Individual replicates are shown by the lighter dots and the mean (n=3) values are represented by the darker dots connected by lines.

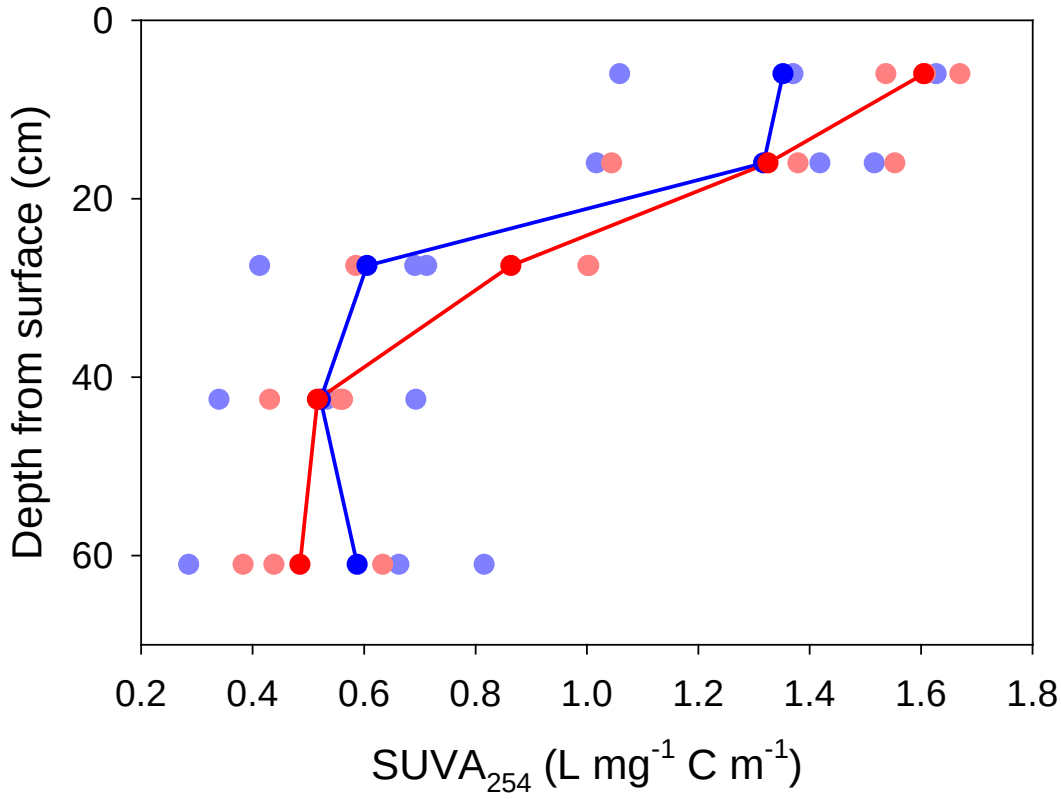

Figure 1.5 Mean normalized FTIR spectra (n=3) of < 0.2 µm water extractable fractions from the MB (left) and NT (right) soils at all depths (solid black line). Gray regions surrounding the spectra represent standard deviation at each wavelength.

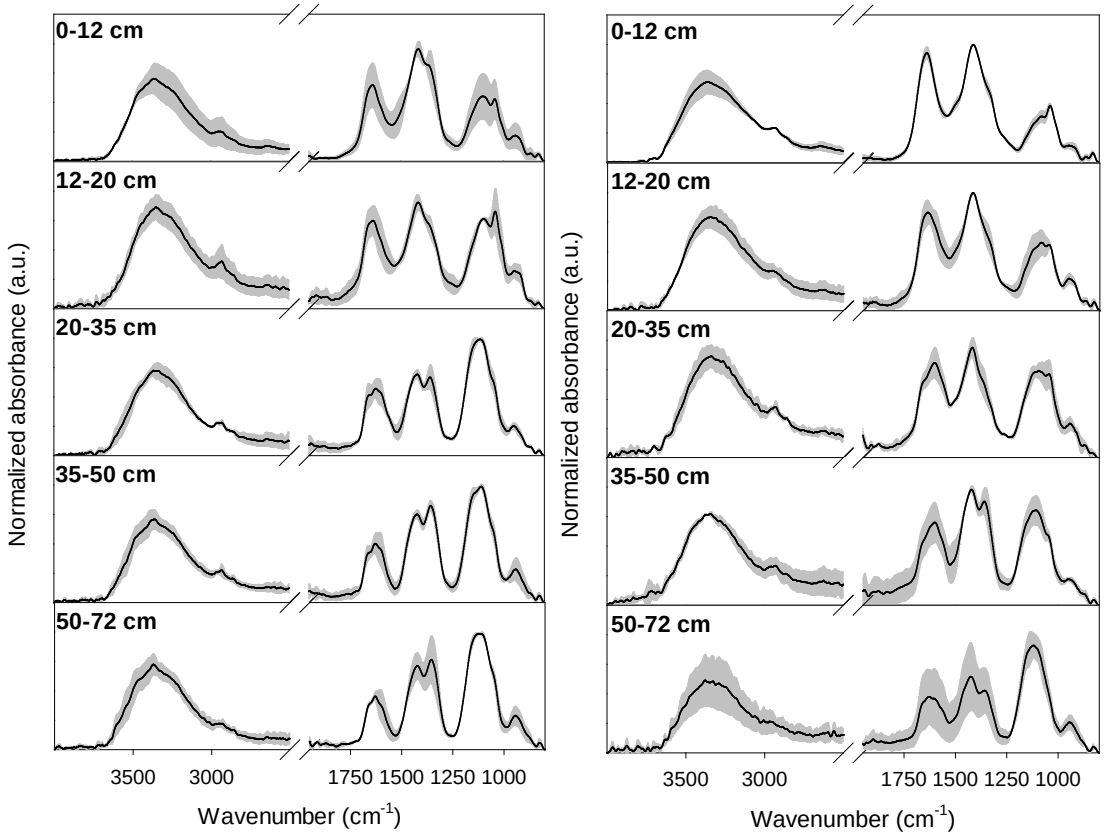

Figure 1.6 Fluorescence EEMs for MB (left) and NT (right) DOM extracts (< 0.2 µm water extractable fractions) at all depths. Primary fluorescence regions are denoted in the 0-12 cm EEMs.

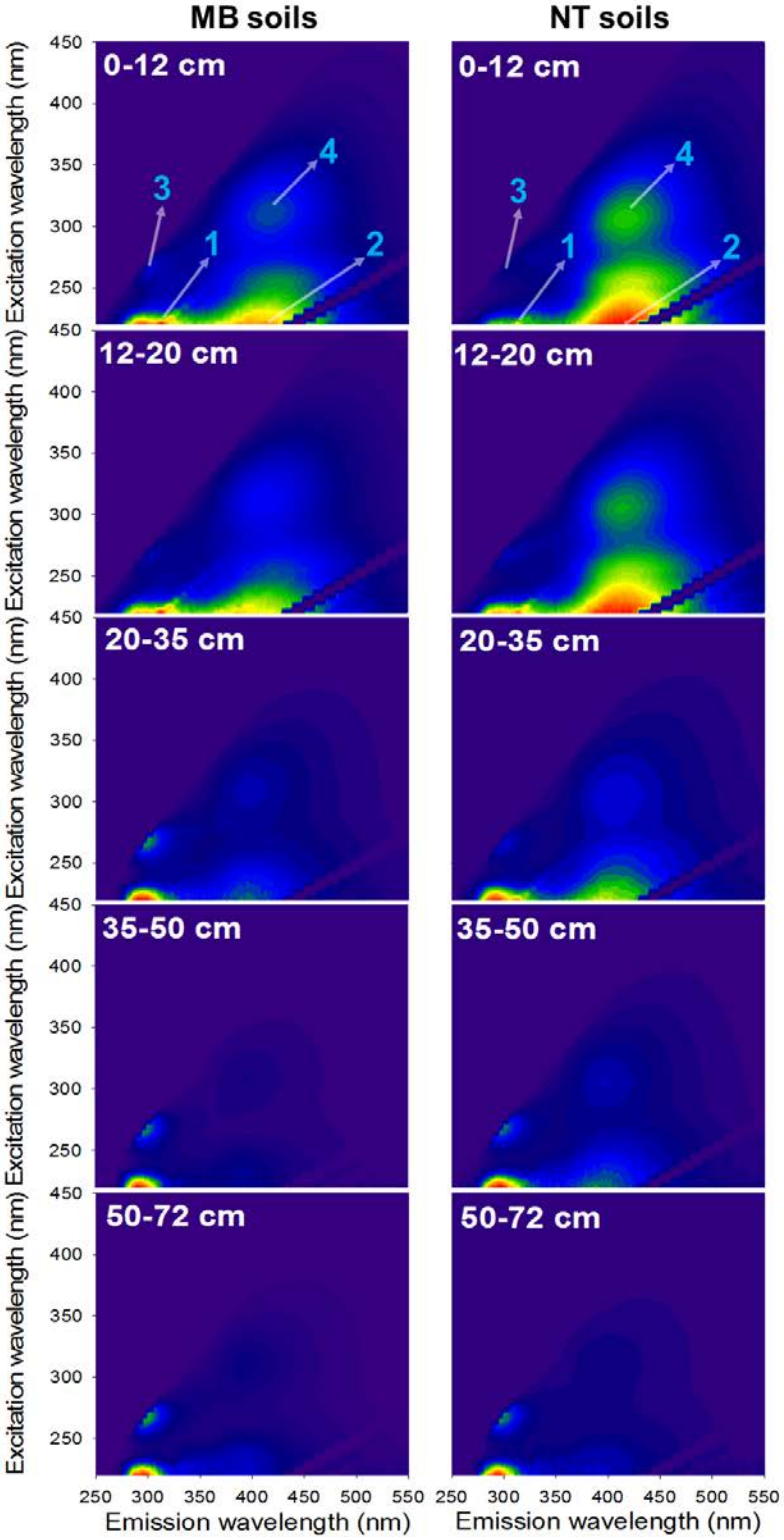

Figure 1.7 Gallic acid equivalent (GAE) concentration normalized against NPOC concentration in DOM extracts from MB (blue) and NT (red) soils. Individual replicates are shown by the lighter dots and the mean (n=3) values are represented by the darker dots connected by lines.

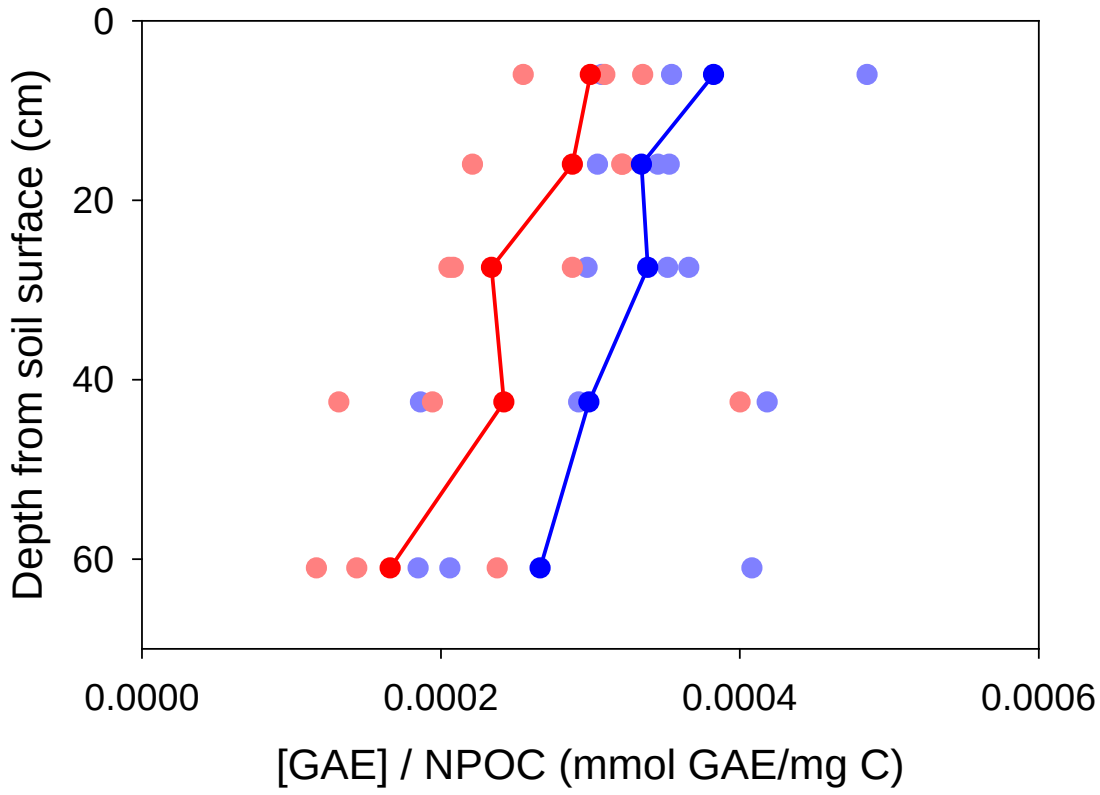

REFERENCES

(1) Chatigny, M.H. Dissolved and water-extractable organic matter in soils: a review on the influence of land use and management practices. Geoderma 2004, 113, 357-380.

(2) Herbert, B.E., Bertsch, P.M., 1995. Characterization of Dissolved and Colloidal Organic Matter in Soil Solution: A Review. In: McFee, W.W., Kelly, J.M. (Eds.), Carbon Forms and Functions in Forest Soils. Soil Science Society of America, Madison, WI, pp. 63-88.

(3) Qualls, R.G.; Haines, B.L.; Swank, W.T. Fluxes of Dissolved Organic Nutrients and Humic Substances in a Deciduous Forest. *Ecology* **1991,** *72,* 578-586.

(4) Kalbitz, K.; Schwesig, D.; Rethemeyer, J.; Matzner, E. Stabilization of dissolved organic matter by sorption to the mineral soil. *Soil Biol. Biochem.* **2005,** *37,* 1319-1331.

(5) Malik, A.; Gleixner, G. Importance of microbial soil organic matter processing in dissolved organic carbon production. *FEMS Microbiol. Ecol.* **2013,** *86,* 139-148.

(6) Kaiser, K.; Kalbitz, K. Cycling downwards – dissolved organic matter in soils. *Soil Biol. Biochem.* **2012,** *52,* 29-32.

(7) Nierop, K.G.J.; Jansen, B.; Verstraten, J.A. Dissolved organic matter, aluminum and iron interactions: precipitation induced by metal/carbon ratio, pH and competition. *Sci. Total Environ.* **2002,** *300,* 201-211.

(8) Torn, M.S.; Trumbore, S.E.; Chadwick, O.A.; Vitousek, P.M.; Hendricks, D.M. Mineral Control of Soil Organic Carbon Storage and Turnover. *Nature* **1997,** *389,* 170-173.

(9) Kaiser, K.; Guggenberger, G.; Haumaier, L. Changes in dissolved lignin-derived phenols, neutral sugars, uronic acids, and amino sugars with depth in forested Haplic Arenosols and Rendzic Leptosols. *Biogeochemistry* **2004,** *70,* 135-151.

(10) Engel, R.E.; Miller, P.R.; McConkey, B.G.; Wallander, R. Soil Organic Carbon Changes to Increasing Cropping Intensity and No-Till in a Semiarid Climate. *Soil Sci. Soc. Am. J.* **2017,** *81,* 404-413.

(11) Gregorich, E.G.; Liang, B.C.; Drury, C.F.; Mackenzie, A.F. Elucidation of the source and turnover of water soluble and microbial biomass carbon in agricultural soils. *Soil Biol. Biochem.* **2000,** *32,* 581-587.

(12) Leinweber, P.; Schulten, H.R.; Kalbitz, K.; Meißner, R.; Jancke, H. Fulvic acid

composition in degraded fenlands. *J. Plant Nutr. Soil Sci.* **2001,** *164,* 371-379.

(13) Romero, C.M.; Engel, R.E.; D'Andrilli, J.; Chen, C.; Zabinski, C.; Miller, P.R.; Wallander, R. Bulk optical characterization of dissolved organic matter from semiarid wheat-based cropping systems. *Geoderma* **2017,** *306,* 40-49.

(14) Ohno, T.; He, Z.; Tazisong, I.A.; Senwo, Z.N. Influence of Tillage, Cropping, and Nitrogen Source on the Chemical Characteristics of Humic Acid, Fulvic Acid, and Water-Soluble Soil Organic Matter Fractions of a Long-Term Cropping System Study. *Soil Sci.* **2009,** *174,* 652-660.

(15) Duiker, S.W.; Beegle, D.B. Soil fertility distributions in long-term no-till, chisel/disk and moldboard plow/disk systems. *Soil Tillage Res.* **2006,** *88,* 30-41.

(16) Sheldrick, B.H., Wang, C., 1993. Particle Size Distribution. In: Carter, M.R. (Ed.), Soil Sampling and Methods of Analysis. Canadian Society of Soil Science, Lewis, Boca Raton, pp. 499-511.

(17) United States Department of Agriculture Soil Survey Laboratory Methods and Procedures for Collecting Soil Samples. United States Government Printing Office (1972)

(18) McKeague, J.; Day, J. Dithionite- and oxalate-extractable Fe and Al as aids in differentiating various classes of soils. *Can. J. Soil Sci.* **1966,** *46,* 13-22.

(19) McKeague, J. An evaluation of 0.1 M pyrophosphate and pyrophosphate-dithionite in comparison with oxalate as extractants of the accumulation products in podzols and some other soils. *Can. J. Soil Sci.* **1967,** *47,* 95-99.

(20) Jokic, A.,; Cutler, J.N.; Ponomarenko, E.; Van der Kamp, G.; Anderson, D.W. Organic carbon and sulphur compounds in wetland soils: insights on structure and transformation processes using K-edge XANES and NMR spectroscopy. *Geochim. Cosmochim. Acta* **2003,** *67,* 2585–2597.

(21) Ravel, B.; Newville, M. ATHENA, ARTEMIS, HEPHAESTUS: data analysis for X-ray absorption spectroscopy using IFEFFIT. *J. Synchrotron Radiat.* **2005,** *12,* 537-541.

(22) Ohno, T.; First, P.R. Assessment of the Folin and Ciocalteu's Method for Determining Soil Phenolic Carbon. *J. Environ. Qual.* **1998,** *27,* 776-782.

(23) Folin, O.; Ciocalteu, V.; On Tyrosine and Tryptophane Determinations in Proteins. *J. Biol. Chem.* **1927,** *73,* 627-650.

(24) Lehmann, J., Brandes, J., Fleckenstein, H., Jacobson, C., Solomon, D., Theime,

J., 2009. Synchrotron-based near-edge X-ray spectroscopy of NOM in soils and sediments. In: Senesi, N., Xing, B., Huang, P.M. (Eds.), Biophysico-chemical Processes Involvin Natural Nonliving Organic Matter in Environmental Systems, IUPAC Series on Biophysico-chemical Processes in Environmental Systems. John Wiley & Sons, Inc., USA, pp. 729-781.

(25) Myneni, S.C.B., 2002. Soft X-ray spectroscopy and spectromicroscopy studies of organic molecules in the environment. In: Fenter, P., Rivers, M., Sturchio, N. (Eds.), Applications of Synchrotron Radiation in Low-temperature Geochemistry and Environmental Sciences, Reviews in Mineralogy & Geochemistry. Vol. 49, pp. 485-579.

(26) Parikh, S.J.; Goyne, K. W.; Margenot, A.J.; Mukome, F.N.D.; Calderón, F.J. Chemical insights provided through vibrational spectroscopy. *Adv. Agron.* **2004,** *126,* 1-112.

(27) Stevenson, F.J., 1994. Humus Chemistry: Genesis, Composition, Reactions. Wiley, USA.

(28) Aiken, G., 2014. Fluorescence and Dissolved Organic Matter: A Chemist's Perspective In: Coble, P.G., Lead, J., Baker, A., Reynolds, D.M., Spencer, R.G.M. (Eds.), Aquatic Organic Matter Fluorescence. Cambridge University Press, New York, NY, pp. 35-74.

(29) Coble, P.G. Marine optical biogeochemistry: the chemistry of ocean color. *Chem. Rev.* **2007,** *107,* 402-418.

(30) Chen, W.; Westerhoff, P.; Leenheer, J.A.; Booksh, K. Fluorescence Excitation-Emission Matrix Regional Integration to Quantify Spectra for Dissolved Organic Matter. *Environ. Sci. Technol.* **2003,** *37,* 5701-5710.

(31) Corvasce, M.; Zsolnay, A.; D'Orazio, V.; Lopez, R.; Miano, T.M. Characterization of water extractable organic matter in a deep soil profile. *Chemosphere* **2006,** *62,* 1583-1590.

(32) Yang, Y.H.; Fang, J.Y.; Guo, D.L.; Ji, C.J.; Ma, W.H. Vertical patterns of soil carbon, nitrogen and carbon:nitrogen stoichiometry in Tibetan grasslands. *Biogeosciences* **2010,** *7,* 1-24.

(33) Callesen, I.; Raulund-Rasmussen, K.; Westman, C.J.; Tau-Strand, L.Nitrogen pools and C:N ratios in well-drained Nordic forest soils related to climate and soil texture. Boreal Environ. Res. 2007, 12, 681-692.

(34) Lou, Y.; Xu, M.; Chen, X.; He, X.; Zhao, K.; Stratification of soil organic C, N and C:N ratio as affected by conservation tillage in two maize fields of China.

Catena **2012,** *95,* 124-130.

(35) Chen, C.; Leinweber, P.; Eckhardt, K.U.; Sparks, D.L. The Composition and Stability of Clay-Associated Organic Matter along a Soil Profile. *Soil Syst.* **2018,** *2,* 16.

(36) Djukic, I.; Zehetner, F.; Tatzber, M.; Gerzabek, M.H.; Soil organic-matter stocks and characteristics along an Alpine elevation gradient. *J. Plant Nutr. Soil Sci.* **2010,** *173,* 30-38.

(37) Ussiri, D.A.N.; Johnson, C.E. Characterization of organic matter in a northern hardwood forest soil by ^{13}C NMR spectroscopy and chemical methods. *Geoderma* **2003,** *111,* 123-149.

(38) Dieckow, J.; Bayer, C.; Conceição, P.C.; Zanatta, J.A.; Martin-Neto, L.; Milori, D.B.M.; Salton, J.C.; Macedo, M.M.; Mielniczuk, J.; Hernani, L.C. Land use, tillage, texture and organic matter stock and composition in tropical and subtropical Brazilian soils. *Eur. J. Soil Sci.* **2009,** *60,* 240-249.

(39) Vairavamurthy, A.; Wang, S. Organic nitrogen in geomacromolecules: Insights on speciation and transformation with K-edge XANES spectroscopy. *Environ. Sci. Technol.* **2002,** *36,* 3050-3057.

(40) Dou, F.; Wright, A.L.; Hons, F.M.; Dissolved and Soil Organic Carbon after Long-Term Conventional and No-Tillage Sorghum Cropping. *Commun. Soil Sci. Plant Anal.* **2008,** *39,* 667-679.

(41) Hassouna, M.; Théraulaz, F.; Massiani, C. Production and elimination of water extractable organic matter in a calcareous soil as assessed by UV/Vis absorption and fluorescence spectroscopy of its fractions isolated on XAD-8/4 resins. *Geoderma* **2012,** *189-190,* 404-414.

(42) Baker, A.; Tipping, F.; Thacker, S.A.; Gondar, D.; Relating dissolved organic matter fluorescence and functional properties. *Chemosphere* **2008,** *73,* 1765-1772.

(43) Coble, P.G. Characterization of marine and terrestrial DOM in seawater using excitation-emission spectroscopy. *Mar. Chem.* **1996,** *51,* 325-246.

(44) Coward, E.K.; Ohno, T.; Plante, A.F. Adsorption and Molecular Fractionation of Dissolved Organic Matter on Iron-Bearing Mineral Matrices of Varying Crystallinity. *Environ. Sci. Technol.* **2018,** *52,* 1036-1044.

(45) Whitehead, C.F.; Carbonaro, R.F.; Stone, A.T. Adsorption of Benzoic Acid and Related Carboxylic Acids onto FeOOH (Goethite): The Low Ionic Strength Regime. *Aquat. Geochem.* **2015,** *21,* 99-121.

(46) Kubicki, J.D.; Schroeter, L.M.; Itoh, M.J.; Nguyen, B.N.; Apitz, S.E. Attenuated total reflectance Fourier-transform infrared spectroscopy of carboxylic acids adsorbed onto mineral surfaces. *Geochim. Cosmochim. Acta* **1999,** *63,* 2709-2725.

(47) Kaiser, K.; Zech, W. Rates of Dissolved Organic Matter Release and Sorption in Forest Soils. *Soil Sci.* **1998,** *163,* 714-725.

(48) Schmidt, M.P.; Martínez, C.E. Ironing out Genes in the Environment: An Experimental Study of the DNA-Goethite Interface. *Langmuir* **2017,** *33,* 8525-8532.

(49) Barral, S.; Villa-García, M.A.; Rendueles, M.; Díaz, M. Interactions between whey proteins and kaolinite surfaces. *Acta Materialia* **2008,** *56,* 2784-2790.

(50) Edwards, W.M.; Norton, L.D.; Redmond, C.E. Characterizing macropores that affect infiltration into nontilled soil. *Soil Sci. Soc. Am. J.* **1988,** *52,* 483-487.

CHAPTER TWO

Kinetic and Conformational Insights of BSA Adsorption onto Montmorillonite Revealed Using *In-Situ* ATR-FTIR/2D-COS

Introduction

Behavior of proteins is relevant to a variety of scientific fields, including biochemistry, engineering, materials science, catalysis and environmental science. In environmental systems proteins are secreted as a result of biological activity or released by organisms upon cellular lysis.[1] Proteins play an important role in a number of environmental processes that are essential to soil and ecosystem health, including the cycling of contaminants and nutrients, impacting the overall health of biota in soils.[1] Proteins have been hypothesized to form the basis of stabile organo-mineral associations in soils, representing the largest stabilized terrestrial carbon pool on Earth.[2,3] Adsorption of proteins onto mineral surfaces has been observed to influence both protein movement and activity in soils, and thus protein function.[1,4] Although the composition of soil mineral surfaces is diverse, the particular impact of protein adsorption onto aluminosilicate clay minerals on the environmental behavior of proteins is apparent.[1,4-6] The high affinity of proteins for layered aluminosilicate clays, relative to other soil minerals, arises from properties unique to layered aluminosilicate clays. The permanent structural charge, high reactive surface area and prevalence in soils of layered aluminosilicate clays (e.g. mica, smectite, vermiculite) are inherent traits that yield a considerable adsorption capacity for a variety of ions and molecules, including proteins.[2, 7-8]Adsorption may be driven by a multitude of forces, including cation exchange, van der Waals, electrostatic interactions, hydrogen bonding and hydrophobic interactions.[9-11] Adsorption of proteins onto layered aluminosilicate clay

minerals, like protein adsorption at solid surfaces in general, is influenced by many conditions.[7] Surface and protein species present, pH, ionic strength and species of interlayer cations, if applicable, are all understood to influence these forces, leading to a system with simultaneously interacting kinetic, structural and thermodynamic controls.[12]

Advancements in analytical capacity have shed some light on the kinetic, structural and thermodynamic aspects of protein adsorption onto clay minerals, enhancing our general understanding of the process. Various microscopic and spectroscopic experiments, utilizing techniques such as atomic force microscopy (AFM),[13,14] quartz crystal microbalance (QCM),[14] Fourier transform infrared spectroscopy (FTIR),[9,15,16] and fluorescence spectroscopy[17] have all been utilized to probe protein adsorption onto aluminosilicates. Taken together, these studies demonstrate surface coverage (i.e. sub-monolayer, monolayer, multilayer), adsorption kinetics (i.e. surface or mass transfer), adsorbed protein assembly and adsorbed protein secondary structure all possibly change to varying extent throughout the protein adsorption process onto aluminosilicates.[9,12-19] For example, it was recently identified that ovalbumin, lysozyme and ovotransferrin assume different orientations throughout adsorption onto synthetic smectite.[14] Furthermore, orientation and aggregation of these proteins is influenced by pH.[14] A previous study probing betalactoglobulin adsorption onto montmorillonite quantifies the strong adsorption affinity ($K= 8.7 \times 10^5 M^{-1}$) while demonstrating loss of β-sheets in betalactoglobulin upon adsorption.[17] Adsorption of *Bt* toxin onto montmorillonite and kaolinite was observed to follow surface controlled adsorption rates[20], while another experiment

probing ovine prion proteins onto mica determined adsorption rates were mass-transfer limited.[19] Drawing comparisons across these different studies can be confounded by the sensitivity of protein adsorption to aforementioned influences, which vary across the literature. Concurrent observation of adsorption kinetics, thermodynamics and structural state of adsorbed protein is not possible with many present experimental approaches, due to the difficulty of simultaneously acquiring quantitative, surface sensitive conformational and surface coverage parameters. Moreover, the dynamic nature of protein adsorption to surfaces warrants observation of the adsorption in real time to comprehensively determine adsorption mechanisms. Future research and present interpretation of protein adsorption onto aluminosilicate minerals, and solid surfaces in general, would benefit greatly from an approach that reconciles this need.

These limitations can potentially be overcome by use of *in-situ* attenuated total reflectance infrared (ATR-FTIR) spectroscopy.[21] Under the appropriate experimental conditions, *in-situ* ATR-FTIR can be used to probe adsorption thermodynamics,[21,22] kinetics,[21-26] and structural changes associated with adsorption processes.[21-24] *In-situ* ATR-FTIR experiments can also be conducted under environmentally relevant conditions, as the technique is compatible with various mineral surfaces and solution variables (e.g. ionic strength, pH, adsorptive concentrations), making it a suitable technique for environmental chemical systems.[21] Due to this flexibility, *in-situ* ATR-FTIR has been applied to many adsorption processes involving soil minerals, including layered clays.[22,23,25,27] In addition to application in environmental systems, ATR-FTIR has received interest for probing protein dynamics by quantifying protein

secondary structure.[28,29] Protein FTIR spectra generally contain three distinct features in the amide I, II and III bands. The amide I (≈1600-1700 cm^{-1}) region is commonly used for protein structural analysis, as these vibrations are sensitive to secondary structure.[29] The amide I region of FTIR spectra can be deconvoluted into components that represent distinct secondary structural features of proteins, including α-helices, β-sheets, turns and random coils.[28,29]

When interpreting FTIR data that represent overlapping peaks, as in the protein amide I band, processing the spectra using two dimensional correlation spectroscopy (2D-COS) can be used to resolve spectral features. 2D-COS is particularly well suited for interpretation of FTIR spectra collected throughout chemical processes that occur across a perturbation gradient.[30] External perturbations include changes in temperature, concentration, pH and time that occur throughout a process, which can be reflected in spectral features.[30] 2D-COS processing of spectra collected across the gradient of interest yields dynamic representations of spectra that can be used to determine sequential appearance of features across the gradient.[30] Due to the flexibility of 2D-COS, it has been applied to a variety of FTIR experiments. Recently, 2D-COS has been used to analyze adsorption and protein denaturation processes, highlighting the potential of 2D-COS application to protein structural analysis during adsorption.[27,31]

This work presents a comprehensive, *in-situ* assessment of the adsorption of a well-studied model protein, bovine serum albumin (BSA), onto a layered aluminosilicate (montmorillonite) mineral surface. *In-situ* ATR-FTIR is used to determine quantitatively and in real time the amount of BSA adsorbed onto

montmorillonite. Furthermore, the secondary structure of adsorbed BSA under a fixed, environmentally relevant set of solution conditions (pH, ionic strength, interlayer and electrolyte cation) is assessed. BSA surface coverage, quantified throughout the adsorption process, is used to clarify adsorption kinetics. The BSA-montmorillonite adsorption equilibrium constant derived from surface coverages are determined, yielding a quantitative measure of the affinity of BSA for montmorillonite. The amide I band of adsorbed BSA is utilized in a complimentary fashion, quantitatively (curve fitting) and qualitatively (2D-COS) interpreting detailed BSA adsorbed structure through the adsorption process. To the best of our knowledge, this work represents the first application of *in-situ* ATR-FTIR to the analysis of kinetic, conformational and equilibrium adsorption parameters of protein adsorption at a mineral/solution interface. This combination of kinetic, equilibrium and conformational approaches, as reported herein, reveals new insights about the process of protein adsorption onto clay minerals. Furthermore, this work establishes a rigorous framework for future analyses of protein behavior at clay surfaces.

Materials and Methods

Materials. Montmorillonite was acquired from the Clay Minerals Repository as Na-rich Wyoming bentonite (SWy-2). Free carbonates[32], organic matter[32] and free iron oxides[33] were all removed from montmorillonite prior to use in experiments. After removal of impurities, montmorillonite was saturated with K^+, [34] freeze-dried and stored under ambient conditions. K^+ was selected to be the interlayer cation on the basis of environmental prevalence and suitability of K^+ as a relatively weak background cation. Purified SWy-2montmorillonite was characterized by FTIR to

verify purity (**Figure A2.1**). Dynamic light scattering measurements of purified SWy-2 from the same sample show a specific surface area of ≈735 m^2/g .[35] BSA used in experiments was used as received (Sigma-Aldrich, ≥98%, M.W.≈66.5 kDa, pI=4.7) and characterized by FTIR to verify purity..

ATR-FTIR measurements. All ATR-FTIR experiments were conducted with a Vertex 70 FTIR spectrometer (Bruker Corp. Billerica, MA) equipped with a deuterated L-alanine doped triglycine sulfate (DLaTGS) detector. A Pike GladiATR accessory with a single bounce diamond internal reflection element (IRE) and flow cell (Pike Technologies Madison, WI) was used for sampling. All spectra were collected from 4500-150 cm^{-1} with 4 cm^{-1} resolution and averaged over 200 scans. For most analyses, spectra were treated post hoc with an atmospheric compensation algorithm, a 9 point Savitsky-Golay smoothing and subsequent background correction to remove water vapor interference and instrumental drift. All spectral manipulations were performed using OPUS 7.2 software (Bruker Corp. Billerica, MA).

***In-situ* adsorption experiments.** BSA solutions used in adsorption experiments ranged in concentration from 1.5 to 15.0 μM. A background electrolyte of 0.005 M KCl was present in all solutions, representing a fairly weak electrolyte and an ionic strength approximating common soil solution values. Solution pH of 5.0 was used for all adsorption experiments and solution spectra. pH was maintained within 0.05 pH units of 5.0 throughout experiments by regulated addition of 0.005 M HCl or KOH with an αlpha pH 200 controller (Eutech Instruments, Singapore). All solutions were made using distilled-deionized water (18.2 MΩ). Montmorillonite films used in experiments were produced by drop casting 50 μL of 0.21 g/L suspension of

montmorillonite over the IRE and drying under N_2 flow. This procedure yields a hydrated thin film with a thickness of around 260 nm as estimated using a previously described calibration approach.[36] Upon deposition, background solution was passed over the montmorillonite film at a rate of 2.0 mL/min for about 2 hours to remove any loosely bound material and allow for re-hydration of the film. Stability of films under flow was considered attained when no changes were observed in FTIR spectra collected during background solution flow. At this point, a background spectrum was collected and adsorption experiments were initiated by switching the background solution with BSA solutions. Spectra were collected every 4 minutes throughout the duration of experiments (about 2 hours) with the exception of the first spectrum, which was collected at around 3 minutes. Data from these experiments represent 2-6 replicates, depending upon the inherent variability of collected data ([BSA] = 1.50, 3.75, 7.50 and 15.0 μM with 2, 2, 6, and 3 replicates, respectively). After adsorption experiments, the IRE, flow cell and tubing were rinsed with distilled-deionized water, then soaked in a 1.5% detergent solution (Citranox, Alcanox, Inc.) for 10 minutes, followed by two rinses with ethanol and then two rinses with distilled-deionized water. Detergent was applied to remove any tightly bound, residual protein from previous experiments.

Adsorption kinetics. Extent of BSA adsorption was monitored using the area of the amide II band with time. The amide II band area, as opposed to amide I or III band area, is often used for monitoring protein adsorption in FTIR experiments, as it is not as sensitive to structural changes or potential aggregation. Data were fitted with commonly used adsorption kinetic models, including Lagergren's pseudo-first order,

pseudo-second order, the Elovich equation and intra-particle diffusion equations.[37,38,39] The pseudo-first order model for adsorption processes can be described by the following equation:[37]

$$\frac{dq_t}{dt} = k_1(q_e - q_t)$$

Where k_1 = the first-order adsorption rate constant, q_e = adsorbed solute quantity at equilibrium, t= adsorption time and q_t = adsorbed solute quantity at time=t. When integrated for the boundary conditions t=0 to t=t and q_t = 0 to q_t = q_t, the equation becomes:

$$\ln(q_e - q_t) = lnq_e - k_1 t$$

This model is commonly used to describe surface controlled adsorption kinetics (i.e. adsorption rates limited by interfacial energetic barriers).[38] If adsorption follows a pseudo-first order model, the rate constant may be derived by plotting $\ln(q_e - q_t)$ versus t, yielding a straight line with a slope = $-k_1$.

Another kinetic model utilized, the pseudo-second order kinetic model, can be described by the following equation:[37]

$$\frac{dq_t}{dt} = k_2(q_e - q_t)^2$$

Where k_2 = the pseudo-second order rate constant, q_e = adsorbed solute quantity at equilibrium and q_t = adsorbed solute quantity at time=t. Upon rearrangement and integration for the boundary conditions t=0 to t=t and q_t=0 and q_t=q_t, the PSO equation can be expressed as:

$$\frac{t}{q_t} = \frac{1}{h} + \frac{1}{q_e}t$$

Where h= the initial adsorption rate and may also be described by $h=k_2 q_e^2$. The pseudo-second order equation, like the pseudo-first order equation, models a surface controlled adsorption rate.[38] A plot of t/q_t versus t yields a straight line with a slope $=1/q_e$ and intercept $= 1/h$ if pseudo-second order adsorption kinetics are followed.

Another adsorption kinetics model, given by the Elovich equation, may be applied to surface controlled adsorption onto energetically heterogeneous surface sites.[37,38] The integrated Elovich equation is written as:

$$\frac{1}{q_t} = \frac{1}{\beta} ln(1 + \alpha\beta t)$$

Where t = time and q_t= adsorbed solute quantity at time=t. α represents initial adsorption rate and β is an empirical constant connected with activation energy distribution.[37,40] When integrated and assuming $\alpha\beta t >> 1$, this equation can be simplified to:

$$q_t = \frac{1}{\beta} ln(\alpha\beta) + \frac{1}{\beta} ln(t)$$

Both representations highlight the logarithmic time dependence of the Elovich model. A plot of q_t versus ln(t) yields a straight line with a slope = $1/\beta$ and intercept = $\ln(\alpha\beta)/\beta$ if an Elovich model describes adsorption kinetics.

Unlike the pseudo-first, pseudo-second order and Elovich kinetic models, the simplified intra-particle diffusion equation describes an adsorption rate that is limited by diffusion within pores, rather than surface related energetic controls. The simplified intra-particle diffusion model is given by:[41]

$$q_t = k_d \sqrt{t}$$

Where k_d= the intraparticle diffusion rate constant. If adsorption kinetics follow this

model, BSA adsorption onto montmorillonite under these conditions is rate limited by diffusion of BSA into pores in the montmorillonite matrix. If adsorption follows the intraparticle diffusion model, a plot of q_t versus $\sqrt{t}$ should produce a straight line with a slope = k_d.

Model parameters were derived from rate plots using linear regression in Microsoft Excel. Models fit with these parameters were compared with experimental data by determining the root-mean-square error (RMSE) of respective models with the following equation:

$$RMSE = \sqrt{\frac{1}{n}\sum_{i=1}^{n}\left(q_{t\ obs.} - q_{t\ pred.}\right)^2}$$

Where n=number of time points (31), $q_{t\ obs.}$= observed amide II area at time = t and $q_{t\ pred.}$= amide II area predicted by the kinetic model at time = t. The most appropriate model for each set of experimental conditions was identified as the most suitable model by having the lowest RMSE value.

Equilibrium isotherms. Amide II areas from the end of adsorption kinetics experiments collected over the range of experimental BSA concentrations (1.50-15.0 µM) were analyzed using the Langmuir isotherm. A fitting of the linearized Langmuir isotherm todata yielded the adsorption parameters of BSA onto montmorillonite under experimental conditions. To apply the Langmuir equation to ATR-FTIR data, fractional surface coverage values must be expressed as a function of absorbance values or peak intensities of a spectral region of interest (i.e. the amide II peak). This relationship has been described previously by the following equation:[42]

$$\frac{c}{A} = \frac{c}{A_\infty} + \frac{1}{KA_\infty}$$

Where c= solute concentration, A= absorbance or area of peak at a given concentration, A_∞= maximum peak absorbance or area of the saturated surface and K= the equilibrium binding constant. This equation represents a linearized form of the Langmuir equation, when graphing c/A verus c, the line yields the parameters A_∞ from the slope and K from the intercept.

Quantitative analysis of adsorbed protein secondary structure. Solution protein spectra and protein spectra from the end of adsorption kinetics experiments (t ≈120 minutes) were used to quantify changes in BSA secondary structure after adsorption. After initial water vapor removal and smoothing, the second derivative spectrum was determined. Using peaks of the second derivative, the position and number of structural component bands can be estimated for subsequent curve fitting. Before fitting curves to designated peak positions, a linear baseline was fitted across the amide I band (1705-1597 cm^{-1}). Once component positions were identified and the baseline established, Gaussian peaks were added to the amide I band according to the second derivative spectrum using the curve fitting function of OPUS 7.2 software. Peak height and width were visually adjusted to best fit the amide I band as an initial estimate and then fitted using the Levenberg-Marquardt algorithm. Resultant peak positions were generally within ≈3 cm^{-1} of the component position predicted by the second derivative. General peak positions and associated tentative secondary structural assignments are as follows: side chain vibrations from 1600-1620 cm^{-1}, aggregated strands from 1620-1630 cm^{-1}, extended chains from 1630-1640 cm^{-1}, random coils

from 1644-1648 cm^{-1}, α-helices from 1650-1660 cm^{-1} and turns from 1660-1690 cm^{-1}.[29,43,44]

2D-COS analysis of adsorbed BSA. 2D correlation analysis of adsorbed protein was performed with 2DShige version 1.3 (Shigeaki Morita, Kwansei-Gaukuin University, 2004-2005). 2D correlation analysis was performed on FTIR spectra from fixed time points in the adsorption process (3, 23, 43, 63, 83, 103 and 123 minutes) to cover the range of experimental time points. These time points were used for all experimental concentrations. Before 2D correlation analysis, spectra were subjected to a defined set of processing steps to minimize interference from artifacts. Spectra for 2D-COS analysis were subjected to initial baseline water and montmorillonite subtraction, water vapor removal and smoothing. Next, the amide I band was cut from the spectrum (1705-1597 cm^{-1}), as this was the region of interest for the 2D correlation analysis. A single, linear baseline was then subtracted across this region. The final step before 2D-COS analysis was the normalization of processed amide I spectra. This step is critical, as it corrects for simultaneous changes in concentration that accompany the external perturbation factor of interest, which aligns with the process of surface adsorption.[43]

Results and Discussion

FTIR spectra. Representative sets of FTIR spectra collected during adsorption experiments can be seen in **Figures 2.1** and **A2.2**. The amide I and II peaks are present at ≈1653 and 1546 cm^{-1}, respectively, in spectra from all experiments. The amide III peaks are located around 1350-1200 cm^{-1} in all spectra as well. Additional peaks at ≈1455 and 1398 cm^{-1} are tentatively assigned to side chain δ CH_2 and ν_s COO^-,

respectively.[29] There is a notable decrease in the region from 3500-3100 cm^{-1} that occurs throughout the BSA adsorption process. These vibrations are likely attributable to montmorillonite interlayer water.[45] The peak present at 3285 cm^{-1}, in the middle of this decreasing region, is tentatively assigned to the ν N-H mode of adsorbed BSA.[29,46]

Spectra highlight the progression of BSA adsorption through the increasing signal of amide I, II and III bands as well as side chain vibrations characteristic of proteins. Furthermore, the adsorption of BSA onto montmorillonite appears to be coupled to water loss at the interface, as suggested by a pronounced decrease of vibrational bands associated with montmorillonite interfacial water. This observed decrease of water vibrations is likely attributable to a higher proportion of BSA being probed, versus water, relative to the background spectrum.

Adsorption kinetics. Of the tested kinetic models, the Elovich model describes the observed adsorption kinetics most suitably, as fits to experimental data yielded lowest RMSE values. A plot of the amide II area versus time for each concentration, and associated Elovich models with parameters, can be found in **Table 2.1** and **Figure 2.2**. The parameters for these other models and linear fits for all kinetic models can be found in **Tables A2.1-3** and **Figures A2.3-5.** Initial adsorption rates increase as BSA concentration increases from 1.50, 3.75, 7.50 and 15.0 μM BSA with α values of 0.0560, 0.0600, 0.106 and 0.160 respectively (**Table 2.1**). When [BSA] = 1.50, 3.75, 7.50 and 15.0 μM, β = 39.8, 21.1, 21.3 and 20.6, respectively. This reflects a pronounced decrease from the lowest experimental concentration to the higher concentrations, which all have similar β values. It has been observed that β is linked to the distribution of activation energies of adsorption, suggesting BSA adsorbed at

higher concentrations may be limited by similar ranges of energetic barriers.[47] This interpretation, however, should be considered tentatively given the empirical nature of the model.

The suitability of the Elovich equation to the adsorption of BSA onto montmorillonite suggests adsorption rates are limited by heterogeneous energetic barriers related to surface adsorption. The inherent logarithmic behavior of this model is often attributed to fixed and induced energetic heterogeneity or surface reconstruction throughout the adsorption process.[48] For the case of protein adsorption onto surfaces, energetic heterogeneity arises from various factors. Lateral interactions between adsorbed proteins, continuous conformational rearrangement of adsorbed proteins and electrostatic forces have all been attributed to energetic heterogeneity and logarithmic adsorption kinetics throughout the adsorption process.[49-51] It is likely one or more of these factors control BSA adsorption rate under experimental conditions. Montmorillonite does have two distinct surfaces in the edge and planar siloxane, which may be responsible for the energetic heterogeneity of BSA adsorption. It should be noted, however, that edge sites represent a minute proportion of montmorillonite surface area and the importance of planar sites on protein adsorption suggest adsorption to edge sites is not playing a large role in the adsorption process.[7,52]

Adsorption isotherm. Figure 2.3 shows the relationship between the amide II peak area at the end of adsorption experiments and BSA solution concentration. BSA concentrations of 1.50, 3.75, 7.50 and 15.0 μM yielded amide II peak areas of 0.139, 0.243, 0.264 and 0.291, respectively. The data fit well to the Langmuir isotherm producing a straight line (R^2=0.9973) when plotting c/A_e versus c, yielding a K value

of 5.97×10^5 M^{-1} and an A_∞ of 0.324.

Both parameters from the Langmuir equation, the relatively large binding constant and approach to surface saturation at low BSA concentrations (1.50-15.0 μM (0.10-1.0 mg/mL)), indicate that BSA has a strong affinity for K^+-montmorillonite surfaces. These results are in general agreement with previous experiments of proteins (e.g. BSA, lysozyme, betalactoglobulin) on aluminosilicate clay surfaces.[17, 52] Experiments probing betalactoglobulin adsorption onto montmorillonite, produced a *K* value of 8.7×10^5 M^{-1} and a surface saturation at ≈0.2 mg/mL protein concentration.[17] A previous experiment investigating BSA adsorption onto K^+-saturated montmorillonite revealed a lower *K* value than this study, with $K = 1.80 \times 10^5$ M^{-1}.[44] It should be noted, however, that this value was acquired with a higher background electrolyte concentration.[14] A higher ionic strength could potentially reduce the affinity of BSA for montmorillonite, as the adsorption affinity of proteins generally decreases with increasing solution ionic strength due to competitive ion exchange between the background cation and protein.[7,53]

Adsorbed BSA secondary structure. Representative curve fitting of the solution and adsorbed BSA amide I region along with 2nd derivative spectra can be seen in **Figure 2.4**. Results of amide I curve fitting for BSA in solution and adsorbed BSA at each concentration are shown in **Figure 2.5** and summarized in **Table 2.2**. The secondary structure of BSA in a 150 μM solution was determined to consist of α-helices (≈68%), extended chains (≈25%), turns (≈6%) and side chain vibrations (≈1%) (**Figure 2.5**). These values agree closely with previous structural estimates, which also suggest BSA possesses a primarily helical structure with additional contributions from extended

chains connecting helical sections and turns.[54] In adsorption experiments with [BSA] = 1.50 μM and θ=0.43 (based on Langmuir parameters), BSA assumes a distorted secondary structure relative to BSA in solution. Adsorbed BSA at this surface coverage is lower in α-helix content (≈47%) and higher in both extended chain (≈31%) and turn (≈16%) structures compared to native BSA. It should be noted that the observed increase in extended chain content is within one standard deviation of the native BSA content (**Figure 2.5**). While aggregated strands (≈4%) and side chain vibrations (≈1%) are observed at this surface coverage, neither contributes substantially to secondary structure when experimental variability is put into account. When [BSA] = 3.75 μM and θ=0.75, adsorbed BSA conformation is also distorted. Unlike BSA adsorbed at θ=0.43, α-helical structures are slightly higher (≈76%) than native BSA. Accompanying an increase in α-helices relative to BSA in solution is a slight increase in turn content to ≈8%. This represents a decrease in turn structures from adsorbed BSA at lower surface coverage and an increase relative to BSA in solution. A decrease in extended chain structure (≈12%) from both solution BSA and adsorbed BSA at lower surface coverage is observed. As with adsorbed BSA at lower surface coverage values, aggregated strands (≈5%) and side chain vibrations (≈3%) were observed, but to a marginal extent. At equilibrium [BSA] = 7.50 μM and θ=0.81, BSA structure possesses extended chain (≈18%) and α-helix (≈67%) structures that are lower than solution BSA, but are not appreciably different based on standard deviation values (**Figure 2.5**). Turns (≈8%) also represent a similar contribution to BSA structure in solution under these conditions. Aggregated strands (≈5%) and side chain vibrations (≈1) contribute to the rest of adsorbed BSA structure, although not

appreciably when considering standard deviation of results. The highest experimental concentration and surface coverage, [BSA]=15.00 μM and θ=0.90, yielded adsorbed BSA structure of ≈63% α-helices, ≈26% extended chains, ≈9% turns and ≈2% side chain vibrations. All of these structural contents, with the exception of an increase in the proportion of structural turns, are not substantially different from BSA in solution (**Figure 2.5**).

These results suggest conformational deformation influences on BSA adsorption onto montmorillonite. Previous FTIR experiments probing protein adsorption onto clay surfaces also highlight these points.[14,16] Conformational changes to BSA upon adsorption onto montmorillonite at pD values between 2.9 and 6.7 were attributed to losses in helical structures and increases in bent/extended chains.[14] The present *in-situ* ATR-FTIR experiments show a similar dynamic at the lowest observed surface coverage and BSA solution concentration (θ=0.43 and [BSA]=1.50 μM) at equilibrium, where α-helices are reduced and extended chain structures and turns increase upon adsorption. This is indicative of a more expanded protein structure, suggestive of a conversion of more rigid helical structures to less rigid extended chains.[55] At higher concentrations, however, this relationship does not seem to hold. BSA structure at the second lowest surface coverage (θ=0.75) exhibits a slight increase in α-helix structures and a decrease in extended chains relative to solution BSA. The two highest fractional surface coverage values, θ=0.81 and 0.90, show little difference between adsorbed BSA conformation and that of BSA in solution. When θ=0.81, α-helix, extended chain, turn and side chain content are within one standard deviation of solution BSA secondary structure, with small and potentially insignificant

contributions from aggregated strands. Similarly, at θ=0.81 α-helix and extended chain structural content is representative of solution BSA. Modest increases in side chain and turn vibrations were also observed at the highest experimental surface coverage, suggesting only minor structural alteration to BSA at higher surface coverages. Retention of most intrinsic secondary structure at higher surface coverage is interpreted as the adoption of a more compact, native-like, structure when compared with adsorbed BSA at lower surface coverage, which takes on a more open and altered form to maximize contact with the montmorillonite substrate.

Sequence of BSA conformational changes. 2D-COS results of the process of BSA adsorption onto montmorillonite are shown in **Table 2.3**. Representative synchronous and asynchronous plots depicting the sequence of structural changes contributing to BSA conformational alteration at the montmorillonite surface are shown in **Figure 2.6.** Furthermore, a representative autocorrelation spectrum is shown above the synchronous plot, depicting peaks corresponding with secondary structural components that change in intensity (positively or negatively) in response to the adsorption.[30] Sequence of changes to component peaks relative to each other can be determined by the position of cross peaks, given as (ν_1, ν_2), and the associated sign, shown as red (+) and blue (-) regions in synchronous and asynchronous plots. Frequency coordinates of the cross peaks correspond with a unique secondary structural component of BSA. The sign of the cross peak on the synchronous plot is used to determine whether cross peak associated frequencies respond in-phase or out-of-phase to the external perturbation of interest (i.e. adsorption).[30] A "+" synchronous cross peak denotes that changes to secondary structural components associated with ν_1

and ν_2 occur in-phase (i.e. both ν_1 and ν_2 increase or decrease as adsorption progresses), whereas a "—" synchronous cross peak suggests changes to components assigned to ν_1 and ν_2 occur out-of-phase (i.e. ν_1 increases and ν_2 decreases during adsorption, or vice versa).[30] Cross peak sign on the asynchronous plot can be used along with synchronous cross peak sign to determine the sequence of changes to ν_1 and ν_2 in response to adsorption. If the cross peak has the same sign on both the synchronous and asynchronous plots, changes to ν_1 occur in the adsorption process before changes to ν_2.[30] If the cross peak signs on synchronous and asynchronous plots are opposite, changes to ν_2 occur in the adsorption process before changes to ν_1. Interpretation of this analysis highlights the link between individual secondary structural components, revealing not only the dynamic association of distinct secondary structures, but also the order in which they respond to the adsorption process.[30]

The autocorrelation spectrum for [BSA]=1.50 μM (**Figure A2.6**) shows five primary peaks at 1631, 1639, 1649, 1662 and 1689 cm^{-1}. These frequencies correspond with extended chains (1631 and 1639 cm^{-1}), α-helices or random coils (1649 cm^{-1}) and turns (1662 and 1689 cm^{-1}). Prominent cross-peaks, synchronous and asynchronous signs and resultant sequences are listed in **Table 2.3**. Although yielding a peak in the autocorrelation spectrum, the feature at 1639 cm^{-1} does not result in features on both synchronous and asynchronous plots. The only visible cross peaks for this feature on the synchronous plot, at (1639, 1662) and the complimentary peak at (1662, 1639), are not resolved in the asynchronous plot. This has been discussed previously in the literature and is potentially the result of frequency or bandwidth

changes that occur during adsorption, as these factors are recognized as possibly skewing peak positions and intensities in 2D-COS plots. [56]As such, peaks without both synchronous and asynchronous peaks will be neglected for interpretation of the adsorption process. Negative synchronous cross peaks at (1649, 1662) and (1631, 1649) suggest changes to α-helical/random structures occur out-of-phase with changes to turns and extended chains. Amide I curve fitting results suggest the peak at 1649 cm^{-1} is attributable to α-helices, rather than random coils, as no random coil structures were evident in second derivative spectra of any BSA sample analyzed, either in solution or adsorbed. Coupled with the amide I curve fitting results, turns and extended chains form during adsorption at the expense of α-helices. Other major cross peaks at (1631, 1662), (1662, 1689) and (1631, 1689) are positive, meaning changes to turns and extended chains occur in-phase, probably in the form of an increase in these structures. From the asynchronous plots, the sequence of these secondary structural alterations can be interpreted as:[30]

$$1631\ cm^{-1}\ (\text{extended chains}) \rightarrow 1649\ cm^{-1}\ (\alpha\text{-helices/random coils})$$

$$\rightarrow 1689\ cm^{-1}\ (\text{turns}) \rightarrow 1662\ cm^{-1}\ (\text{turns})$$

Based on this sequence and the phase of observed structural transitions, adsorbed BSA unfolds first into extended chains, followed by a loss of α-helices and a subsequent conversion to turns. Overall, this corresponds with a transformation of relatively compact α-helices into less ordered turns and extended chains. Conversion of α-helices into less compact is consistent with BSA assuming an expanded, unfolded structure upon adsorption.[30, 57]

When BSA adsorbs onto montmorillonite at [BSA]=3.75 μM and θ=0.75, the

autocorrelation spectrum reveals six primary peaks (**Figure 2.6):**1610, 1622, 1641, 1664, 1678 and 1689 cm^{-1}. These vibrations tentatively correspond with side chain vibrations (1610 cm^{-1}), aggregated strands (1622 cm^{-1}), extended chains (1641 cm^{-1}) and turns (1664, 1678 and 1689 cm^{-1}). According to the synchronous plot, changes to extended chains, turns and side chain vibrations occur in-phase with each other, indicating an increase or decrease of these components together during the adsorption process (**Table 2.3**). The response of aggregated strands to adsorption is out-of-phase with turns and extended chains and not correlated with side chain vibrations. Considering these two situations, it is possible that loss of aggregated strands is coupled with an increase in extended chains and turns and an increase in side chain vibrations. It is also plausible that aggregated structures arise from converted extended chains and turns. Given the relatively high surface coverage and the quantitative analysis of adsorbed BSA structure at this surface coverage which depicts a loss of extended chain structures (**Table 2.2**), the latter scenario seems more likely. The contribution of aggregated strands to bound BSA conformation, however, is also low, indicating that changes to these structures are minimal. From synchronous and asynchronous plots, the sequence of structural changes in adsorbed BSA is interpreted as follows:

1641 cm^{-1} (extended chains) → 1610 cm^{-1} (side chains), 1622 cm^{-1} (aggregated strands) → 1662 cm^{-1} (turns), 1678 cm^{-1} (turns) → 1689 cm^{-1} (turns)

This sequence possibly suggests an initial conversion of extended chains to aggregated strands with a loss of side chain structure concurrent with, or after, aggregated strand formation. These transitions are then followed by a loss of turn structures, which

represent externalized and hydrated structures.[42] At this surface coverage and BSA concentration, BSA assumes a more compact form than is evident from the lower surface coverage studied. It is notable that aggregated structures begin to play a role in BSA adsorption at θ=0.75, the result of increasing interaction between adsorbed BSA molecules, despite the more compact form. In contrast to the adsorption process through lower surface coverage values, α-helices do not seem to be altered throughout adsorption at this set of conditions. The more compact form of adsorbed BSA likely favored retention of these structures, as opposed to unfolding into extended chains and turns. Curve fitting results of adsorbed BSA reinforce this interpretation, with secondary structural analysis yielding an α-helix composition similar to solution BSA (**Table 2.2** and **Figure 2.4**).

2D-COS plots for the adsorption process when [BSA] =7.50 μM and θ=0.81 can be found in **Figure A2.7**. The autocorrelation spectrum for adsorption under these conditions has five primary peaks: 1606, 1620, 1633, 1665 and 1688 cm^{-1}. Synchronous plot signs for (1606, 1665), (1633, 1665) and (1665, 1689) are all positive, meaning changes to side chains, extended chains and turns are all in-phase and, thus, all respond to adsorption in the same direction (i.e. increase or decrease). Changes to aggregated strands occur out-of-phase with extended chains and turns and are not strongly correlated with side chain vibrations. Response of these structures to adsorption resembles that of adsorption when [BSA] = 3.75 μM and θ=0.75. As such, the interpretation of an increase in aggregated strands and a decrease of more expanded structures, like turns and extended chains, is applied to adsorption at [BSA] = 7.50 μM and θ=0.81 as well. The inferred sequence of changes is:

1606 cm^{-1} (side chains), 1622 cm^{-1} (aggregated strands) → 1662 cm^{-1} (turns) → 1633 cm^{-1} (extended chains), 1689 cm^{-1} (turns)

While the same type of structural changes is interpreted for adsorption at [BSA] = 3.75 and 7.50 μM, the sequence of changes appears to be slightly different. Alterations to extended chain structures occur early in the adsorption process when [BSA] = 3.75 μM and precede formation of aggregated strands. This is different when contrasted with the [BSA] = 3.75 μM system, where extended chains appear to decrease last in the adsorption process, after changes to aggregated strands. As with [BSA] = 3.75 μM, BSA structure upon adsorption likely represents a more compact figure relative to [BSA] = 1.50 μM. This point is further highlighted by curve fitting results, which have α-helix, extended chain and turn structures similar to solution BSA. The primary difference is the small presence of aggregated strands in adsorbed BSA.

At the highest BSA concentration and surface coverage ([BSA] = 15.0 μM and θ=0.90) the autocorrelation plot of the adsorption process has five primary features at 1604, 1621, 1638, 1672 and 1689 cm^{-1} (**Figure A2.8** and **Table 2.3**). Side chain, extended chain and turn secondary structures are modified by adsorption in-phase. Aggregated structures change out-of-phase with extended chains and turns and are not correlated with side chain vibrations. Interpretation follows that of adsorption when [BSA] = 7.50 μM and θ=0.81, with a decrease of turns, extended chain and side chain structures through the adsorption process with an increase of aggregated strands. The sequence of structural changes under these conditions is:

1604 cm^{-1} (side chain), 1622 cm^{-1} (aggregated strands) →1672 cm^{-1} (turns) → 1638 cm^{-1} (extended chains), 1688 cm^{-1} (turns)

The sequence and phase of structural changes upon BSA adsorption at [BSA] = 15.0 μM correspond with those when [BSA] = 7.50 μM, indicating the transformation pathway adsorbed BSA undergoes is the same in both systems, with extended chains, turns, side chains and aggregated strands being affected.

2D-COS analyses yield a wealth of information regarding the dynamic adsorption of BSA onto montmorillonite. This analysis shows at least 2 distinct concentration and surface coverage dependent adsorption pathways for BSA on montmorillonite. At the lowest θ and [BSA] studied, α-helix structures appear to unfold into extended chains and turns during adsorption. Through this pathway, BSA assumes a more open and unfolded conformation than at higher θ values, transferring more ordered, rigid structures (i.e. α-helices) into extended chains and turns in order to increase surface contact with montmorillonite. At higher θ and [BSA] values, a decrease in extended chain/turn structures and side chain rearrangement seems to occur in order to develop a greater extent of aggregated structures through protein-protein interaction. These results are in contrast to previous 2D-COS analysis of cytochrome c_{552} adsorption onto montmorillonite, which highlight the role of β structures and turns in the adsorption process, rather than extended chains.[58] Comparing results between these two studies, however, is challenging provided the intrinsic differences between BSA and cytochrome c_{552}, which have different properties. Cytochrome c_{552} possesses a different secondary structure from BSA (cytochrome c_{552} has more native β-sheets and fewer α-helices than BSA), likely resulting in different structural implications of adsorption.[58] For the higher concentrations studied here, the proposed pathways from 2D-COS analyses also

contrast with existing concepts of BSA unfolding on montmorillonite, which suggests a degradation of helical structures and subsequent conversion into bent structures.[15] At higher concentrations, no apparent changes to helices were resolved with 2D-COS, suggesting these structures are not playing a dynamic role in the BSA adsorption process. Apparent discrepancies between these studies may be the result of experimental concentrations and resultant surface coverage values, as the previous work was based on one BSA concentration (30 g/L or ≈ 450 μM) and more available montmorillonite surface area with pH as the variable.[15] 2D-COS results correspond with observed logarithmic adsorption kinetics, which indicate potential conformational rearrangement of BSA throughout the adsorption process. This is observed for all BSA concentrations used. Furthermore, 2D-COS results show the influence of aggregated strands at higher experimental BSA concentrations, highlighting the possibility that lateral adsorbate interactions contribute to the energetic heterogeneity of BSA adsorption kinetics under these conditions.

Conclusions

The adsorption of BSA onto montmorillonite was studied under a set of environmentally relevant solution conditions (pH=5.0 and [KCl]=0.005 M) and varying concentrations (1.50-15.0 μM), revealing the importance of solution BSA concentration on adsorption dynamics. Our results suggest BSA readily adsorbs onto montmorillonite, with reaction kinetics following an Elovich model, suggesting a reaction rate governed by heterogeneous energetic barriers. BSA conformational rearrangement and lateral protein-protein interactions likely represent associated energetic barriers at all studied concentrations. The BSA/montmorillonite binding

constant (K= 5.97x 10^5 M^{-1}) represents a strong association between BSA and montmorillonite. Amide I curve fitting identifies that the extent of BSA unfolding on montmorillonite decreases with increasing BSA concentration and θ, underlining the link between adsorbed BSA conformation and BSA concentration/θ. At the lowest BSA concentration studied, adsorbed BSA loses α-helices into extended chains and turns, representing a decrease in rigid structures into more expanded structures. At higher BSA concentrations, adsorbed BSA assumes a more compact secondary structure that is more representative of native BSA. Along with different conformations of adsorbed BSA, 2D-COS analyses show distinct pathways of structural modification throughout the adsorption process. Like the resultant conformation changes, these pathways are dependent upon BSA concentration and θ. At the lowest BSA concentration studied (1.50 μM), changes to adsorbed BSA started with a gain of extended chains, then a loss of α-helices and a gain of turn structures. When [BSA] = 3.75 μM, loss of extended chains was followed by side chain rearrangement, increase in aggregated strands and loss of turns. For [BSA] = 7.50 and 15.0 μM, side chain rearrangements and increase of aggregated structures preceded a decrease in turns and extended chains. This suggests that when solution concentrations differ ([BSA] = 7.50 and 15.0 μM), similar surface coverage values (θ=0.81and 0.90) may exhibit similar structural transformation pathways.

This study sheds light on the mechanism behind a process of environmental significance, the sorption of biomolecules and biomolecular fragments onto soil mineral surfaces. Current prevailing concepts of soil organic matter (SOM) stabilization on mineral surfaces are built on the assertion that amphiphilic, protein-

like molecules undergo conformational reorganization upon adsorption at mineral surfaces.[2] Results presented in this work suggest unfolding of globular proteins, such as BSA, could likely occur when solution protein concentrations and surface coverage are low. This seems like a plausible scenario considering reported protein concentrations in soil solution (reported as a few to a few tens of mg L^{-1}, depending upon methodology) and known adsorption isotherms of proteins on common soil minerals, which often show surface saturation when protein solution concentration is a few tenths of a gram per liter.[18,52,59] This study also help clarify how carbon retention mechanisms on mineral surfaces can be linked to carbon and nitrogen turnover through enzymatic degradation. While enzymes bound to mineral colloids may be inactivated, depending upon adsorbed conformation, it is possible that retained enzymes maintain activity, which could result in clay-mineral complexes being a reserve of concentrated catalytic activity.[60] The presented work begins to highlight concentration and surface coverage dependent conditions under which extensive conformational rearrangement is likely to occur, potentially having an impact on carbon turnover rates in soils.[60]

Acknowledgements

This research was supported by the Section of Soil and Crop Sciences of the School of Integrative Plant Sciences with the College of Agriculture and Life Sciences at Cornell University. M.P.S. also acknowledges the Cross-Scale Biogeochemistry and Climate (CSBC) IGERT program at Cornell University (NSF award number: 1069193) for financial support.

Table 2.1 Elovich model parameters for each experimental concentration

concentration (μM)	α	β	RMSE
1.50	0.056	39.8	4.28×10^{-3}
3.75	0.060	21.1	3.80×10^{-3}
7.50	0.106	21.3	3.34×10^{-3}
15.0	0.160	20.6	3.10×10^{-3}

Table 2.2 Results of amide I band curve fitting for BSA in solution (150 μM) and BSA adsorbed onto montmorillonite at t=120 minutes. Numbers in parentheses represent standard deviations from an average of replicates.

concentration (μM)	predicted θ	% side chain	% aggregated strands	% extended chain	% α-helix	% turns
150 (BSA solution)	----------	0.95	0.00	24.8	68.2	6.09
1.50	0.43	1.06 ± (1.50)	3.93 ± (5.56)	31.4 ± (17.0)	47.2 ± (17.5)	16.4 ± (4.56)
3.75	0.75	2.63 ± (3.71)	5.14 ± (7.27)	11.8 ± (2.99)	76.8 ± (4.66)	7.78 ± (0.55)
7.50	0.81	1.19 ± (1.13)	5.18 ± (7.08)	18.2 ± (8.38)	67.2 ± (10.3)	7.89 ± (5.05)
15.0	0.90	1.85 ± (0.69)	0.00	26.0 ± (6.04)	63.0 ± (6.10)	9.13 ± (0.54)

Table 2.3 Results of 2D-COS analysis for each experimental concentration, showing prominent cross peaks, synchronous and asynchronous cross peak signs and resultant sequences.

Concentration (μM)	Cross Peak (ν_1, ν_2)	Synchronous	Asynchronous	Sequence
1.50	(1631, 1662)	+	+	1631>1661
	(1631, 1689)	+	+	1631>1689
	(1631, 1649)	-	-	1631>1649
	(1639, 1662)	+		
	(1649, 1662)	-	-	1649>1662
	(1662, 1689)	+	-	1662<1689
3.75	(1610, 1641)	+	-	1610<1641
	(1610, 1662)	+	+	1610>1662
	(1622, 1689)	-	-	1622>1689
	(1622, 1678)	-		
	(1622, 1662)	-	-	1622>1662
	(1622, 1641)	-	+	1622<1641
	(1641, 1678)	+	+	1641>1678
	(1641, 1662)	+	+	1641>1662
	(1662, 1689)	+	+	1662>1689
	(1664, 1678)	+		
	(1678, 1689)	+	+	1678>1689
7.50	(1606, 1665)	+	+	1606>1665
	(1620, 1665)	-	-	1620>1662
	(1633, 1689)	+		
	(1633, 1665)	+	-	1633<1665
	(1665, 1689)	+	+	1665>1689
15.0	(1604, 1688)	+	+	1604>1688
	(1604, 1672)	+		
	(1622, 1688)	-	-	1622>1688
	(1622, 1672)	-	-	1622>1672
	(1635, 1672)	+	-	1638<1672
	(1672, 1688)	+	+	1672>1688

Secondary structural components and assignments: Side chains (1600-1620 cm^{-1}), aggregated strands (1620-1630 cm^{-1}), extended chains (1630-1640 cm^{-1}), random coils (1644-1648 cm^{-1}), α-helices (1650-1660 cm^{-1}) and turns (1660-1690 cm^{-1}).

Figure 2.1 FTIR spectra from a representative adsorption experiment ([BSA] = 3.75 µM). Spectra shown were collected at ≈20 minute intervals from t = 3 minutes until t =120 minutes.

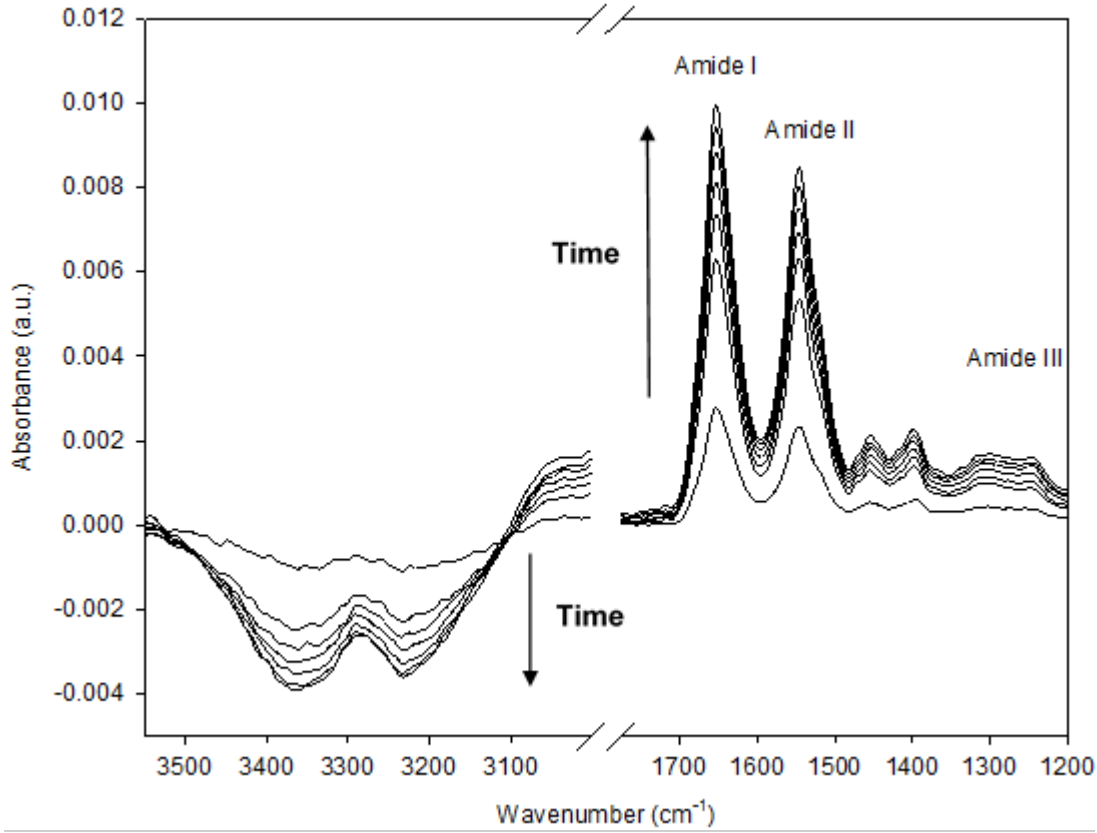

Figure 2.2 BSA adsorption kinetic plots for [BSA] = 1.50 (yellow squares), 3.75 (red x), 7.50 (green circles) and 15.0 µM (orange triangles). Elovich kinetic models for each series are depicted by lines of corresponding color.

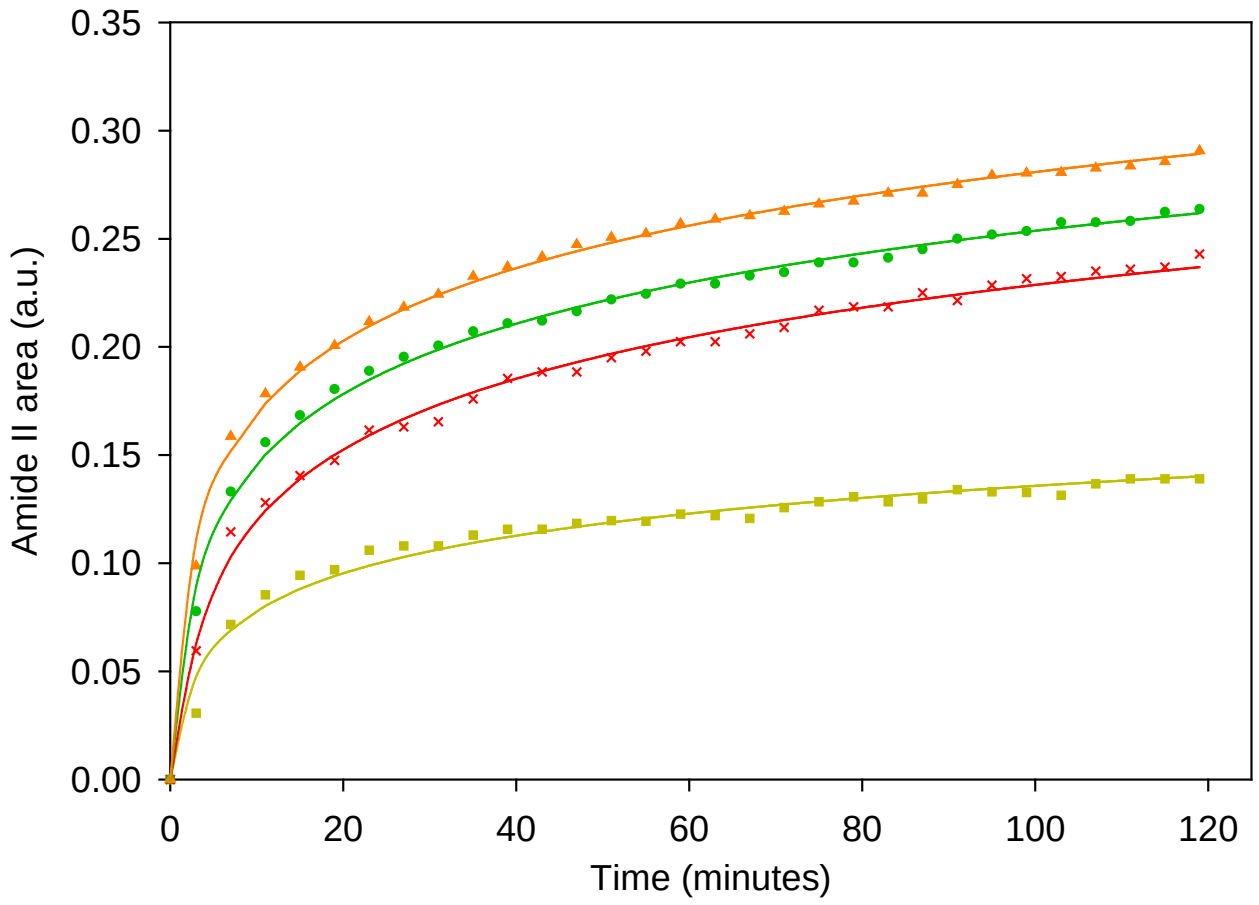

Figure 2.3 Adsorption isotherm for BSA adsorption onto montmorillonite (dots) with the experimental Langmuir model (line). Error bars represent standard deviation values from replicates.

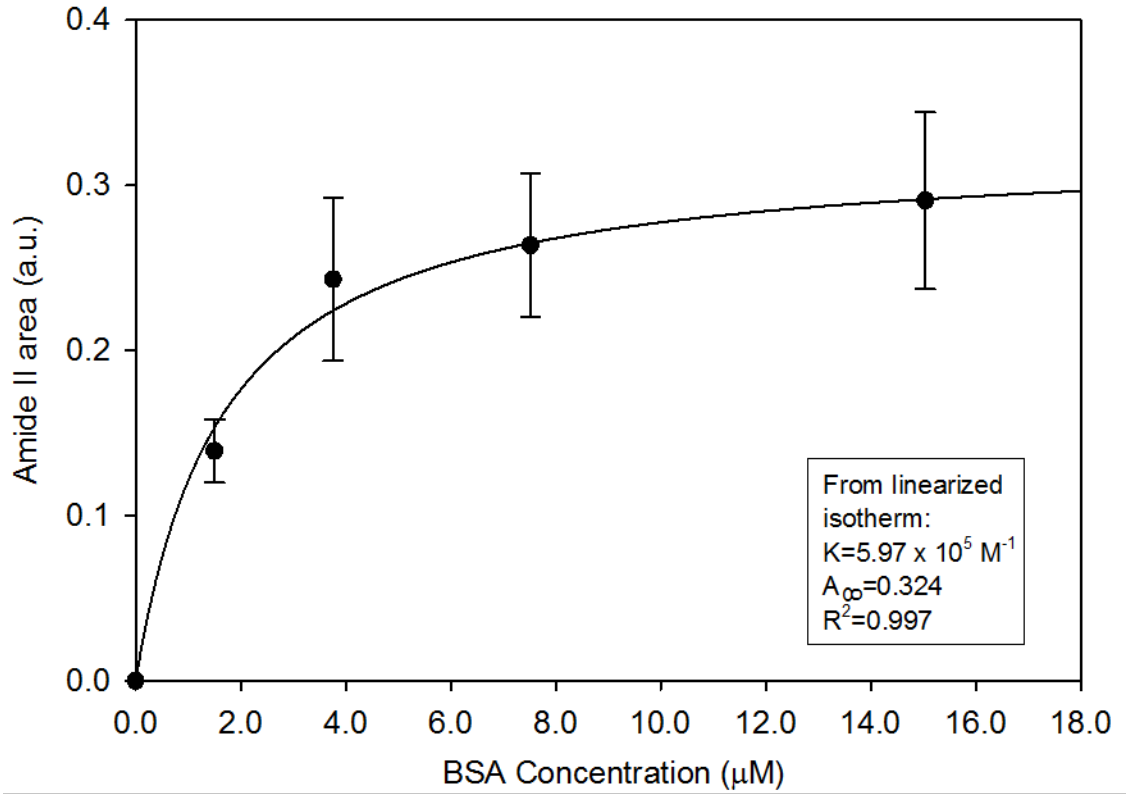

Figure 2.4 Example 2nd derivative amide I deconvolution of 150 µM BSA solution (a) and adsorbed BSA at 15.0 µM and θ=0.90 (b). Amide I band and components are represented by solid black line, the second derivative spectrum is represented by black dashed line and sum of curve fitting is represented by red circles.

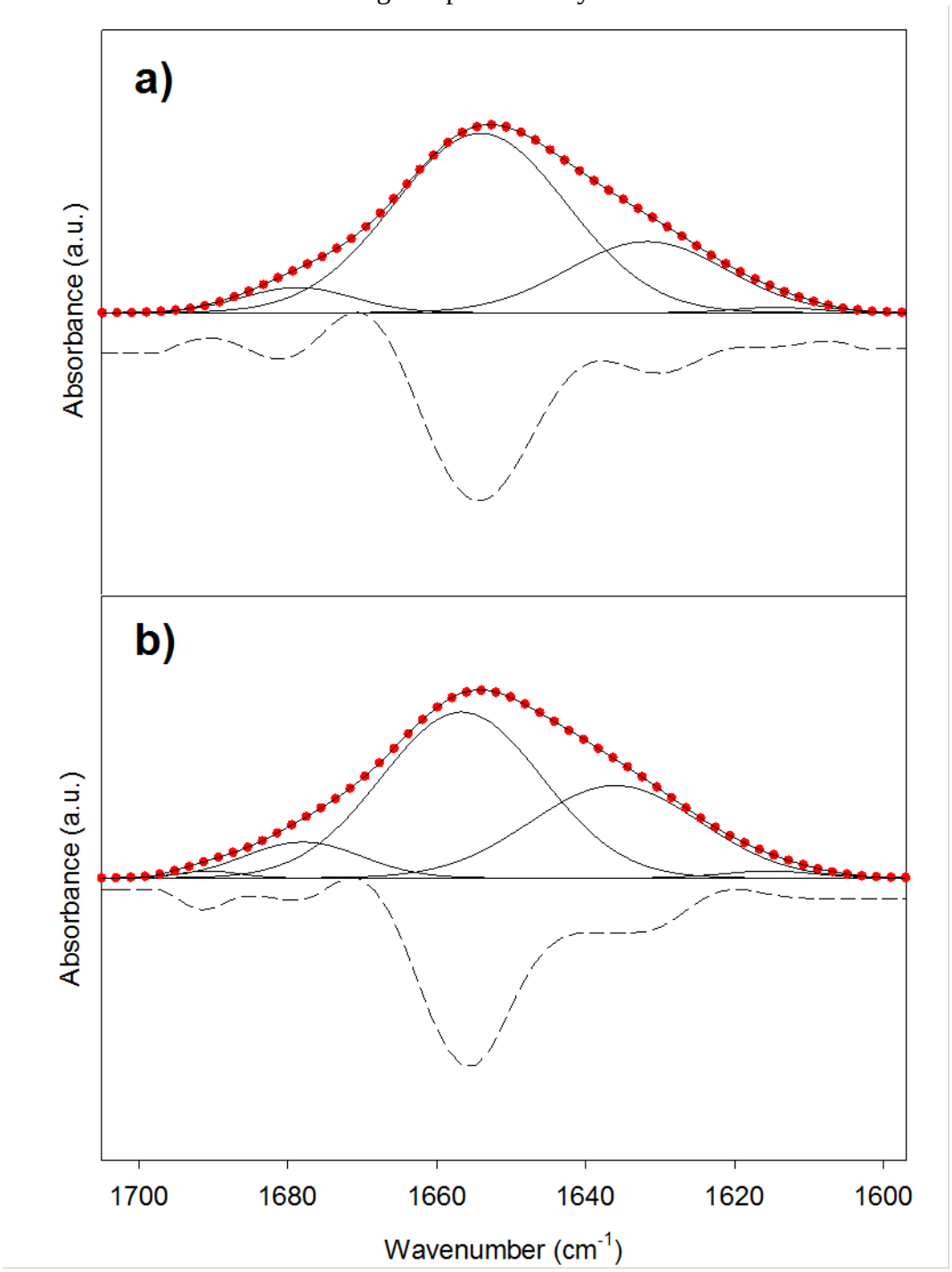

Figure 2.5 Results of amide I curve fitting after 120 minutes of adsorption at each concentration. Dots represent proportion of α-helices (orange circles), extended chains (green triangles), turns (black inverted triangles), aggregated strands (red x) and side chains (blue squares) in secondary structure for adsorbed BSA at each concentration. Dotted lines of corresponding color represent solution BSA secondary structural composition.

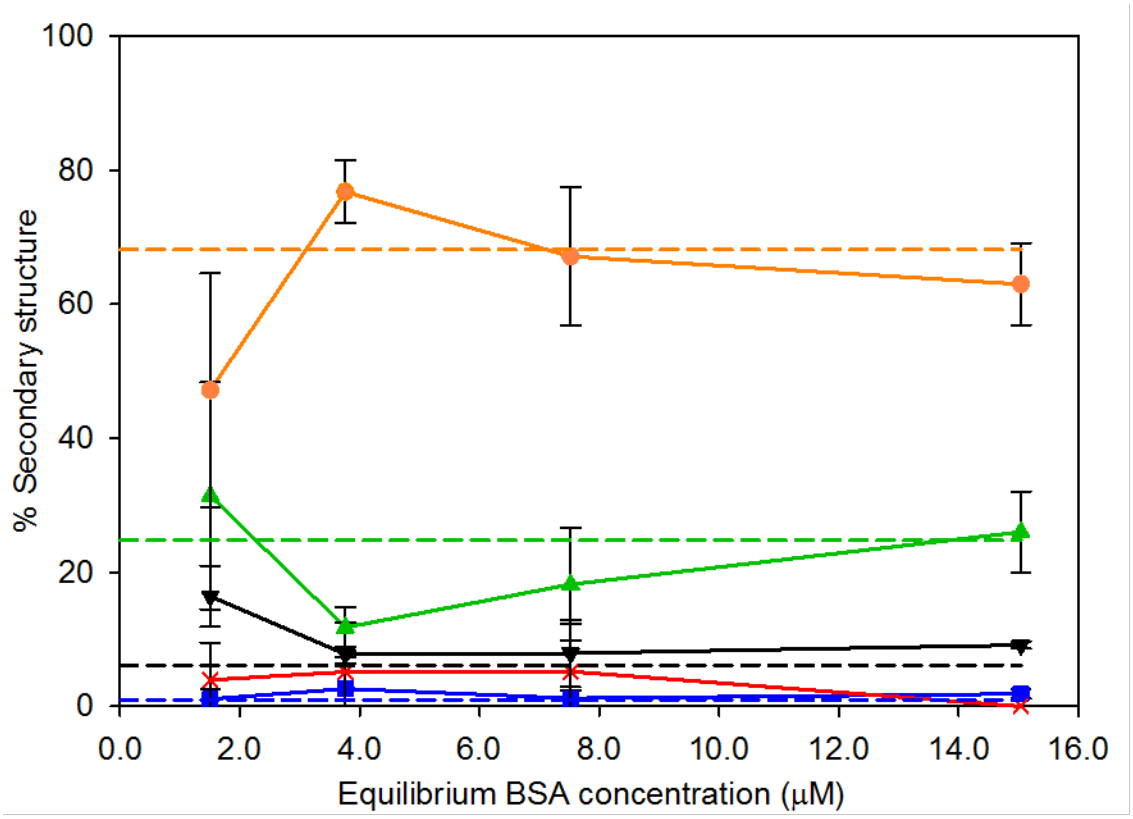

Figure 2.6 Synchronous (top) and asynchronous (bottom) 2D-COS plots for [BSA] = 3.75 µM with corresponding autocorrelation spectrum and labelled peaks in the amide I band. Correlation values are shown in the legend.

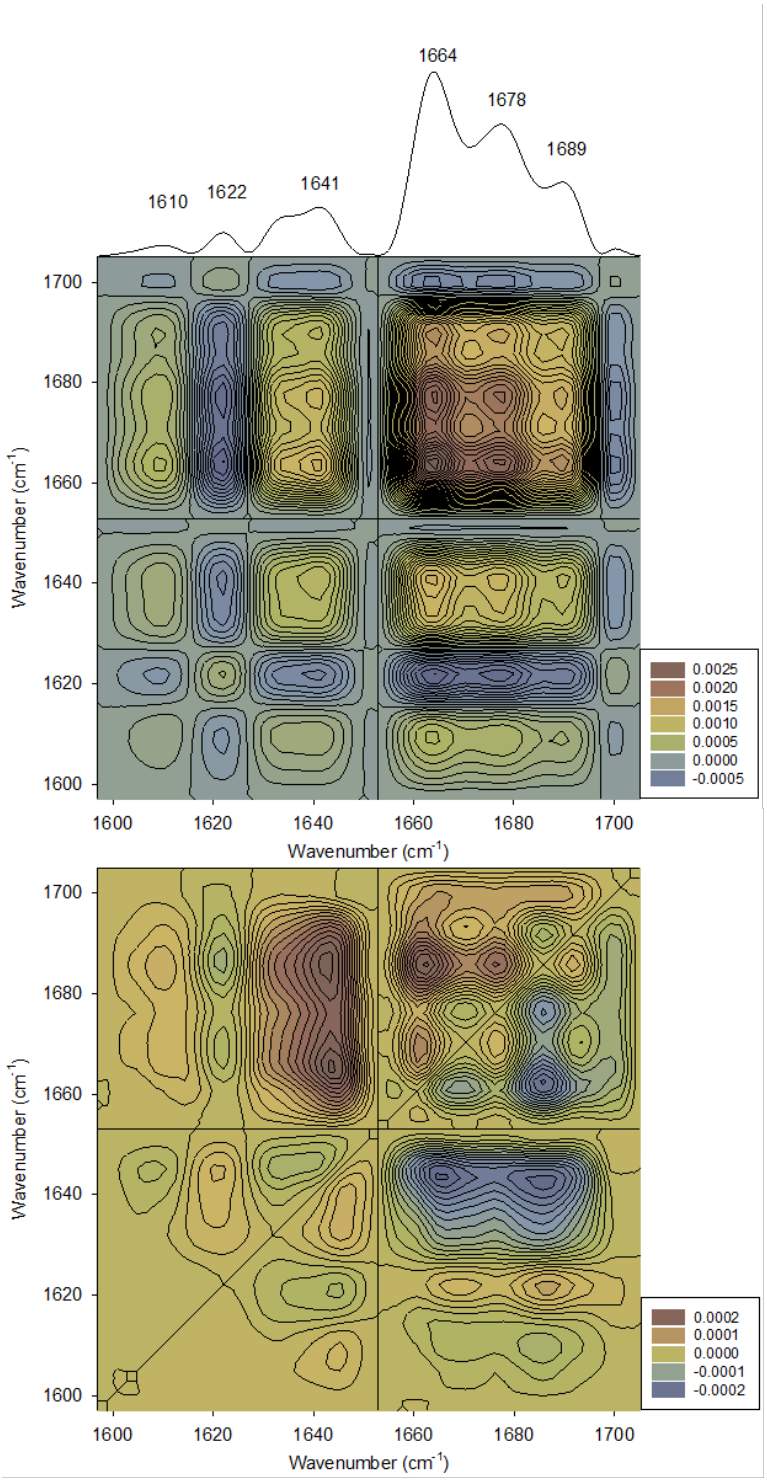

REFERENCES

(1) Quiquampoix, H.; Servagent-Noinville, S.; Baron, M.H. Enzyme Adsorption on Soil Mineral Surfaces and Consequences for the Catalytic Activity. In *Enzymes in the Environment: Activity, Ecology, and Applications*; Burns, R.G.; Dick, R.P., Eds.; CRC Press: Boca Raton, 2002; pp 285-306.

(2) Kleber, M.; Sollins, P.; Sutton, R. A conceptual model of organo-mineral interactions in soils: self-assembly of organic molecular fragments into zonal structures on mineral surfaces. *Biogeochemistry* **2007,** *85,* 9-24.

(3) Houghton, R.A. The Contemporary Carbon Cycle. In *Biogeochemistry* Vol. 8 *Treatise on Geochemistry*; Schlesinger, W.H., Ed.; Elsevier-Pergamon: Oxford, 2003; pp 425-472.

(4) Saxena, D.; Flores, S.; Stotzky, G. Vertical movement in soil of insecticidal Cry1Ab protein from *Bacillus thuringiensis*. *Soil Biol. Biochem.* **2002,** *34,* 111-120.

(5) Nielsen, K.M.; Calamai, L.; Pietramellara, G. Stabilization of Extracellular DNA and Proteins by Transient Binding to Various Soil Components. In *Nucleic Acids and Proteins in Soil*; Nannipieri, P.; Smalla, K., Eds.; Springer-Verlag: Heidelberg, 2006; pp 141-153.

(6) Stotzky, G. Persistence and Biological Activity in Soil of Insecticidal Proteins from *Bacillus thuringiensis* and of Bacterial DNA Bound on Clays and Humic Acids. *J. Environ. Qual.* **2000,** *29,* 691-705.

(7) Yu, W.H.; Li, N.; Tong, D.S.; Zhou, C.H.; Lin, C.X.; Xu, C.Y. Adsorption of proteins and nucleic acids on clay minerals and their interactions: A review. *Appl. Clay Sci.* **2013,** *80-81,* 443-452.

(8) Bleam, W.F. *Soil and Environmental Chemistry,* 1st Ed.; Academic Press: Waltham, MA, 2011.

(9) Johnston, C.T.; Premachandra, G.S.; Szabo, T.; Lok, J.; Schoonheydt, R.A. Interaction of biological molecules with clay minerals: a combined spectroscopic and sorption study of lysozyme on saponite. *Langmuir* **2012,** *28,* 611-619.

(10) Zhou, X.Y.; Huang, Q.Y.; Chen, S.W.; Yu, Z.N. Adsorption of the insecticidal protein of *Bacillus thuringiensis* on montmorillonite, kaolinite, silica, goethite and red soil. *Appl. Clay Sci.* **2005,** *30,* 87-93.

(11) Fiorito, T.M.; Ferris, J.P.; Stotzky, G. Adsorption and binding of the transgenic plant proteins, human serum albumin, β-glucuronidase, and Cry3Bb1 on montmorillonite and kaolinite: microbial utilization and enzymatic activity of free and clay-bound proteins. *Appl. Clay Sci.* **2008,** *39,* 142-150.

(12) Norde, W. Driving forces for protein adsorption at solid surfaces. *Macromolecular Symposia* **1996,** *103,* 5-18.

(13) Mori, O.; Imae, T. AFM investigation of the adsorption process of bovine serum albumin on mica. *Colloids and Surfaces B* **1997,** *9,* 31-36.

(14) Kolman, K.; Makowski, M.M.; Golriz, A.A.; Kappl, M.; Piglowski, J.; Butt, H.J.; Kiersnowski, A. Adsorption, Aggregation, and Desorption of Proteins on Smectite Particles. *Langmuir* **2014,** *30,* 11650-11659.

(15) Servagent-Noinville, S.; Revault, M.; Quiquampoix, H.; Baron, M.H.

Conformational Changes of Bovine Serum Albumin Induced by Adsorption on Different Clay Surfaces: FTIR Analysis. *J. Colloid Interface Sci.***2000,** *221*, 273-283.
(16) Baron, M.H.; Revault, M.; Servagent-Noinville, S.; Abadie, J.; Quiquampoix, H. Chymotrypsin Adsorption on Montmorillonite: Enzymatic Activity and Kinetic FTIR Structural Analysis. *J. Colloid Interface Sci.* **1999,** *214,* 319-332.
(17) Assifaoui, A.; Huault, L.; Maissiat, C.; Roullier-Gall, C.; Jeandet, P.; Hirschingier, J.; Raya, J.; Jaber, M.; Lambert, J.F.; Cayot, P.; Gougeon, R.D.; Loupica, C. Structural studies of adsorbed protein (betalactoglobulin) on natural clay (montmorillonite). *RSC. Adv.* **2014,** *4*, 61096-61103.
(18) Ralla, K.; Sohling, U.; Riechers, D.; Kasper, C.; Ruf, F.; Scheper, T. Adsorption and separation of proteins by a smectitic clay mineral. *Bioproc. Biosyst. Eng.* **2010,** *33,* 847-861.
(19) Vasina, E.N.; Déjardin, P.; Rezaei, H.; Grosclaude, J.; Quiquampoix, H. Fates of Prions in Soil: Adsorption Kinetics of Recombinant Unglycosylated Ovine Prion Protein onto Mica in Laminar Flow Conditions and Subsequent Desorption. *Biomacromolecules* **2005,** *6*, 3425-3432.
(20) Fu. Q.; Deng, Y.; Li, H.; Liu, J.; Hu, H.; Chen, S.; Sa, T. Equilibrium, kinetic and thermodynamic studies on the adsorption of the toxins of *Bacillus thuringiensis* subs. *Kurstaki* by clay minerals. *Appl. Surf. Sci.* **2009,** *255,* 4551-4557.
(21) Mundunkotuwa, I.A.; Minshid, A.A.; Grassian, V.H. ATR-FTIR spectroscopy as a tool to probe surface adsorption on nanoparticles at the liquid-solid interface in environmentally and biologically relevant media. *Analyst* **2014,** *139,* 870-881.
(22) Chiem, L.T.; Huynh, L.; Ralston, J.; Beattie, D.A. An in situ study of polyacrylamide adsorption at the talc surface *J. Colloid Interface Sci.* **2006,** *297,* 54-61.
(23) Depalma, S.; Cowen, S.; Hoang, T.; Al-Abadleh, H.A. Adsorption thermodynamics of p-arsanilic acid on iron (oxyhydr)oxides: in-situ ATR-FTIR studies. *Environ. Sci. Technol.* **2008,** *42,* 1922-1927.
(24) Bouhekka, A.; Bürgi, T. In situ ATR-IR spectroscopy study of adsorbed protein: Visible light denaturation of bovine serum albumin on TiO_2. *Appl. Surf. Sci.* **2012,** *261,* 369-374.
(25) Yang, Y.; Du, J.; Jing, C. Dynamic adsorption process of phthalate at goethite/aqueous interface: An ATR-FTIR study. *Colloids Surf., A* **2014,** *441,* 504-509.
(26) Fredriksson, A.; Holmgren, A. An in situ ATR-FTIR study of the adsorption kinetics of xanthate on germanium. *Colloids Surf., A* **2007,** *302,* 96-101.
(27) Yan, W.; Zhang, J.; Jing, C. Adsorption of Enrofloxacin on montmorillonite: two-dimensional correlation ATR/FTR spectroscopy study. *J. Colloid Interface Sci.* **2013,** *390,* 196-203.
(28) Chittur, K.K. FTIR/ATR for protein adsorption to biomaterial surfaces *Biomaterials* **1998,** *19,* 357-369.
(29) Barth, A.; Zscherp, C. What vibrations tell us about proteins *Q. Rev. of Biophys.* **2002,** *35,* 369-430.
(30) Noda, I. Two-Dimensional Infrared (2D IR) Spectroscopy: Theory and

Applications. *Appl. Spectrosc.* **1990,** *44,* 550-561.
(31) Lu, R.; Li, W.W.; Katzir, A.; Raichlin, Y.; Yu, H.Q.; Mizaikoff. B. Probing the secondary structure of bovine serum albumin during heat-induced denaturation using mid-infrared fiberoptic sensors. *Analyst* **2015,** *140,* 765-770.
(32) Kunze, G.W.; Dixon, J.B. Pretreatment for Mineralogical Analysis. In *Methods of Soil Analysis; Part 1-Physical and Mineralogical Methods*; Klute, A., Ed.; Soil Science Society of America: Madison, W.I., 1986; pp 91-99.
(33) Mackenzie, R.C. Free iron-oxide removal from soils. *J. Soil Sci.* **1954,** *5,* 167-172.
(34) Whittig, L.D.; Allardice, W.R. X-Ray Diffraction Techniques. In *Methods of Soil Analysis; Part 1-Physical and Mineralogical Methods*; Klute, A., Ed.; Soil Science Society of America: Madison, W.I., 1986; pp 331-362.
(35) Stuckey, J.W. Highly Charged Swelling Mica Reduces Exchangeable and Bioavailable Cu in Cu Contaminated Soils. M.S. Thesis, The Pennsylvania State University, University Park, PA, 2007.
(36) Johnston, C.T.; Premachandra, G.S. Polarized ATR-FTIR Study of Smectite in Aqueous Suspension. *Langmuir* **2001,** *17,* 3712-3718.
(37) Ho, Y.S. Review of second-order models for adsorption systems. *J. of Hazard. Mater.* **2006,** *136,* 681-689.
(38) Plazinski, W.; Rudzinski, W.; Plazinska, A. Theoretical models of sorption kinetics including a surface reaction mechanism: A review. *Adv. Colloid Interface Sci.* **2009,** *152,* 2-13.
(39) Lagergren, S. Zur theorie der sogenannten adsorption gelöster stoffe. *Kungliga Svenska Vetenskapsakademiens Handligar* **1898,** *24,* 1-39.
(40) Aharoni, C.; Tompkins, F.C. Kinetics of Adsorption and Desorption and the Elovich Equation. *Adv. Catal.* **1970,** *21,* 1-49.
(41) Ho, Y.S.; Ng, J.C.Y.; McKay, G. Kinetics of Pollutant Sorption by Biosorbents: Review. *Separ. Purif. Method.* **2000,** *29,* 189-232.
(42) Degenhardt, J.; McQuillan, J. In Situ ATR-FTIR Spectroscopic Study of Adsorption of Perchlorate, Sulfate, and Thiosulfate Ions onto Chromium (III) Oxide Hydroxide Thin Films. *Langmuir* **1999,** *15,* 4595-4602.
(43) Czarnik-Matusewicz, B.; Murayama, K.; Wu, Y.; Ozaki, Y. Two-Dimensional Attenuated Total Reflection/Infrared Correlation Spectroscopy of Adsorption-Induced and Concentration-Dependent Spectral Variations of β-Lactoglobulin in Aqueous Solutions. *J. Phys. Chem. B* **2000,** *104,* 7803-7811.
(44) Roach, P.; Farrar, D.; Perry, C.C. Interpretation of Protein Adsorption: Surface-Induced Conformational Changes. *J. Am. Chem. Soc.* **2005,** *127,* 8168-8173.
(45) Madejová, J.; Komadel, P. Baseline studies of the clay mineral society source clays: Infrared methods. *Clays Clay Miner.* **2001,** *49,* 410-432.
(46) Grdadolinik, J.; Maréchal, Y. Bovine Serum Albumin Observed by Infrared Spectrometry. I. Methodology, Structural Investigation, and Water Uptake. *Biopolymers* **2001,** *62,* 40-53.
(47) Zhang, J.; Stanforth, R. Slow Adsorption Reaction between Arsenic Species and Goethite (α-FeOOH): Diffusion or Heterogeneous Surface Reaction Control. *Langmuir* **2005,** *21,* 2895-2901.

(48) Cerofolini, G. In *Adsorption Kinetics. Encyclopedia of Surface and Colloid Science*; Marcel Dekker, Inc.; New York, 2002; pp 225-239.
(49) Asanov, A.N.; DeLucas, L.J.; Oldham, P.B.; Wilson, W.W. Heteroenergetics of Bovine Serum Albumin Adsorption from Good Solvents Related to Crystallization Conditions. *J. Colloid Interface Sci.* **1997,** *191,* 222-235.
(50) Kulik, E.A.; Kalinin, I.D.; Sevastianov, V.I. The Heterogeneity of Protein/Surface Interactions and Structural Alterations of Adsorbed Albumin and Immunoglobulin G. *Artif. Organs* **1991,** *15,* 386-391.
(51) Cai, Y.; Schwartz, D.K. Influence of Protein Surface Coverage on Anomalously Strong Adsorption Sites. *ACS Appl. Mater. Interfaces* **2016,** *8,* 511-520.
(52) Lepoitevin, M.; Jaber, M.; Guégan, R.; Janot, J.M.; Déjardin, P.; Henn, F.; Balme, S. BSA and lysozyme adsorption on homoionic montmorillonite: Influence of the interlayer cation. *Appl. Clay Sci.* **2014,** *95,* 396-402.
(53) Norde, W.; MacRitchie, F.; Nowicka, G.; Lyklema, J. Protein Adsorption at Solid-Liquid Interfaces: Reversibility and Conformation Aspects. *J. Colloid Interface Sci.* **1986,** *112,* 447-456.
(54) Murayama, K.; Tomida, M. Heat-Induced Secondary Structure and Conformation Change of Bovine Serum Albumin Investigated by Fourier Transform Infrared Spectroscopy. *Biochemistry* **2004,** *43,* 11526-11532.
(55) Perticaroli, S.; Nickels, J.D.; Ehlers, G.; Sokolov, A.P. Rigidity, Secondary Structure, and the Universality of the Boson Peak in Proteins. *Biophys. J.* **2014,** *106,* 2667-2674.
(56) Czarnecki, M.A. Interpretation of Two-Dimensional Correlation Spectra: Science or Art? *Appl. Spectrosc.* **1998,** *52,* 1583-1590.
(57) Haynes, C.A.; Norde, W. Structures and Stabilities of Adsorbed Proteins. *J. Colloid Interface Sci.* **1995,** *169,* 313-328.
(58) Lecomte, S.; Hilleriteau, C.; Forgerit, J.P.; Revault, M.; Baron, M.H.; Hidebrandt, P.; Soulimane, T. Structural Changes of Cytochrome c_{552} from *Thermus thermophilus* Adsorbed on Anionic and Hydrophobic Surfaces Probed by FTIR and 2D-FTIR Spectroscopy. *ChemBioChem* **2001,** *2,* 180-189.
(59) Roberts, P.; Jones, D.L. Critical evaluation of methods for determining total protein in soil solution. *Soil Biol. Biochem.* **2008,** *40,* 1485-1495.
(60) Burns, R.G.; Deforest, J.L.; Marxsen, J.; Sinsabaugh, R.L.; Stromberger, M.E.; Wallenstein, M.D.; Weintraub, M.N.; Zoppini, A. Soil enzymes in a changing environment: Current knowledge and future directions. *Soil. Biol. Biochem.* **2013,** *58,* 216-234.

CHAPTER THREE

Ironing out Genes in the Environment: An Experimental Study of the DNA-Goethite Interface

Introduction

Deoxyribonucleic acid (DNA) represents a biomolecule used for the transfer and storage of genetic information, making it critical for the functioning of cells. Through cellular lysis, active secretion and grazing of microbes and senescence of leaves/roots in plants, DNA may be released into the surrounding environment.[1] In natural systems, such as soil and water, DNA may adsorb strongly onto colloidal mineral surfaces, which may profoundly influence its environmental behavior.[1-3] Over the past few decades, numerous studies have demonstrated protection of DNA from nucleases by adsorption onto inorganic colloids, including sand, model clays and whole soils.[1-7] This allows for persistence of DNA in conditions that would otherwise be unfavorable for DNA stability. Furthermore, DNA adsorbed to mineral colloids may retain the ability to transfer genetic information to active microbiota despite close association with mineral surfaces.[1-3, 8,9] This has been observed for a plasmid DNA containing an *nptII* gene, which carries resistance for the widely-used antibiotic kanamycin, adsorbed on clay minerals. Upon adsorption onto kaolinite, illite and montmorillonite, the plasmid was partially protected from degradation by nucleases, yet was still available to transform a strain of *Acinetobacter*.[9] Another study demonstrated the ability of the chloramphenicol resistance carrying plasmid pHV14 to transform *B. subtilis* despite being mineral (montmorillonite and kaolinite) bound.[10]

Additionally, adsorbed pHV14 continued to maintain the ability to transform *B. subtilis* despite wet-dry cycling, albeit to a lower extent.[10] Reduction in transformative ability was hypothesized to be a result of conformational changes in DNA associated with multiple reiterations of wet-dry cycles.[10] Adsorption of DNA onto soil minerals has also been suggested to play a role in the transport of DNA in soils, with type of soil particles and adsorption time as particularly important influence of DNA movement in subsoils.[11,12] These points highlight the impact of underlying adsorption processes on the propagation and fate of genetic information in environmental systems.

Goethite (α-FeOOH), an iron oxyhydroxide mineral commonly found in soils and sediments, readily adsorbs DNA.[13-15] Additionally, DNA adsorbed on goethite is more susceptible to PCR amplification, relative to montmorillonite, kaolinite and clay fractions isolated from whole soils, suggesting the adsorption of DNA onto goethite is particularly relevant to DNA behavior in soils.[8] Despite the significance of DNA adsorption onto goethite, the adsorption process itself has not been well characterized. Experiments probing DNA adsorption onto goethite rely on bulk measurements (e.g. batch adsorption studies, calorimetric measurements) to infer adsorption mechanisms rather than investigating the interface directly.[13-15] From previous bulk adsorption experiments, it was suggested that DNA adsorption onto goethite follows a Langmuir-type adsorption and results in ligand exchange between DNA backbone phosphoester groups and surface hydroxyl groups on goethite.[14,16] While another Fourier transform infrared (FTIR) spectroscopic investigation of adsorption of a suite of P-containing biomolecules to hematite and goethite alludes to this mechanism by showing

phosphate groups of organics adsorb strongly onto Fe-oxides, further characterization of the DNA-goethite interface is lacking.[17] To the best of our knowledge, a quantitative description of the surface coverage, kinetic parameters and structural changes associated with the adsorption of DNA onto goethite is notably absent from previous studies. A focused study on the adsorption mechanism, taking into account these fundamental considerations of surface processes, is needed to assess the environmental chemistry of DNA in soils.

To address this void in knowledge, surface sensitive *in situ* attenuated total reflectance Fourier transform infrared (ATR-FTIR) and X-ray photoelectron (XPS) spectroscopies are applied to characterization of the DNA-goethite interface. Previous application of XPS to the characterization of biomolecule/mineral interfaces has yielded insight into the behavior of biomolecules at mineral surfaces by probing biomolecule surface coverage and chemical bonding information.[18-20] *In situ* ATR-FTIR is also applicable to the study of biomolecule/mineral interfaces under environmentally relevant conditions (i.e. in solution and in real time).[21] Specifically, this technique has been used to study kinetic, conformational and surface coverages related to biomolecule adsorption onto mineral surfaces.[22-24] This technique, as a form of FTIR, is particularly suitable for probing DNA adsorption, as FTIR can readily distinguish between different double-stranded DNA conformations. Different DNA conformations include the right-handed B-form helix (3.4 Å rise per base pair, 10.5 base pairs per turn), the more compact A-form helix (2.6 Å rise per base pair, 11 base pairs per turn) and the more extended, left-handed Z-form helix (3.7 Å rise per base pair, 12 base pairs per turn). The ability to distinguish between these forms of DNA

helices is of importance, as helical DNA has been demonstrated to change form upon adsorption to mineral surfaces.[4] Furthermore, DNA forms have different major and minor groove dimensions, which can influence protein interaction with and recognition of DNA.[25] The objective of this work is to employ surface sensitive in situ ATR-FTIR and XPS spectroscopic methods to better understand the DNA/goethite interface by probing the kinetics, equilibrium behavior and conformational implications of DNA adsorption onto goethite under environmentally relevant conditions. Furthermore, these results will be used to interpret the state of DNA at the goethite interface and to discuss the role of DNA adsorption onto minerals on the environmental fate of DNA.

Materials and Methods

Materials Double-stranded herring testes DNA (B-form, Type XIV, Sigma Aldrich prod. No. D6898) was used in all experiments. Prior to use, DNA was ultrasonically sheared to a shorter length (≈ 400 bp) and more uniform size distribution (Figure S1). Sonication of DNA was performed using a 550W Misonix XL2020 Ultrasonic Processor (Misonix Incorporated, Farmington NY) at about 25% output. Sonication was carried out by 12 repetitions of a 30 s pulse sequence followed by a 60 s pause for a total of 6 min of sonication time. Throughout sonication, DNA solution was kept in an ice water bath to prevent sample denaturation. This yielded DNA with a length ≈ 400 bp, as characterized by agarose gel (1.5%) electrophoresis (**Figure A3.1**). To maintain conditions representative of soil solution (i.e. low ionic strength and moderately acidic pH), DNA solutions were prepared in 0.005 M KCl electrolyte at pH = 5.00. All solutions were made with distilled-deionized water (18.2 MΩ).

Goethite was synthesized using the method of Schwertmann and Cornell.[26] Synthesis resulted in needle shaped particles ranging from one to a few micrometers in length, as observed by scanning electron microscopy (**Figure 3.1**). Purity of the synthesized material was verified by FTIR spectroscopy (**Figure A3.2**) and the surface area was determined to be 56.6 m^2/g by N_2 adsorption.

In-situ ATR-FTIR adsorption experiments Goethite thin films used in experiments were made using a previously described approach.[27] Briefly, a suspension of 1.12 g/L goethite was made in 0.01 M KCl and adjusted to pH = 4.50. The suspension was then placed in a sonication bath for around 30 minutes and re-adjusted to pH = 4.50. Four μL of the sonicated suspension was then drop cast onto the diamond IRE and dried under N_2 flow. This resulted in a thin, evenly-distributed and slightly opaque layer of goethite. After creating a goethite film, background solution was passed over the film until no detectable changes to the FTIR spectrum were observed (1.5-2 hours). DNA solution was introduced after collection of background spectra, with a series of concentrations (0.001, 0.0025, 0.005, 0.01, 0.05, 0.1 and 0.5 mg/mL) used for in-situ experiments. Experimental values represent duplicate except for 0.05 and 0.1 mg/mL DNA, which were run in triplicate due to observed variability. FTIR spectra were collected on a Vertex 70 FTIR spectrometer (Bruker Corp., Billerica, MA) equipped with a DLaTGS detector. A single reflection Pike GladiATR accessory (Pike Technologies, Madison, WI) with a diamond internal reflection element was used for sampling. Spectra were averaged over 200 scans with 4 cm^{-1} resolution. Spectra received post-hoc atmospheric correction, smoothing (9 point Savitzky-Golay) and baseline correction. Adsorption kinetic data was fitted in SigmaPlot 13.0 (Systat

Software, Inc.) by non-linear fitting. Equilibrium isotherms were fitted using a non-linear approach in Excel using the Solver add-in.

XPS analysis of adsorbed DNA Samples for XPS experiments were prepared using a batch adsorption approach, with a fixed amount of goethite (10 mL of a 2 g/L suspension), different concentrations of DNA (0.0130, 0.033, 0.065, 0.13 and 0.65 mg/mL) and the same background solution as ATR-FTIR experiments. Duplicate samples were shaken for 6 h (determined adequate by a preliminary batch experiment) with periodic adjustment of pH to maintain a constant value. After equilibration, suspensions were centrifuged at 10000 RPM (9000 rcf) for 5 minutes. DNA concentration in the supernatants was analyzed using UV/Vis spectrophotometry by measuring the 260 nm peak area, corresponding with DNA in solution. Pellets were combined, resuspended in background solution and centrifuged to remove excess DNA. This material was streaked onto Si shards and dried for XPS analysis. Samples were analyzed using a Surface Science Instruments SSX-100 with operating pressure ~$2x10^{-9}$ Torr. Monochromatic Al Kα x-rays (1486.6 eV) with 1 mm diameter beam size was used with a 55° emission angle. A hemispherical analyzer determined electron kinetic energy, using a pass energy of 150 V for wide/survey scans, and 50 V for high resolution scans of the C 1s, N 1s, O 1s and P 2p regions. High resolution scans were energy calibrated to the primary C 1s peak at 285.0 eV. A flood gun was used for charge neutralization of non-conductive samples. Quantification and peak fitting of high resolution XPS spectra was performed using CasaXPS (Casa Software, Ltd. Version 2.3.18). Equilibrium isotherms were fitted using a non-linear approach in Excel using the Solver add-in. Surface coverage of DNA on goethite was determined

by %N/%Fe from survey scans of samples (**Figure A3.3**, **Table 3.1**). Nitrogen serves as the elemental probe for DNA, as it is not present in the substrate or adventitious hydrocarbon contamination that may arise during analysis. High resolution scans of N 1s and P 2p are used to identify structural changes of DNA upon adsorption.

Results and Discussion

Adsorption kinetics Kinetics of DNA adsorption onto goethite for each concentration were followed by the absorbance of the backbone ν C-C (≈ 970 cm^{-1}) mode from FTIR spectra with time (**Figures 3.2-3** and **A3.4** and **Table A3.1**).[28-31] This peak was selected as it was present in all spectra at the same position and represents a group unlikely to play an active role in adsorption, which may alter peak character. Adsorption reaches equilibrium within 95 minutes under experimental conditions with kinetics well described by Lagergren's pseudo-first order adsorption kinetic model, of which a modified form is given as:[32,33]

$$A_t = A_{max}(1 - e^{-k_1 t})$$

where A_t is ν C-C peak absorbance (a.u.) at time = *t* (min), A_{max} is ν C-C peak absorbance (a.u.) at equilibrium and k_1 is the pseudo-first order rate constant (min^{-1}). This suggests adsorption rates are limited by energetic barriers associated with surface adsorption (e.g. bond breaking, dehydration, rearrangement, electrostatic barriers), as opposed to mass transport limitations. Adsorption rate constants (k_1) generally increase with increasing DNA concentration (**Table A3.2**), ranging from 3.29 x 10^{-2} min^{-1} when [DNA] = 0.001 mg/mL up to 3.55 x 10^{-1} min^{-1} when [DNA] = 0.5 mg/mL. The predicted maximum ν C-C peak absorbance values (A_{max}) correspond well with experimental data, highlighting the suitability of the pseudo-first order model for

describing DNA adsorption onto goethite under these conditions.

Adsorption isotherms Adsorption isotherms and models yielded from equilibrium ν C-C absorbance values (FTIR) and %N/%Fe (XPS) are shown in **Figure 3.4**. Adsorption is well described by the Langmuir isotherm model, given by the following equation:[34]

$$\theta = \frac{Kc}{1 + Kc}$$

where θ is given fraction of adsorption sites occupied at concentration = c and K is the equilibrium adsorption coefficient. Parameters yielded from the Langmuir model are presented in the supplementary information (**Table A3.3**). Isotherms from FTIR and XPS yield K values of 1.23×10^3 and 9.48×10^2 mL/mg, respectively. The isotherm is suggestive of high affinity adsorption behavior, with a steep initial slope until [DNA] ≈ 0.02 mg/mL after which surface saturation is approached. This result is reflected in both XPS and FTIR derived adsorption isotherms, as they agree closely when plotting on a common scale (θ versus DNA concentration). Comparison to adsorption isotherms of DNA on gold surfaces from XPS and FTIR data also show remarkable similarity despite their physically distinct methods of probing matter.[35] Existing bulk studies of DNA adsorption onto goethite show a lower initial slope, corresponding with a lower affinity of DNA for goethite than this work. This may be the result of a range of pH and ionic strength values being used. Generally, DNA adsorbs more strongly with lower pH and higher ionic strength. These conditions are suggested to reduce electrostatic repulsion between negatively charged backbone phosphate groups of adsorbed DNA and/or surface groups, allowing for more DNA to be

accommodated.[36] DNA adsorption to goethite is sensitive to these factors, perhaps yielding a different affinity when those factors are taken into account.[9] It is also possible that the use of sheared DNA may increase the surface affinity, as smaller DNA molecules have been demonstrated to adsorb more strongly to soil particles than longer DNA molecules.[37]

Structure of DNA adsorbed on goethite High resolution N 1s and P 2p XPS spectra of DNA adsorbed to goethite and a DNA solid standard are shown in **Figures 3.5** and **A3.5**. P 2p spectra of DNA adsorbed onto goethite and standard show two main components, both attributable to P in the backbone phosphate groups of DNA. Due to spin-orbit splitting, the P 2p peak is represented by a doublet of peaks, which arise from $2p_{1/2}$ and $2p_{3/2}$ spin orbit peaks.[38] For the DNA standard, the 2p peak is centered at 132.4 eV with the $2p_{1/2}$ and $2p_{3/2}$ peaks at 133.0 and 132.2 eV, respectively. DNA adsorbed on goethite at the highest experimental surface coverage has a 2p peak centered at 133.1 eV with the $2p_{1/2}$ and $2p_{3/2}$ components at 133.8 and 132.9 eV, respectively, representing a P 2p binding energy increase of 0.7 eV. P 2p peaks for other surface coverages range from 133.8 to 134.0 eV, exhibiting a binding energy increase for all surface coverages studied. An increase in binding energy suggests that P in the backbone phosphate groups experiences a greater extent of electron withdrawal upon adsorption onto goethite. This reflects an active role of backbone phosphate groups in the binding of DNA onto goethite. Previous XPS studies probing the interaction of phosphate with ferrihydrite indicate that an increase in P 2p binding energy by 0.7 eV upon adsorption is the result of Fe-O-P bond formation.[39] This corresponding result suggests direct coordination of the DNA phosphate backbone

groups is occurring upon adsorption.

The N 1s peak of the DNA standard has two components, 400.3 and 398.7 eV, corresponding with non-conjugated (-NH- and saturated N) species and conjugated N structures of DNA nucleobases, respectively.[40,41] Similar features are observed in N 1s spectra of adsorbed DNA, although with some difference in relative proportion of each component peak. Generally, the ratio of conjugated to non-conjugated peak areas decreased with increasing DNA surface coverage (**Table A3.4**, **Figure A3.5**). While these changes are observed, it is unlikely the nucleobases play an active role in DNA binding to goethite under experimental conditions. Binding of nucleobases to surfaces and metal ions results in dramatic changes to existing peak profiles and would be accompanied by appearance of satellite peaks in the N 1s spectrum.[35, 41, 42] Both indicators are absent here, suggesting nucleobases do not directly bind goethite.

ATR-FTIR spectra of DNA adsorbed on goethite and in solution support XPS results (**Figures 3.2**, **A3.6**). Upon adsorption, the backbone ν_{as} PO_4^- peak shifts from 1224 to 1218 cm^1, indicative of backbone PO_4^- interaction with the goethite surface. This agrees with FTIR spectra of DNA adsorption on $CoFe_2O_4$ and layered Mg/Fe hydroxide nanoparticles, which induced small bathochromic shifts in ν_{as} PO_4^- through surface coordination.[43, 44] While a shift in ν_{as} PO_4^- to 1218 cm^{-1} could potentially be interpreted as a change of DNA to a Z-form conformation upon adsorption, other major Z-form indicators, such as a Z-form specific C-C mode ≈1413-1408 cm^{-1} and the Z-form marker at 1123 cm^{-1}, are notably absent in spectra.[29, 45] This suggests DNA adsorbed on goethite retains B-form conformation. In addition to a shift in the ν_{as} PO_4^- peak, adsorbed DNA also develops a peak around 1010 cm^{-1} which is tentatively

assigned to inner-sphere ν Fe-O-P.[19,20] Previous theoretical studies probing the adsorption of a model phosphodiester bond of a nucleic acid also suggests the presence of a peak at 1009 cm^{-1} for monodentate coordination on a goethite surface.[46] It should be noted, however, that ν Fe-O-P modes at 1015 cm^{-1} (close to observed experimental values in this study) have previously been assigned to bidentate bridging of the phosphonate group of methylphosphonic acid with goethite.[47] Further evidence for interaction of the backbone PO_4 group with goethite can be found near 1068 cm^{-1}, where DNA adsorbed on goethite at many surface coverages develops a feature (**Figure 3.6**). Calculated frequencies of monodentate complexes adsorbed on goethite highlight features close to this value (1067 cm^{-1}).[46] This study also suggests that formation of a monodentate Fe-O-P bond is energetically more favorable than bidentate coordination, perhaps making a monodentate complex more likely in our study.[46] There appears to be some dependence of equilibrium DNA concentration/surface coverage on the relative intensities of peaks at 1068 and 1010 cm^{-1} (**Figure 3.6**). The intensity of the 1010 cm^{-1} peak increases with surface coverage, possibly suggesting a greater extent of Fe-O-P bond formation with increasing DNA adsorption. The feature near 1068 cm^{-1} shows a less clear relationship with increasing amounts of adsorbed DNA, with the peak becoming generally more pronounced up to DNA adsorbed at [DNA] = 0.1 mg/mL, then becoming a weaker peak at [DNA] = 0.5 mg/mL. While this may represent a variance in bonding mechanism between DNA adsorbed at lower and higher surface coverages, no attempt is made to attribute observed discrepancies to specific mechanisms given the ambiguity of Fe-O-P peak assignments in this region. Despite this ambiguity, it can be

concluded from ATR-FTIR that inner sphere Fe-O-P bonds form upon DNA adsorption onto goethite and monodentate complexation is the tentative mechanism. Overall, these results correspond with XPS P 2p spectra, which also emphasize the role of inner-sphere complexation on DNA adsorption.

The region of FTIR spectra associated with nucleobase vibrations (**Table A3.1**) shows minor shifts in frequencies, but there is no evidence of strong interaction between nucleobases and goethite or degradation of the helical structure of DNA on the goethite surface. As with the N 1s XPS spectra, lack of major changes or shifts in the spectral landscape associated with the nucleobases underlines the important role of phosphate groups on the adsorption of DNA onto goethite.

Conclusions

Spectroscopic characterization of DNA adsorbed on goethite corresponds well with kinetic and equilibrium adsorption data. Adherence to pseudo-first order adsorption kinetics suggests that adsorption is limited by surface processes. Spectroscopic results support this conclusion by demonstrating Fe-O-P bond formation during DNA adsorption onto goethite. It is likely that barriers associated with forming this bond are rate limiting, as other potential surface limitations are either not detectable (dehydration, conformational change) or unfavorable (electrostatic barriers between molecule and surface). Inner-sphere complexation of DNA with goethite corresponds with the high affinity adsorption isotherms observed in this study.[48, 49] Given the high affinity nature of the adsorption isotherm, it is likely that goethite would strongly adsorb DNA in the environment, even at low concentrations of DNA expected in surface and soil waters, with values of 1.5 μg/L in

soil water and up to 72 μg/L in lake water previously observed.[50,51] The high affinity of DNA for goethite observed in this experiment and the poor desorbability of DNA adsorbed on goethite demonstrated previously both suggest DNA mobility in soils and sediments could likely be impacted by goethite.[8,52] This could have implications for the transport of DNA in soils and sediments where goethite may be present, with goethite potentially limiting movement of DNA. It is also possible, given the small size of colloidal goethite, that strong adsorption of DNA to goethite could enhance the mobility of DNA in soils. Colloid facilitated transport may play an important role in the movement of molecules in soil, particularly when considering the transport of molecules that bind strongly to mineral or organic colloids.[53] The observed strong adsorption of DNA onto colloidal goethite particles may enhance transport in systems where colloids are likely to be mobilized (i.e. low ionic strength, presence of monovalent electrolytes, high rainfall) as a result of strong association with goethite, rather than hindered in movement.[54]

These results are in line with the protective nature of mineral surfaces toward biomolecules (such as DNA), as formation of the inner-sphere Fe-O-P bond may provide some degree of stability. Chemical association between biomolecules and mineral surfaces is believed to impart a certain degree of stabilization to the adsorbed biomolecule due to protection from microbial attack.[55,56] This may partially explain the persistence of DNA in soil, however the resistance of DNA to enzymatic degradation has also been attributable to adsorption and deactivation of nucleases on mineral surfaces.[4,9] In this instance, further work probing the direct surface interaction of nucleases with minerals may yield additional insight on DNA preservation beyond

observed bond formation. Additionally, retention of the double-stranded, B-form upon DNA adsorption to goethite may inform understanding of the protective behavior of mineral surfaces toward DNA. Widespread single-strand specific nucleases will degrade only single-stranded forms of DNA[57], suggesting that goethite surfaces may prevent degradation under some circumstances as a result of retaining the double-stranded form, even if adsorbed DNA is accessible. Retention of the helical, B-form conformation of adsorbed DNA may influence the ability of DNA adsorbed on goethite to transform organisms. Previous work suggests that a decrease in transformative ability of DNA, albeit linked to wetting and drying, was likely the result of DNA conformational changes on mineral surfaces relative to the conformation in solution.[10] It is conceivable that a mineral surface which fosters retention of solution conformation potentially would maintain a higher ability to transform microorganisms than a mineral surface which does not (e.g. kaolinite).[4,10] Additionally, transformation is a process that initiates by binding of DNA by bacterial proteins, with varying extent of specificity.[58] Maintaining the B-form and associated groove structure could possibly allow this critical first step in transformation to occur, or occur more favorably, depending upon binding proteins utilized, as grooves in DNA helices serve as important sites for protein recognition and binding to DNA.[25]

Acknowledgements

This work made use of the Cornell Center for Materials Research Shared Facilities which are supported through the NSF MRSEC program (DMR-1120296). Partial funding provided by the Cornell University Program in Cross-Scale Biogeochemistry

and Climate, which is supported by NSF-IGERT (NSF award number: 1069193) and the Atkinson Center for a Sustainable Future. Additional support was provided by the School of Integrative Plant Science within the College of Agriculture and Life Sciences at Cornell University. M.P.S. would also like to acknowledge Akio Enders and Dr. Francis DiSalvo for surface area measurement of goethite and Mick Thomas for assistance with SEM imaging.

Table 3.1 Atom % N and Fe values from survey scans for each experimental concentration.

Equilibrium DNA concentration (mg/mL)	**% N**	**% Fe**	**% N/% Fe**
0 (goethite)	0	16.16	0
2.12×10^{-4}	1.19	11.99	0.10
2.26×10^{-4}	3.05	15.26	0.20
1.57×10^{-3}	4.89	12.35	0.40
5.85×10^{-2}	5.35	7.98	0.67
5.14×10^{-1}	5.57	7.41	0.75

Figure 3.1 Scanning electron microscopy image of goethite particles used in adsorption experiments. The scale bar represents 1 μm length.

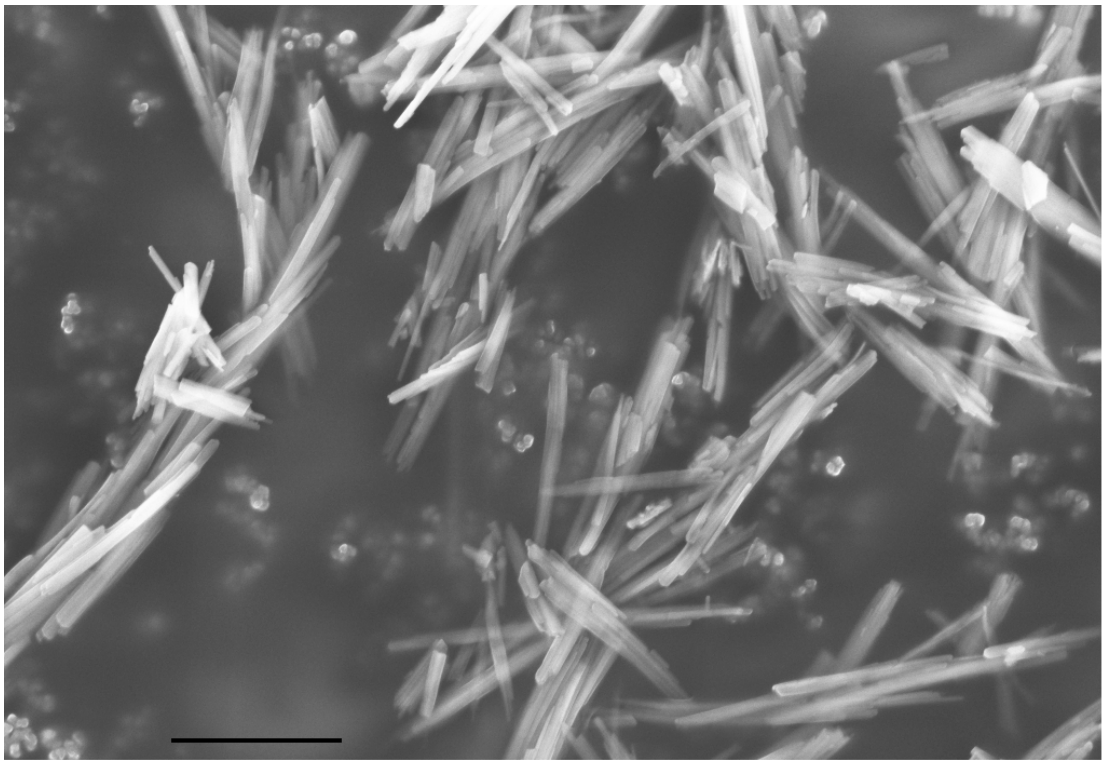

Figure 3.2 ATR-FTIR spectra of 5 mg/mL DNA in solution (top) and 0.005 mg/mL DNA adsorbed on goethite at 7 (red), 11 (blue), 19 (orange) and 99 (black) minutes. Position of potential Z-form marker bands shown by dashed lines.

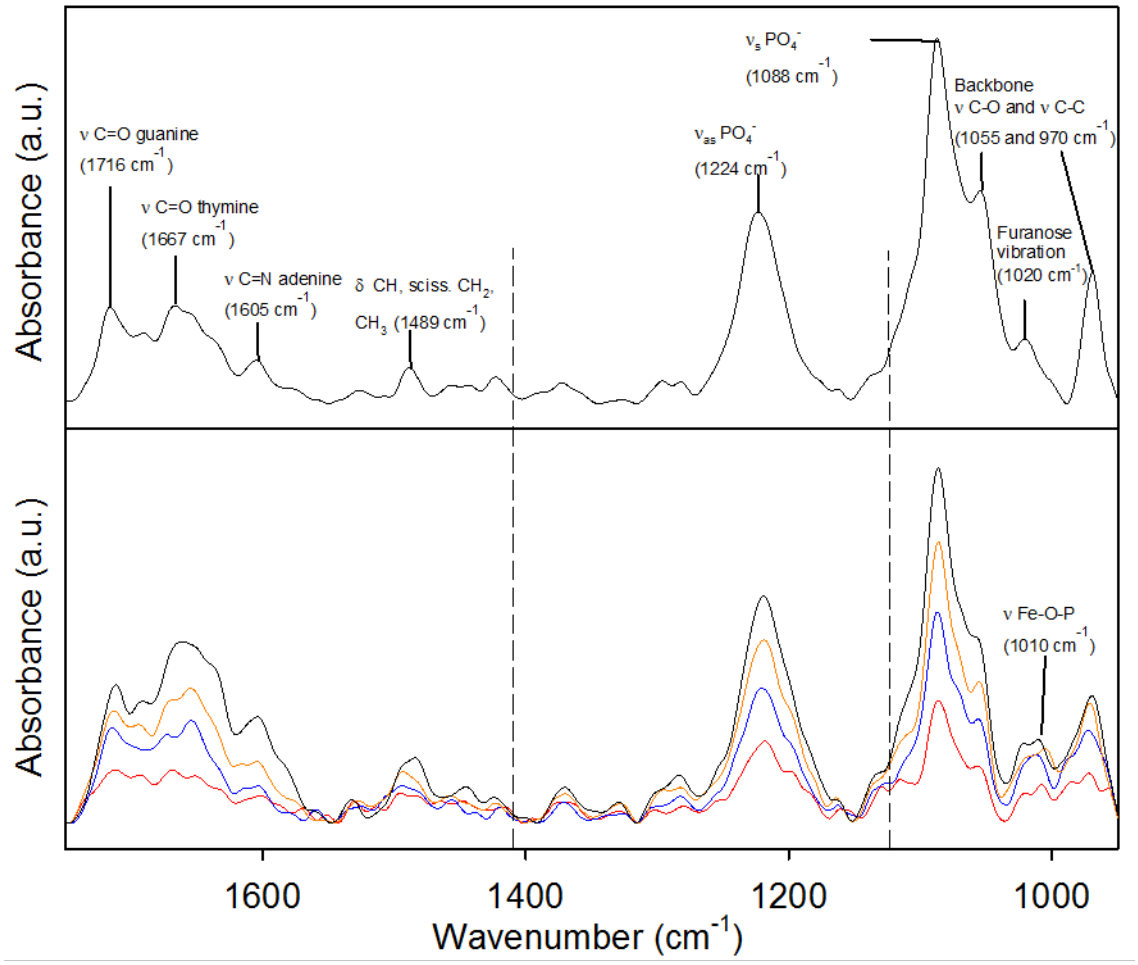

Figure 3.3 Kinetics of DNA adsorption onto goethite for [DNA] = 0.001, 0.005, 0.05 and 0.5 mg per mL (from bottom to top). Additional concentrations have been omitted for clarity with remaining kinetic plots included in the supplementary information (Figure S4).

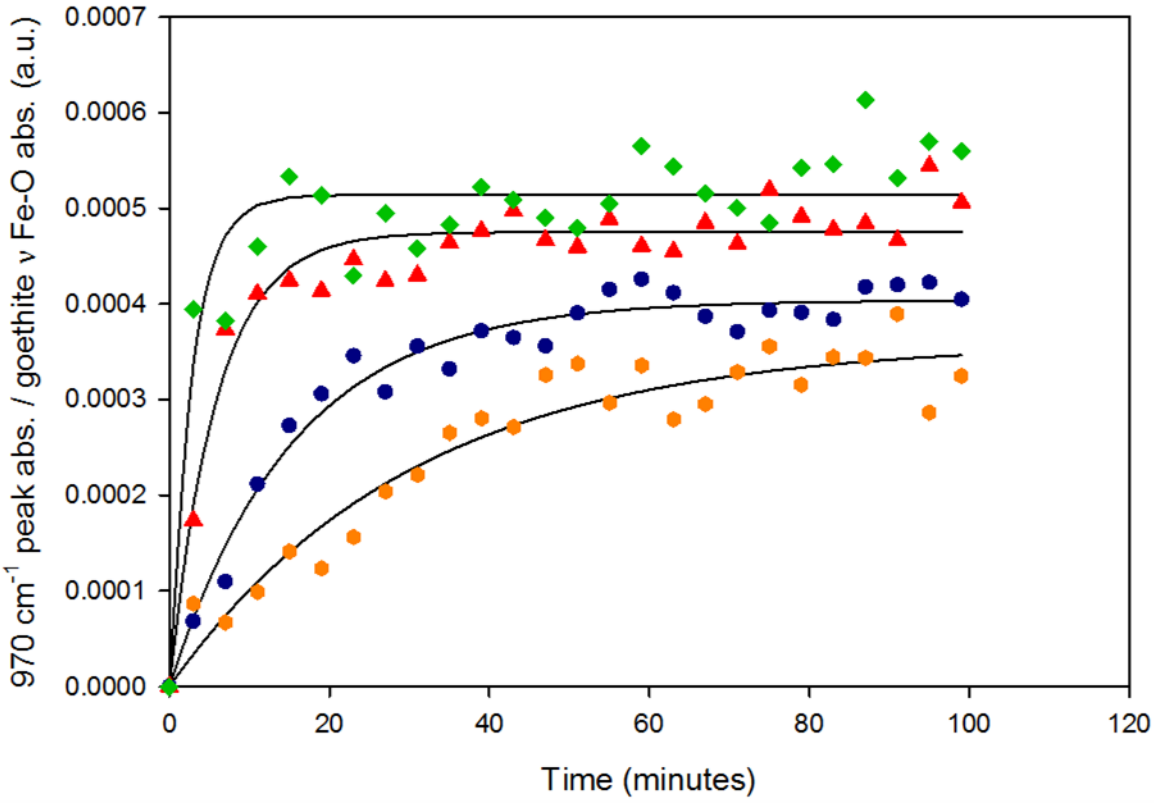

Figure 3.4 Experimental adsorption isotherms from FTIR (red triangles) and XPS (black diamonds) with error bars corresponding with standard deviations in equilibrium absorbance (FTIR) and concentration (XPS). Langmuir isotherm models derived from FTIR (solid red line) and XPS surface coverages (dotted black circles) are included.

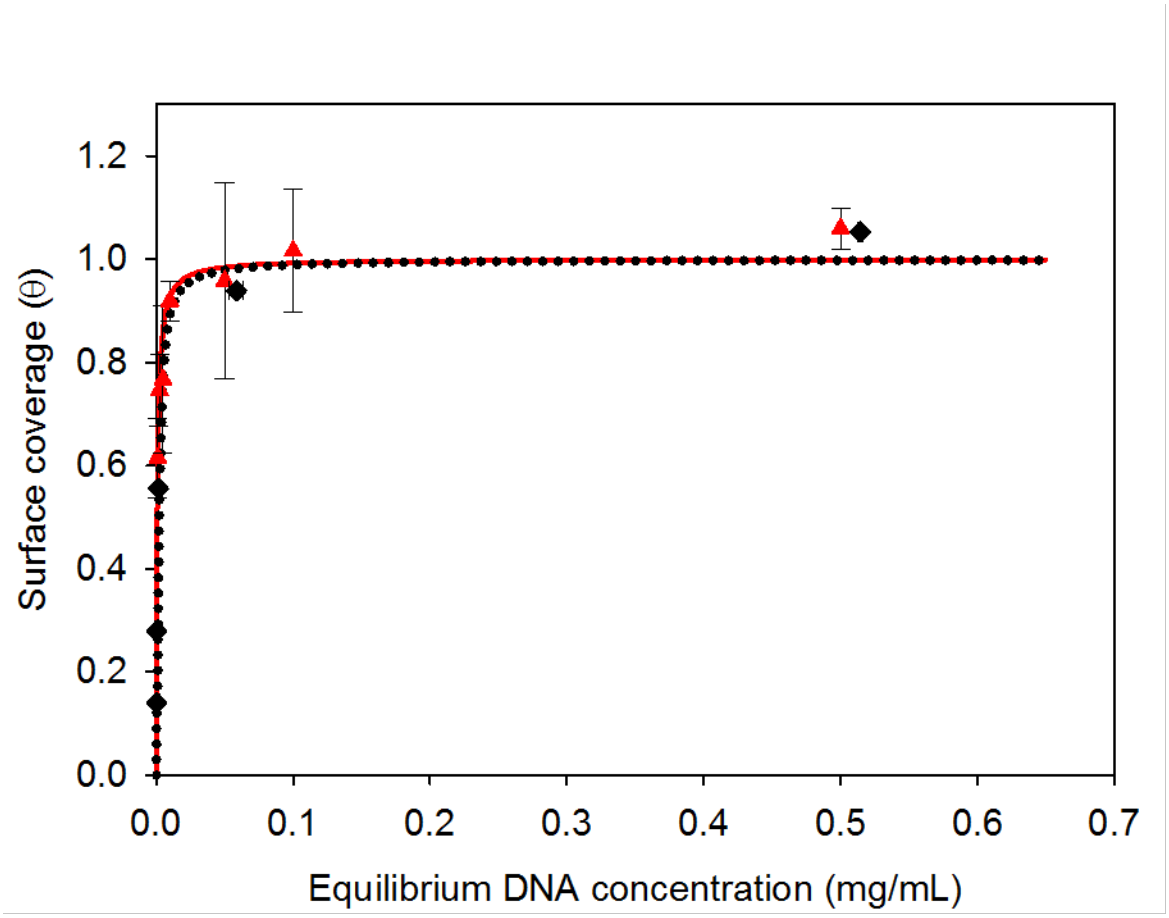

Figure 3.5 High resolution N1s (left) and P2p (right) XPS spectra for a DNA standard and DNA adsorbed on goethite at highest surface coverage (at [DNA] = 5.14 x 10^{-1} mg/mL) in XPS experiments. Spectra (solid black lines), peak components (solid colored lines) along with summed components (long dashed line) and background (dotted-dashed lines) are shown. High resolution scans for other surface coverages are included in the supplementary information (Figure S5).

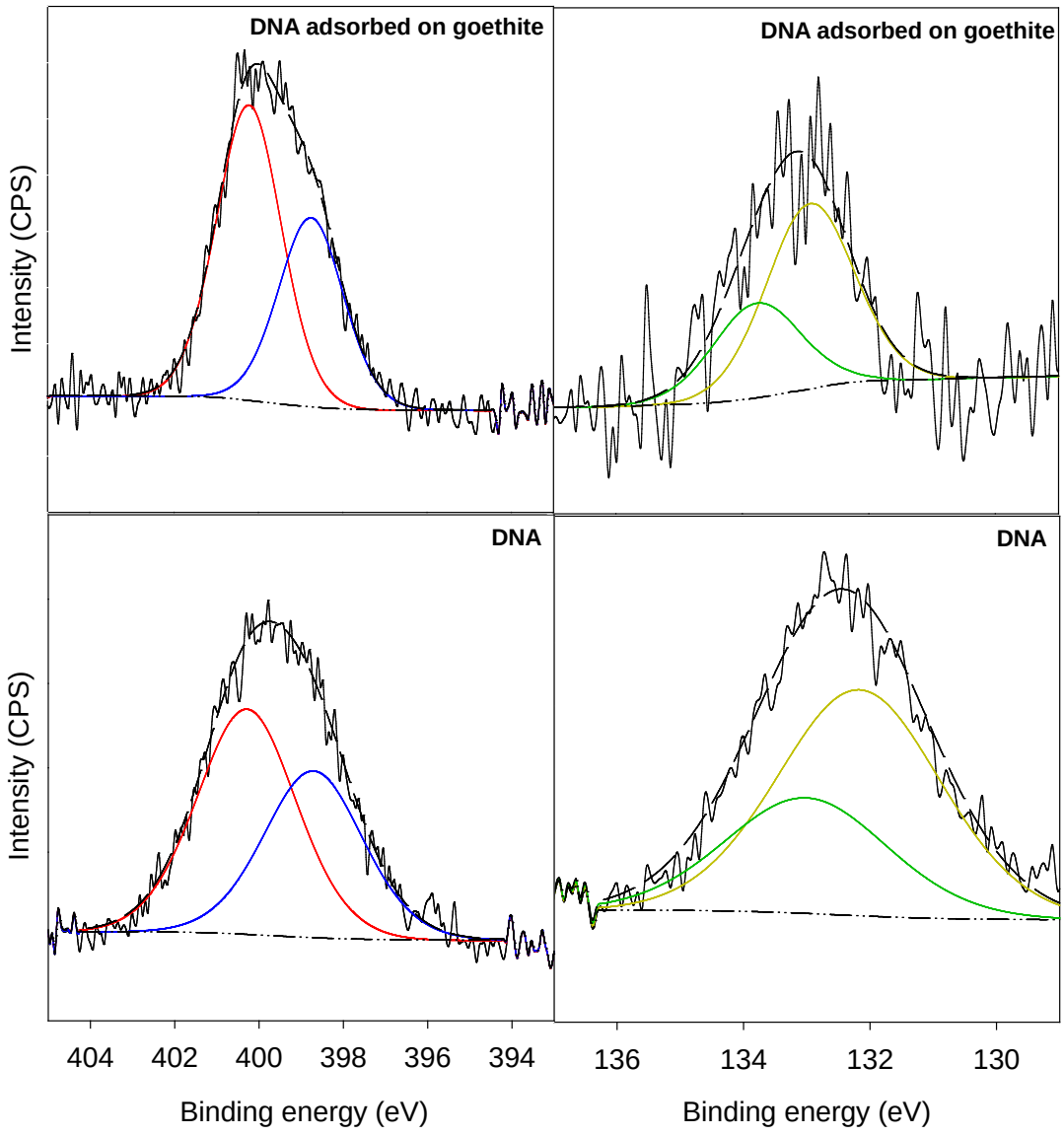

Figure 6. FTIR spectra of DNA in solution (top) and adsorbed at different DNA concentrations (low to high; top to bottom) from 1315-950 cm^{-1}. Blue (1068 cm^{-1}) and orange (1010 cm^{-1}) dotted lines denote peak positions of observed Fe-O-P modes.

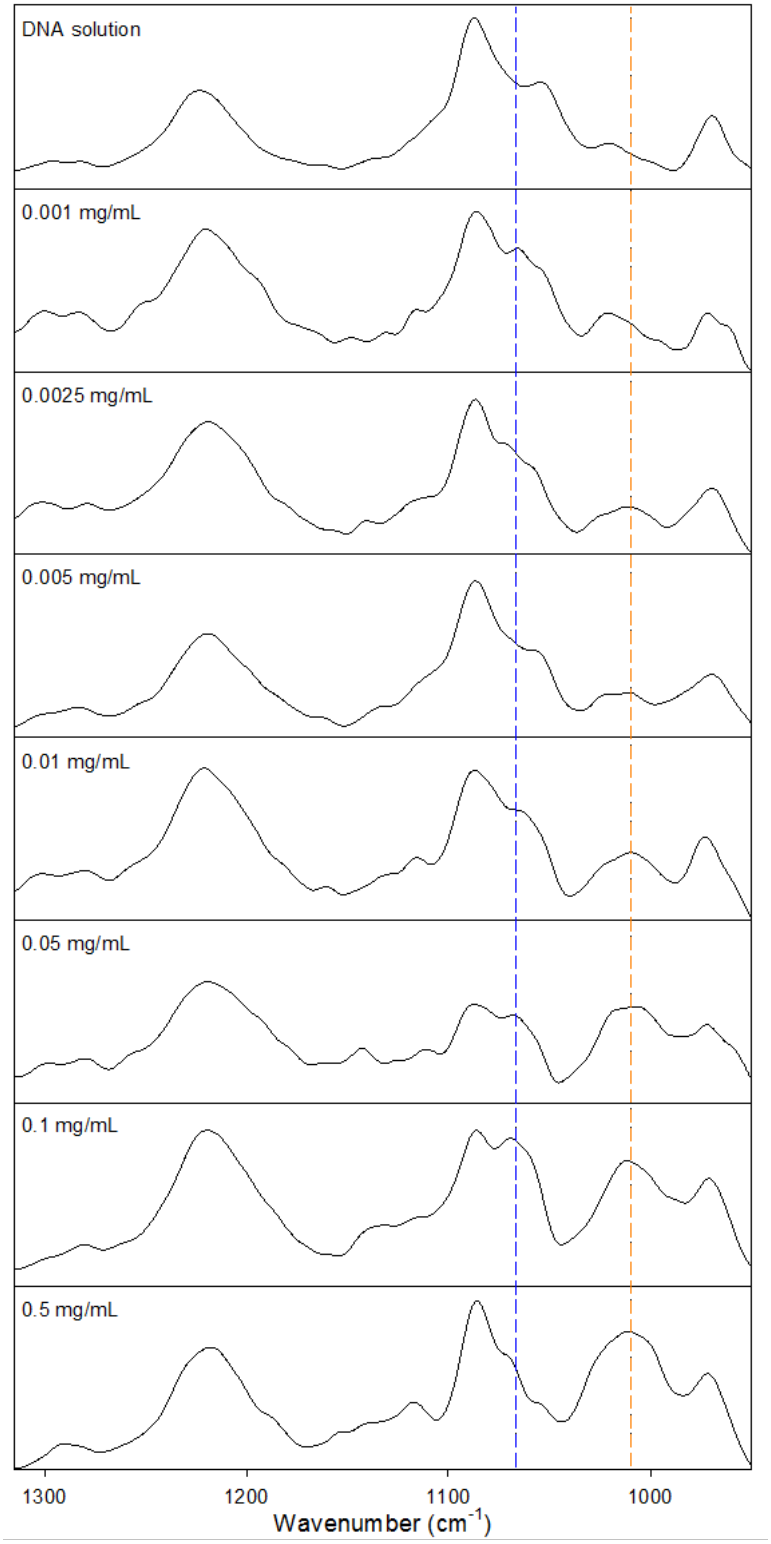

REFERENCES

(1) Nielsen, K.M.; Calamai, L.; Pietramellara, G. Stabilization of Extracellular DNA and Proteins by Transient Binding to Various Soil Components. In *Nucleic Acids and Proteins in Soil*; Nannipieri, P.; Smalla, K., Eds.; Springer-Verlag: Heidelberg, 2006; pp 141-153.

(2) Yu, W. H.; Li, N.; Tong, D. S.; Zhou, C. H.; Lin, C. X.; Xu, C. Y. Adsorption of proteins and nucleic acids on clay minerals and their interactions: A review *Appl. Clay Sci.* **2013,** *80-81,* 443-452.

(3) Pietramellara, G.; Ascher, J.; Borgogni, F.; Ceccherini, M. T.; Guerri, G.; Nannipieri, P. Extracellular DNA in soil and sediment: fate and ecological relevance *Biol. Fertil. Soils* **2009,** *45,* 219-235.

(4) Cai, P.; Huang, Q.; Zhang, X. Interactions of DNA with Clay Minerals and Soil Colloidal Particles and Protection against Degradation by DNase *Environ. Sci. Technol.* **2006,** *40,* 2921-2926.

(5) Paget, E.; Monrozier, L. J.; Simonet, P. Adsorption of DNA on clay minerals: protection against DNaseI and influence on gene transfer *FEMS Microbiol. Lett.* **1992,** *97,* 31-39.

(6) Lorenz, M. G.; Wackernagel, W. Adsorption of DNA to sand and variable degradation rates of adsorbed DNA *Appl. Environ. Microbiol.* **1987,** *53,* 2948-2952.

(7) Aardema, B. W.; Lorenz, M.G.; Krumbein, W. E. Protection of sediment-adsorbed transforming DNA against enzymatic inactivation *Appl. Environ. Microbiol.* **1983,** *46,* 417-420.

(8) Cai, P.; Huang, Q.; Lu, Y.; Chen, W.; Jiang, D.; Liang, W. Amplification of plasmid DNA bound on soil colloidal particles and clay minerals by the polymerase chain reaction *J. Environ. Sci.* **2007,** *19,* 1326-1329.

(9) Demanèche, S.; Jocteur-Monrozier, L.; Quiquampoix, H.; Simonet, P. Evaluation of biological and physical protection against nuclease degradation of clay-bound plasmid DNA. *Appl. Environ. Microbiol.* **2001,** *67,* 293-299

(10) Pietramellara, G.; Dal Canto, L.; Vettori, C.; Gallori, E.; Nannipieri, P. Effects of air-drying and wetting cycles on the transforming ability of DNA bound on clay minerals *Soil Biol. Biochem.* **1997,** *29,* 55-61

(11) Poté, J.; Rosselli, W.; Wigger, A.; Wildi, W. Release and leaching of plant DNA in unsaturated soil column *Ecotoxicol. Environ. Saf.* **2007,** *68,* 293-298.

(12) Poté, J.; Ceccherini, M. T.; Van, V. T.; Roselli, W.; Wildi, W.; Simonet, P.; Vogel, T. M. Fate and transport of antibiotic resistance genes in saturated soil columns *Eur. J. Soil Biol.* **2003,** *39,* 65-71.

(13) Cai, P.; Huang, Q.; Zhang, X. Microcalorimetric studies of the effects of $MgCl_2$ concentrations and pH on the adsorption of DNA on montmorillonite, kaolinite and goethite *Appl. Clay Sci.* **2006,** *32,* 147-152.

(14) Saeki, K.; Sakai, M.; Wada, S. DNA adsorption on synthetic and natural allophanes *Appl. Clay Sci.* **2010,** *50,* 493-497.

(15) Cai, P.; Huang, Q.; Zhu, J.; Jiang, D.; Zhou, X.; Rong, X.; Liang, W. Effects of low-molecular-weight organic ligands and phosphate on DNA adsorption by soil colloids and minerals *Colloids Surf., B* **2007,** *54,* 53-59.

(16) Saeki, K.; Kunito, T. Adsorptions of DNA molecules by soils and variable-charged soil constituents *Curr. Res. Technol. Educ. Top. Appl. Microbiol. Microb. Biotechnol.* **2010,** *1,* 188-195.
(17) Parikh, S. J.; Mukome, F. N. D.; Zhang, X. ATR-FTIR Spectroscopic Evidence for Biomolecular Phosphorus and Carboxyl Groups Facilitating Bacterial Adhesion to Iron Oxides *Colloids Surf., B* **2014,** *119,* 38-46.
(18) Mateo-Martí, E.; Briones, C.; Rogero, C.; Gomez-Navarro, C.; Methivier, C.; Pradier, C. M.; Martín-Gago, J. A. Nucleic acid interactions with pyrite surfaces *Chem. Phys.* **2008,** *352,* 11-18.
(19) Perderiset, M.; Baillif, P.; Jaurand, M. C. Chemical Analysis and Photoelectron Spectroscopy of the Adsorption of Macromolecules on the Surface of Attapulgite. *J. Coll. Interf. Sci.* **1988,** *121,* 381-391.
(20) Vanea, E.; Simon, V. XPS study of protein adsorption onto nanocrystalline aluminosilicate microparticles. **2011,** *257,* 2346-2352.
(21) Mundunkotuwa, I. A.; Minshid, A. A.; Grassian, V. H. ATR-FTIR spectroscopy as a tool to probe surface adsorption on nanoparticles at the liquid-solid interface in environmentally and biologically relevant media. *Analyst* **2014,** *139,* 870-881.
(22) Schmidt, M. P.; Martínez, C. E. Kinetic and Conformational Insights of Protein Adsorption onto Montmorillonite Revealed Using in Situ ATR-FTIR/2D-COS. *Langmuir* **2016,** *32,* 7719-7729.
(23) Bouhekka, A.; Bürgi, T. In situ ATR-IR spectroscopy study of adsorbed protein: Visible light denaturation of bovine serum albumin on TiO_2. *Appl. Surf. Sci.* **2012,** *261,* 369-374.
(24) Mudunkotuwa, I. A.; Grassian, V. H. Histidine adsorption on TiO_2 Nanoparticles: An Integrated Spectroscopic, Thermodynamic, and Molecular-Based Approach toward Understanding Nano-Bio Interactions *Langmuir* **2014,** *30,* 8751-8760.
(25) Sinden, R. R. *DNA Structure and Function*; Academic Press: San Diego, CA, 1994.
(26) Schwertmann, U.; Cornell, R.M. *Iron Oxides in the Laboratory: Preparation and Characterization;* VCH: Weinheim; New York, 1991.
(27) Beattie, D. A.; Chapelet, J. K.; Gräfe, M.; Skinner, W. M.; Smith E. In Situ ATR FTIR Studies of SO_4 Adsorption on Goethite in the Presence of Copper Ions *Environ. Sci. Technol.* **2008,** *42,* 9191-9196.
(28) Banyay, M.; Sarkar, M.; Gräslund. A. A library of IR bands of nucleic acids in solution *Biophys. Chem.* **2003,** *104,* 477-488.
(29) Calais, T.; Playe, B.; Ducéré, J. M.; Veyan, J. F.; Rupich, S.; Hemeryck, A.; Rouhani, M. D.; Rossi, C.; Chabal, Y. J.; Estève, A. Role of Alumina Coatings for Selective and Controlled Bonding of DNA on Technologically Relevant Oxide Surfaces *J. Phys. Chem. C* **2015,** *119,* 23527-23543.
(30) Gagnasso, M.; Boero, V.; Franchini, M. A.; Chorover, J. ATR-FTIR studies of phospholipid vesicle interactions with α-FeOOH and α-Fe_2O_3 surfaces *Colloids Surf., B* **2010,** *76,* 456-467.
(31) Parikh, S. J.; Chorover, J. ATR-FTIR Spectroscopy Reveals Bond Formation During Bacterial Adhesion to Iron Oxide *Langmuir* **2006,** *22,* 8492-8500.
(32) Lagergren, S. Zur theorie der sogenannten adsorption gelöster stoffe *K. Sven.*

Vetenkapsakad. Handl. **1898,** *24,* 1-39.
(33) Fredriksson, A.; Holmgren, A. An in situ ATR-FTIR study of the adsorption kinetics of xanthate on germanium *Colloids Surf., A* **2007,** *302,* 96-101.
(34) Atkins, P.; Paula, J.; Friedman, R. *Quanta, Matter and Change: A Molecular Approach to Physical Chemistry;* Oxford University Press: Oxford, 2009; Chapter 21.
(35) Petrovykh, D. Y; Kimura-Suda, H.; Tarlov, M. J.; Whitman, L. J. Quantitative Characterization of DNA Films by X-ray Photoelectron Spectroscopy *Langmuir* **2004,** *20,* 429-440.
(36) Melzak, K. A.; Sherwood, C. S.; Turner, R. F. B.; Haynes, C. A. Driving Forces for DNA Adsorption to Silica in Perchlorate Solutions *J. Coll. Interf. Sci.* **1996,** *181,* 635-644.
(37) Ogram A. V.; Mathot, M. L.; Harsh, J. B.; Boyle, J.; Pettigrew, C. A. Effects of DNA Polymer Length on Its Adsorption to Soils *Appl. Envioron. Microbiol.* **1994,** *60,* 393-396.
(38) Ratner, B. D.; Castner, D. G. Electron Spectroscopy for Chemical Analysis. In *Surface Analysis – The Principle Techniques* 2nd ed.*;* Vickerman, J. C.; Gilmore, I. S. Eds.; John Wiley & Sons Ltd.: Teddington, U.K., 2009.
(39) Mallet, M.; Barthélémy, K.; Ruby, C.; Naille, S. Investigation of phosphate adsorption onto ferrihydrite by X-ray Photoelectron Spectroscopy *J. Coll. Interf. Sci.* **2013,** *407,* 95-101.
(40) Vilar, M. R.; Bothelho do Rego, A. M.; Ferraria, A. M.; Jugnet, Y.; Noguès, C.; Peled, D.; Naaman, R. Interaction of Self-Assemble Monolayers of DNA with Electrons: HREELS and XPS Studies *J. Phys. Chem. B* **2008,** *112,* 6957-6964.
(41) Dinsmore, M. J.; Lee, J. S. Characteristic differences in the X-ray photoelectron spectrum between B-DNA and M-DNA monolayers on gold *J. Inorg. Biochem.* **2008,** *102,* 1599-1606.
(42) Majumder, S.; Priyadarshini, M.; Subudhi, U.; Chainy, G. B. N.; Varma, S. X-ray photoelectron spectroscopic investigations of modifications in plasmid DNA after interaction with Hg nanoparticles *Appl. Surf. Sci.* **2009,** *256,* 438-442.
(43) Pershina, A.G.; Sazonov, A. E.; Ogorodova, M. L. Investigation of the Interaction between DNA and Cobalt Ferrite Nanoparticles by FTIR Spectroscopy *Russ. J. Bioorg. Chem.* **2009,** *35,* 607-613.
(44) Lu, M.; Shan, Z.; Andrea, K.; MacDonald, B.; Beale, S.; Curry, D. E.; Wang, L.; Wang, S.; Oakes, K. D.; Bennett, C.; Wu, W.; Zhang, X. Chemisorption Mechanism of DNA on Mg/Fe Layered Double Hydroxide Nanoparticles: Insights into Engineering Effective SiRNA Delivery Sytems *Langmuir* **2016,** *32,* 2659-2667.
(45) Taillandier, E.; Liquier, J. Infrared Spectroscopy of DNA *Methods Enzymol.* **1992,** *211,* 307-335.
(46) Omoike, A.; Chorover, J.; Kwon, K. D.; Kubicki, J. D. Adhesion of Bacterial Exopolymers to α-FeOOH: Inner-Sphere Complexation of Phosphodiester Groups *Langmuir* **2004,** *20,* 11108-11114.
(47) Barja, B. C.; Tejedor-Tejedor, M. I.; Anderson, M. A. Complexation of Methylphosphonic Acid with the Surface of Goethite Particles in Aqueous

Solution *Langmuir* **1999,** *15,* 2316-2321.
(48) Ruttenberg, K. C.; Sulak, D. J. Sorption and desorption of dissolved organic phosphorusonto iron (oxyhydr)oxides in seawater *Geochim. Cosmochim. Acta* **2011,** *75,* 4095-4112.
(49) Nooney, M. G.; Murrell, T. S.; Corneille, J. S.; Rusert, E. I.; Hossner, L. R.; Goodman, D. W. A spectroscopic investigation of phosphate adsorption onto iron oxides *J. Vac. Sci. Technol. A* **1996,** *14,* 1357-1361.
(50) Niemeyer, J.; Gessler, F. Determination of free DNA in soils *J. Plant Nutri. Soil Sci.* **2002,** *165,* 121-124.
(51) Siuda, W.; Güde, H. Determination of dissolved deoxyribonucleic acid concentration in lake water *Aquat. Microb. Ecol.* **1996,** *11,* 193-202.
(52) Cai, P.; Zhu, J.; Huang, Q.; Fang, L.; Liang, W.; Chen, W. Role of bacteria in the adsorption and binding of DNA on soil colloids and minerals *Colloids Surf., B* **2009,** *69,* 26-30.
(53) Goldberg, S. Soil Colloidal Behavior. In *Handbook of Soil Science;* Sumner, M.E., Ed.; CRC Press: Boca Raton, London, New York, Washington, DC, 2000; Chapter 6, pp B-195 to B-240.
(54) Rousseau, M.; Di Pietro, L.; Angulo-Jaramillo, R.; Tessier, D.; Cabibel, B. Preferential Transport of Soil Colloidal Particles: Physicochemical Effects on Particle Mobilization. *Vadose Zone J.* **2004,** *3,* 247-261.
(55) Kaiser, K.; Guggenberger, G. The role of DOM sorption to mineral surfaces in the preservation of organic matter in soils. *Org. Geochem.* **2000,** *31,* 711-725.
(56) Cotrufo, M. F.; Wallenstein, M. D.; Boot, C. M.; Denef, K.; Paul, E. The Microbial Efficiency-Matrix Stabilization (MEMS) framework integrates plant litter decomposition with soil organic matter stabilization: do labile plant inputs form stable soil organic matter? *Global Change Biol.* **2013,** *19,* 988-995.
(57) Desai, N. A.; Shankar, V.; Single-strand-specific nucleases *FEMS Microbiol. Rev.* **2003,** *26,* 457-491.
(58) Lorenz, M. G.; Wackernagel, W. Bacterial Gene Transfer by Natural Genetic Transformation in the Environment *Microbiol. Rev.* **1994,** *58,* 563-602.

CHAPTER FOUR

Supramolecular association impacts biomolecule adsorption onto goethite

Introduction

Stabilization of input organic matter (OM) through various mechanisms is a primary reason for both the magnitude of the soil organic carbon pool (≈2370-2450 Pg C in top 2 m) and its potential to act as a carbon sink.[1-4] Retention of OM by mineral surfaces in organo-mineral associations is recognized as a prevalent form of soil organic matter (SOM) stabilization, with molecular-level interaction between adsorbed organic matter and mineral surfaces protecting against degradation.[5-9] Formation of organo-mineral associations is initiated by adsorption of dissolved organic matter (DOM), a mixture of organic molecules in soil solution derived from plant and microbial sources, onto mineral surfaces.[7,8] DOM does not adsorb indiscriminately, however, with large biomolecules and microbial residues believed to be selectively retained by mineral surfaces.[7,10] Initial adsorption of biomolecules onto mineral surfaces has been hypothesized to act as a base for subsequent retention of organic matter at mineral surfaces by biomolecule-biomolecule interaction, resulting in the patchy, multilayered architecture of mineral associated SOM observed in soils.[7] These concepts highlight the impact of both biomolecule-mineral and biomolecule-biomolecule interactions on the stabilization of organic carbon in soils.

Theoretical and experimental studies probing the adsorption of biomolecules onto mineral surfaces in model systems suggest strong adsorption occurs across a range of conditions.[11-19] Interfacial contact may result in conformational

rearrangement of the adsorbate and bond formation between adsorbed biomolecules and the mineral substrate.[13,15,19,20] Surface adsorption has been demonstrated to release large amounts of free energy and thus favor interfacial assembly of biomolecules at mineral surfaces, reinforcing the concept of preferential adsorption of biomolecules from DOM in soil solution.[10,21] While previous experiments highlight a favorable adsorptive interaction, the inherent complexity of DOM favors spontaneous interaction and assembly of constituent molecules in solution before contact with a mineral surface.[22] This interaction leads to formation of supramolecular assemblies of biomolecules (e.g. proteins, lipids, lignin, nucleic acids) in soil solution through hydrogen bonds, hydrophobic forces or electrostatic interactions.[22] Upon engagement in supramolecular assembly, formation of colloids may induce changes to biomolecular properties, with size, morphology, charge and function different from individual constituent biomolecules.[23-26] Despite this current understanding, work focused on biomolecule interaction in solution and subsequent impact on interfacial behavior at mineral surfaces is scarce.

Here we investigate the formation of supramolecular associations in solution and their impact on the biomolecule/mineral interfacial environment in mixed systems. A model nucleic acid (deoxyribonucleic acid (DNA)) is used to investigate how supramolecular complexation with a model protein (bovine serum albumin (BSA)) influences the interfacial behavior of DNA at a common mineral surface (goethite). A model protein and nucleic acid were selected for these experiments as they account for a large portion of microbial biomass, with nucleic acids and proteins representing ≈23% and ≈55%, respectively, of dried bacterial biomass.[27] Nucleic acids and proteins

are both present within natural DOM fractions (≈μg/L and mg/L levels previously reported, respectively), indicating they may serve as environmentally relevant models.[28,29] While the model protein used (BSA) is not found in soil, nor does BSA individually represent the diverse nature of soil proteins, it possesses traits similar to some soil proteins. With a molecular mass of around 66 kDa, BSA falls within the range of masses observed for proteins extracted from soils (≈14-98 kDa in DOM and ≈6-181 kDa in whole soil) and has a globular structure.[30,31] Furthermore, the isoelectric point (≈4.7) of BSA is within the range of values previously observed for proteins extracted from a field groundwater reactor (≈4-8).[32] Interaction between DNA and a serum protein, BSA, would also represent a nonspecific binding process, which occur readily through physicochemical interactions (i.e. hydrogen bonding, electrostatic interactions, hydrophobic interactions) without sequence specificity, as would be expected between proteins and DOM.[33-36]

In these studies, a series of DNA/BSA complexes is synthesized with a fixed DNA concentration and varying BSA concentrations, yielding complexes with a range of BSA:DNA ratios. Equilibrium binding behavior between DNA and BSA is described with circular dichroism (CD) spectroscopy. Charge and size of the DNA/BSA associations are characterized by dynamic light scattering (DLS) measurements. Surface adsorption of DNA/BSA complexes onto goethite is probed using *in situ* attenuated total reflectance Fourier transform infrared (ATR-FTIR) spectroscopy, a technique which monitors surface adsorption under environmentally relevant conditions (i.e. in solution, in real time, non-destructive analysis), providing direct molecular-scale characterization of the DNA/BSA complex-goethite aqueous

interface.[37] Through application of solution phase and surface characterization of model DNA/BSA complexes, a novel viewpoint is developed on the indirect control of supramolecular association on the interfacial behavior of biomolecules at mineral surfaces.

Materials and Methods

Materials. Double-stranded herring testes DNA (B-form, Type XIV, Sigma Aldrich prod. No. D6898) was used in all experiments. This specific type of DNA was used because it was used in previous adsorption experiments with goethite.[13] While herring testes DNA is not found in soil and is possibly not representative of soil DNA base pair composition, DNA base pair composition was determined to have little influence on previous studies probing DNA adsorption onto soil minerals.[38] Prior to use, DNA was ultrasonically sheared to a shorter length (≈ 400 bp) and more uniform size distribution.[13] BSA used in experiments (Sigma Aldrich prod. No. B4287, M.W. ≈66.5 kDa, pI≈4.7) was used as received without further purification. All solutions were made with deionized water (18.2 MΩ resistance). In all experiments, a background electrolyte of 5 mM KCl was added to approximate the low ionic strength of soil solutions.

Goethite used in adsorption experiments was synthesized by the method of Schwertmann and Cornell.[39] Details are included in the supplementary information. Identity and purity of the synthesized goethite was verified with FTIR and the surface area was determined to be 56.6 m^2/g by N_2 adsorption. SEM determined particles to be needle-like with width around 50 nm and length ranging from a few hundred

nanometers to a few micrometers. Additional details about goethite synthesis and preparation and purity of DNA are included in the supplementary information.

Synthesis of DNA/BSA complexes. DNA/BSA complexes were synthesized by the addition of 0.2 mg/mL DNA in a 5 mM KCl background solution at pH=5.0 to an equal volume of BSA ranging in concentration from 0.1-1.0 mg/mL in the same background solution under rapid stirring. After initial combination of solutions, stirring was stopped and complexes were equilibrated for at least 30 minutes. Complexes were then adjusted to pH=5.0 using 5 mM HCl, after which complexes were equilibrated an additional 30 minutes before solution characterization or use in adsorption experiments. The amount of time allowed for DNA and BSA equilibration, totaling at least 1 hour, is assumed to be enough time for equilibration based on times used from previous studies probing protein-nucleic acid binding, which demonstrate rapid interaction.[40,41] This process resulted in a series of DNA/BSA complexes with a fixed DNA concentration of 0.1 mg/mL and ranging from 0.05-0.5 mg/mL BSA.

Circular dichroism (CD) spectroscopic analysis of DNA/BSA complexes. CD spectra were acquired on samples initially ranging from 0-0.5 mg/mL BSA and 0.1 mg/mL DNA at 0.05 mg/mL BSA increments, for a total of 11 points. Immediately prior to collection of CD spectra, samples were diluted to a DNA concentration of 0.04 mg/mL to avoid saturation of the dynode in the detector, which may lead to irregularities in the data. Experimental binding curves were collected in triplicate for all data points.

CD spectra were analyzed to determine DNA-BSA binding behavior in a manner described previously for probing DNA-protein interaction.[42,43] When

interaction occurs between DNA and a ligand, the underlying optical activity of the DNA helix may be changed, altering the molar extinction coefficient (Δε). The response of Δε to increasing ligand concentration may yield information about DNA-ligand stoichiometry and strength of interaction. For these studies, change in Δε (ΔΔε) at 280 nm with incremental addition of BSA was plotted against BSA:DNA molar ratio, yielding a DNA/BSA binding curve across a range of BSA:DNA stoichiometries. A molar mass of 2.6×10^5 Da was assumed for DNA based on 400 bp length and an average mass of 650 g/mol per base pair. Spectrometer manufacturer, model and collection parameters may be found in the supplementary information.

Light scattering measurements. For light scattering measurements, a refractive index of 1.500 was assumed for DNA and DNA/BSA complexes with a refractive index of 1.33 and viscosity of 0.954 cP used for water. Electrophoretic mobility measurements represent an average of three measurements on each sample. Prior to synthesizing complexes for light scattering measurements, DNA and BSA solutions were passed through 0.2 (BSA) and 0.45 μm (DNA) polyethersulfone syringe filters to remove dust or suspended particulates which could interfere with light scattering from samples. Complexes synthesized for other analyses (CD, FTIR) were not filtered, as these methodologies are not highly sensitive to low levels of particulates. Instrument manufacturer, model, parameters and setup can be found in the supplementary information.

ATR-FTIR experiments. Solution spectra of BSA and DNA were collected at concentrations of 10 and 5 mg/mL, respectively, in a background solution of 5 mM KCl at pH=5.0, chosen to approximate soil solution conditions (i.e. acidic with low

ionic strength). Solution spectra of BSA were collected to eliminate contribution of BSA adsorbed on the diamond internal reflective element (IRE) using a previously described approach.[42] Further details about BSA adlayer subtraction are included in the supplementary information. No correction was necessary for DNA, which did not adsorb to the IRE under our experimental conditions. Goethite films used in adsorption experiments were made using a previously described approach (see supplementary information).[45] After creating a goethite film, background solution was passed over the film at a flow rate around 2 mL/min. until no detectable changes to the FTIR spectrum were observed (1.5-2 hours). At this point, a background spectrum of the electrolyte solution was collected. The DNA or DNA/BSA complex solution was then introduced. DNA was used at a fixed concentration of 0.1 mg/mL in adsorption experiments, with BSA concentrations of 0.1, 0.2, 0.3, 0.4 and 0.5 mg/mL used. Adsorption experiments were run in triplicate for each experimental DNA/BSA ratio and DNA. It should be noted that at the concentrations of biomolecules used in our adsorption experiments, solution contributions have been previously determined to yield no significant contribution to spectra.[15] Instrument manufacturer, model, configuration and data processing procedures are included in the supplementary information.

Results and Discussion

Formation and Physicochemical Characteristics of Supramolecular Complexes in Solution. To probe the equilibrium binding behavior between DNA and BSA, circular dichroism (CD) studies were performed with synthesized complexes. CD results suggest that BSA and DNA interact in solution under experimental conditions (5 mM

KCl at pH=5.0), as an increase in molar extinction coefficient with increasing amounts of BSA is observed (**Figure 4.1**). This corresponds with a previous study probing DNA-BSA interaction in solution, which demonstrated that it is possible to form nonspecific complexes between BSA and a model double stranded oligonucleotide at pH = 3.0.[46] The steady increase in $\Delta\Delta\varepsilon$ of DNA at low BSA:DNA ratios (<15.1, [BSA] = 0.4 mg/mL) is potentially the result of strong interaction between BSA and DNA. Similar binding behavior between the protein C.AhdI and DNA was interpreted as a strong, stoichiometric binding process between DNA and C.AhdI.[43] Observed DNA-BSA binding behavior qualitatively follows a sigmoidal Hill-type binding model, yielding a better fit than the other tested model, the Langmuir equation, suggesting interaction between bound BSA molecules may influence binding (**Figure A4.1 and Table A4.1).** Some degree of cooperativity is likely based upon the upward inflection of the binding curve at lower BSA:DNA ratios and a Hill coefficient greater than 1 (n=2.71) (**Table A4.1**).[47,48] The Hill model fit shown in **Figure 4.1** yields a K_d value of 2.11 μM, while this value is not quantitatively meaningful given the proximity to total experimental BSA concentrations (0.75-7.5 μM), similarity between predicted K_d and experimental BSA concentrations provides further evidence of tight binding between BSA and DNA.[48] Over the range of BSA:DNA ratios used, $\Delta\Delta\varepsilon$ plateaus, indicating saturation of BSA binding sites on DNA is reached. A maximum $\Delta\Delta\varepsilon$ value is reached at a BSA:DNA ratio of 15.1, suggesting that BSA added beyond this ratio may not bind to DNA directly.

Electrophoretic mobility measurements were made on BSA, DNA and synthesized complexes to determine the influence of binding on charge characteristics

of DNA/BSA complexes. Electrophoretic mobility results suggest BSA:DNA ratio has an impact on the charge characteristics of synthesized DNA/BSA complexes (**Figure 4.1**). DNA itself has a electrophoretic mobility of -3.10 x 10^{-8} m^2/Vs, which would be expected at the experimental pH value of 5.0, which is above, or on the higher end, of anticipated pI values (≈4.5) for DNA. BSA has a electrophoretic mobility of -0.17 x 10^{-8} m^2/Vs at pH=5.0, yielding a less negative value than DNA, but indicative of an overall negative charge on BSA. This reflects the proximity of our experimental conditions to the pI of BSA (≈4.7) relative to that of DNA. As BSA:DNA ratio increases, a decreasing trend in electrophoretic mobility of the synthesized complexes is observed. BSA addition across experimental BSA:DNA ratios increased the electrophoretic mobility of DNA/BSA complexes up to-1.88 x 10^{-8} m^2/Vs, a change of 1.22 x 10^{-8} m^2/Vs compared to DNA alone. This shift in electrophoretic mobility is interpreted as a reduction in negative charge associated with DNA/BSA complexes as more BSA binds to DNA.

Light scattering characteristics of DNA, BSA and synthesized complexes was used to identify changes in size of DNA/BSA complexes and intermolecular interactions between synthesized complexes. Light scattering results for BSA, DNA and DNA/BSA complexes can be seen in **Figure 4.2**. The relaxation time distribution of BSA features one primary relaxation mode, a peak at 27.7 μs. This peak likely arises from translational diffusion of BSA molecules in solution and is in agreement with previous studies of BSA, which demonstrate unimodal light scattering distributions.[49,50] A weak peak at around 521 μs is also present, suggesting sample filtration may not have entirely removed all of the large BSA aggregates in the sample

or BSA aggregated slightly after filtration.[50]

The relaxation time distribution for DNA shows a bimodal distribution, with two primary peaks at 66.8 and 450 μs observed (**Figure 4.2**). These peaks correspond with two distinct relaxation modes, designated as fast and slow relaxation modes, respectively. Presence of a fast relaxation mode is attributable to a combination of intramolecular relaxation modes and translational diffusion of DNA, which are exceptionally challenging to separate experimentally.[51-53] Several concepts have been proposed to explain the slow mode of polyelectrolytes, such as DNA, in light scattering studies. Synchronized movement of DNA molecules locked into concerted movement by repulsive, electrostatic intermolecular interactions has been a proposed cause of the slow mode of DNA.[54-56] It has also been proposed that the slow relaxation mode of DNA may be the result of the diffusion of individual DNA molecules within a cage of nearby DNA molecules, requiring specific DNA orientation to diffuse due to electrostatic repulsion with the cage-like DNA structure.[57] This requisite specificity of DNA movement, likely in line with the long axis of a DNA strand, results in a slower relaxation rate.[57] Both of these theories, while rather different in description of the phenomenon of the slow mode, suggest intermolecular DNA-DNA interactions play a critical role in its appearance. Furthermore, electrostatic forces arising from deprotonation of backbone phosphate groups seem to be essential to the development of intermolecular repulsion. Given the low ionic strength (5 mM KCl) and the cation used in experiments (K^+), DNA-DNA repulsion would be expected, as these conditions would likely favor poor shielding of charges between DNA strands. While it may be advantageous for data interpretation to present hydrodynamic radii of BSA,

DNA and DNA/BSA complexes, it has been previously suggested that determination of DNA hydrodynamic radius under conditions similar to ours may be obscured.[54,58] This is due to intermolecular repulsion between DNA helices in solution and the subsequent influence on translational diffusion, which is used to calculate hydrodynamic radius.

Upon titration of different starting concentrations of BSA with a fixed amount of DNA, changes to the DNA light scattering distribution are observed. At low BSA:DNA ratios (≤3.9), increasing amount of BSA corresponds with a decrease in the intensity of the DNA slow mode peak. A marked decrease in the slow relaxation peak intensity with protein addition to DNA was observed previously in a study investigating DNA-lysozyme interaction under similarly low ionic strength conditions (3 mM NaCl).[54] This observation was attributed to reduction of intermolecular repulsion between DNA helices by the addition of lysozyme.[54] The proposed mechanism for alleviating DNA-DNA repulsion is through a screening of electrostatic repulsion by charge neutralization via lysozyme association with DNA.[54] This interpretation would correspond with electrophoretic mobility results, which highlight a decrease of negative charge on DNA/BSA complexes with increasing BSA concentration. A lower negative charge could, in turn, reduce electrostatic repulsion between DNA strands within DNA/BSA complexes. While BSA does not possess a net positive charge under experimental conditions, screening of negative charges between DNA strands could result from local interaction between DNA backbone phosphodiester groups and positively charged side chain groups of BSA (e.g. lysine, arginine). Local binding of positively charged side chain groups to DNA is believed to

be one of the primary mechanisms driving nonspecific interaction (e.g. DNA-BSA) between proteins and nucleic acids.[34,59] BSA has been shown to have numerous exposed lysine side chain groups that could serve as interaction sites with the backbone phosphodiester groups of DNA.[60] In addition, BSA has long been known to possess a heterogeneous surface charge distribution at pH=5.0 despite its net negative charge, with some regions possessing a positive charge and others negative.[61] This charge asymmetry has been demonstrated to influence BSA association with a series of anionic polymers, where positive charge patches on BSA were demonstrated to interact with polyelectrolyte species even though net charges suggest repulsion would occur.[62] Interaction between DNA and regional positive charge patches on BSA could thus be driving binding between the negatively charged biomolecules. It is also possible that conformational rearrangement of BSA occurs upon binding to DNA, which may include involvement of side chain groups that are buried in native BSA. In addition to electrostatic considerations for reduced repulsion between DNA/BSA complexes, previous work on DNA-BSA complexation suggests hydrophobic interactions may also enhance attraction between DNA/BSA aggregates, reducing net repulsion through attractive forces.[44]

In addition to a decrease of intensity of the slow relaxation mode with increasing BSA:DNA ratio up to 3.9, both the slow and fast modes shift to higher relaxation times, corresponding with a decrease of associated diffusion coefficients (**Figure 4.2**). This change is attributed to increased size of DNA/BSA complexes with increasing BSA addition, which would effectively reduce the diffusion coefficient as described by the inverse size-diffusion relationship defined by the Stokes-Einstein

equation.[51,63] This interpretation is based on assignment of the fast (coupled with internal relaxation modes) and slow relaxation modes to diffusion of DNA. Conceptually, incorporation of bound BSA would lower translational motion associated with both modes, hindered by intermolecular repulsion or otherwise. Persistence of the slow relaxation mode coupled with the shift of the slow mode peak to higher relaxation times at low BSA:DNA ratios suggests that repulsive forces between DNA strands are appreciable at BSA:DNA ratios ≤3.9.

At BSA:DNA ratios exceeding 3.9, the slow mode of DNA disappears, suggesting repulsive interaction between DNA strands is diminished. Comparison of light scattering results with the binding curve from CD spectroscopy (**Figure 4.1**) shows that this point corresponds with the steep, upward inflection of the DNA-BSA binding curve after an initial lag. Together, these points demonstrate the impact of increasing association of BSA with DNA on the forces between DNA/BSA complexes in solution. In addition to the apparent decrease in repulsion amongst DNA/BSA complexes, light scattering distributions of complexes formed with BSA:DNA ratios >3.9 show a decrease in diffusion coefficient of the fast mode with increasing BSA (**Figure 4.2**). Given the binding characteristics of BSA and DNA and results from electrophoretic mobility measurements, it is likely that the size of supramolecular DNA/BSA complexes continues to grow beyond a BSA:DNA ratio of 3.9. In accordance with this observed binding behavior, the diffusion coefficient of fast mode of complexes (partially attributable to translational movement) decreases with added BSA, reflecting an increased size of DNA/BSA associations. Interestingly, light scattering of DNA/BSA complexes synthesized beyond saturation on the DNA-BSA

binding curve do not appear to show the translational diffusion mode of free BSA.

Adsorption of DNA/BSA Supramolecular Complexes onto Goethite. *In-situ* ATR-FTIR spectroscopic experiments were applied to monitor the adsorption of DNA/BSA complexes onto goethite from solution in real time. Normalized FTIR spectra of BSA and DNA in solution, adsorbed on goethite at equilibrium and adsorbed on goethite at equilibrium as DNA/BSA complexes can be seen in **Figure 4.3**. The peak at 1652 cm^{-1} is assigned to the amide I band of BSA, which primarily represents vibrations from backbone ν C=O modes.[64] The amide II band, located at 1547 cm^{-1}, represents a combination band from the backbone in plane δ N-H and ν C-N modes.[64] Peaks at 1450 and 1400 cm^{-1} are tentatively attributed to side chain δ C-H and ν_s COO^- modes, respectively.[64] FTIR spectra of BSA in solution and adsorbed on goethite also show the amide III band from 1350-1200 cm^{-1}, attributable to the in-phase combination of backbone δ N-H and ν C-N modes.[64] There are no apparent changes (e.g. appearance of peaks, shifting of the amide I band, shifting of the amide I/amide II ratio) to the FTIR spectrum of adsorbed BSA from 1700-1200 cm^{-1} compared to BSA in solution. While this qualitative assessment of adsorbed BSA does not suggest there are any major structural or conformational changes to BSA upon adsorption to goethite, a more comprehensive analysis of adsorbed BSA, such as deconvolution of the amide I or III band, may reveal unfolding of BSA on goethite, as one may expect with a soft-globular protein such as BSA.[15,65,66] Previous studies of protein adsorption on the hematite (Fe-oxide) mineral surface suggests that soft, globular proteins, like BSA, adsorb with accompanying conformational changes.[67] Furthermore, electrostatic

interactions play a critical role in adsorption, with both protein-hematite and protein-protein electrostatic interactions influencing adsorption. BSA spectra are presented to show general features of FTIR spectra of BSA and how they can be distinguished from DNA within DNA/BSA complexes.

FTIR spectra of DNA in solution and adsorbed on goethite show key differences that clarify the adsorption mechanism (**Figure 4.3**).[13] Solution DNA and DNA adsorbed on goethite show three peaks from ν C=O guanine, ν C=O thymine and ν C=N/ν C=C of nucleobase rings. These peaks appear at 1714, 1664 and 1605 cm^{-1} and 1711, 1661 and 1605 cm^{-1} in solution and adsorbed DNA, respectively.[68] DNA also shows a peak associated with δ C-H modes at 1489 and 1485 cm^{-1} for solution and adsorbed species, respectively.[69] Structurally important vibrational modes related to the DNA backbone can be observed at 1224 (ν_{as} PO_4^-), 1088 (ν_s PO_4^-), 1055 (backbone ν C-O), 1021 (furanose vibration) and 970 cm^{-1} (backbone ν C-C) in solution DNA. These peaks appear in the same position in the FTIR spectrum of adsorbed DNA, with the exception for the ν_{as} PO_4^- peak. Upon adsorption, a shift in the ν_{as} PO_4^- peak to 1219 cm^{-1} occurs, suggesting interaction of backbone phosphodiester groups with goethite plays a role in DNA adsorption.[70] This interpretation is reinforced by the appearance of a strong peak at 1010 cm^{-1} and a shoulder at 1068 cm^{-1}, both of which are indicative of Fe-O-P bond stretching, suggesting inner-sphere complexation occurs between goethite and DNA.[13, 71-73] This conclusion was supported by X-ray photoelectron spectroscopy (XPS), which demonstrated an increase of P 2p binding energy upon DNA adsorption to goethite.[13]

Normalized spectra of DNA/BSA complexes adsorbed on goethite (**Figure 4.3**

and **Figure A4.2**) show features related to both DNA and BSA. At all BSA:DNA ratios studied BSA amide I and II peaks are apparent, with the weaker amide III and side chain δ C-H and ν_s COO^- modes becoming relatively more prominent at higher BSA:DNA ratios, which aligns with complexes becoming more enriched in BSA. DNA related peaks discernible in spectra are primarily attributable to backbone groups, with the ν_{as} PO_4^-, ν_s PO_4^- and backbone ν C-C peaks most apparent. Nucleobase vibrations are mostly obscured by the amide I peak of BSA, but the ν C=O guanine peak at around 1714 cm^{-1} represents a discreet peak at the lowest experimental BSA:DNA ratio of 3.9 and a shoulder to the amide I peak at BSA:DNA ratios >3.9. In addition to recognizable vibrations from the DNA helix (i.e. nucleobase and backbone vibrations), the ν Fe-O-P modes at 1068 and 1010 cm^{-1} are clearly visible in DNA/BSA complexes adsorbed on goethite. Together, these results show that BSA and DNA are both adsorbed at an aqueous goethite interface under experimental conditions.

Absolute intensities of peaks, with peak height proportional to the amount of vibration associated with either DNA or BSA, are used to quantitatively assess the impact of varying BSA:DNA ratio in solution on surface speciation.[36] The amide II peak is selected as the indicator of BSA adsorption due to its demonstrated proportionality with adsorbed protein.[74,75] The amide II peak also does not directly overlap with any major peaks in DNA, minimizing any interference of peak intensity from DNA within DNA/BSA complexes. For adsorbed DNA, the ν C-C peak height at 970 cm^{-1} is used as a metric for DNA adsorption, proportional to the amount of DNA adsorbed. This feature does not change in position or relative intensity upon

interaction of DNA with serum protein or upon surface adsorption onto goethite, where use of this peak for quantification of adsorbed DNA was corroborated by XPS experiments.[13,76] This peak also does not overlap with features of BSA in solution or adsorbed on goethite, further validating the utility of this peak to measure DNA adsorbed within DNA/BSA complexes. ν Fe-O-P peak height, given its connection to inner-sphere coordination of DNA to goethite and the lack of BSA related peaks in this region, serves as an analogue for direct binding of DNA within DNA/BSA complexes onto goethite, with peak height proportional to direct interaction between DNA backbone phosphodiester group and goethite The While the ν C-C and ν Fe-O-P peaks of adsorbed DNA are used here to generalize quantity of DNA adsorbed and direct coordination of DNA with goethite, respectively, the orientation of DNA itself and within DNA/BSA complexes on goethite is not probed through these modes.

FTIR spectra from adsorption experiments with two different BSA:DNA solution ratios (7.6 and 18.9) show increasing signals of distinct BSA and DNA related peaks with time (**Figure 4.4 and Figure A4.3**). Kinetic results do not appear to be influenced by diffusion within the goethite film in these experiments. Although pore size distributions within drop cast films was not characterized here, characteristics of diffusion limited adsorption, such as a square root time dependence or slow approach to equilibrium are not observed here. Moreover, our previous work with the adsorption of DNA on goethite using the same film deposition technique suggests that the adsorption of DNA, the constituent molecule with the single largest dimension (≈130 nm in length) used here, is surface controlled rather than diffusion limited.[13] The relative proportion of BSA and DNA adsorbed on goethite, however,

differs throughout adsorption between experimental ratios, as indicated by amide II/ ν C-C peak ratios with time (**Figure 4.5a**). BSA:DNA solution ratios ≤15.1 show a relatively uniform proportion of BSA and DNA as adsorption progresses with time. This suggests that the stoichiometry of adsorbed BSA and DNA remains stable throughout adsorption. At a BSA:DNA ratio of 18.9, however, there is a rapid decrease of the amide II/ ν C-C ratio within the first 15 minutes of adsorption. The initially higher amide II/ ν C-C ratio can be attributed to a greater proportion of BSA than DNA adsorbed, relative to times after 15 minutes of adsorption. Spectra show the presence of BSA amide I and II peaks early in the adsorption process while peaks related to DNA are barely visible. This trend is apparent in FTIR spectra from different adsorption time points from an experiment using a BSA:DNA ratio of 18.9 (**Figure 4.4**). This initial kinetic region up to 15 minutes is followed by a stable amide II/ ν C-C ratio for the duration of adsorption, suggesting that the relative stoichiometry of adsorbed material stabilizes after 15 minutes. Equilibrium amide II/ ν C-C ratios at BSA:DNA ≤ 15.1 exhibit a linear increase with incremental increase in BSA. This is in line with observed amide II/ ν C-C ratios throughout adsorption, which suggest no detectable discrimination toward BSA or DNA occurs at the interface. At BSA:DNA = 18.9, equilibrium amide II/ ν C-C ratio markedly increases above what would be expected on the basis of solution BSA:DNA ratios alone. At this BSA:DNA ratio, amide II/ ν C-C with time shows a higher proportion of BSA is adsorbed initially, relative to DNA. Amide II/ ν C-C at 99 minutes suggests this initial kinetic partitioning translates to a more BSA-rich interface at equilibrium as well. Differences in relative proportion of DNA and BSA adsorbed on goethite with time between

BSA:DNA ratios at and below 18.9 are attributed to the binding characteristics of DNA and BSA in solution. When BSA:DNA ratio in solution is 18.9, the binding curve suggests BSA is present in excess of binding saturation on DNA and is not bound strongly to DNA and, hence, is not as strongly associated with DNA as BSA bound to DNA at lower BSA:DNA ratios. It is possible that weakly associated BSA adsorbs quicker than DNA and BSA bound in larger DNA/BSA complexes, as proteins adsorb rapidly and irreversibly to mineral surfaces.[77] This situation contrasts with complexes formed at BSA:DNA ratios at or below binding saturation, in which tight binding between BSA and DNA favors complexation, rather than persistence of individual biomolecules in solution. Under these conditions, DNA and BSA adsorb in association and maintain a relatively uniform surface speciation throughout adsorption process.

The impact of BSA:DNA ratio in solution on the ν C-C peak at equilibrium shows that increasing the amount of BSA bound to DNA, up to a BSA:DNA ratio of 15.1, generally enhances DNA adsorption (**Figure 4.5b**). When no BSA is present, the ν C-C peak height at equilibrium is 5.46×10^{-4} a.u. at a DNA concentration of 0.1 mg/mL. This increases up to a value of 8.08×10^{-4} a.u. with a BSA:DNA ratio of 15.1, representing a 48% increase in the amount of DNA adsorbed. A marked increase of DNA adsorption onto kaolinite and montmorillonite due to association with other biomolecules has been observed previously.[78] With associated constitutional organic components (proteins, lipids and polysaccharides) and cellular wall debris, the amount of DNA adsorbed on montmorillonite and kaolinite clays was greater than the amount adsorbed when DNA was first purified to remove associated biomolecules.[78] The

authors propose three factors responsible for observed increased adsorption: a change in DNA morphology (size, flexibility and conformation) induced by associated biomolecules, DNA condensation/aggregation to a more compact state induced by associated biomolecules (e.g. lipids, proteins, polysaccharides), and bridging between DNA and the clay surfaces by DNA-bound biomolecules. While DLS results do not necessarily suggest condensation and compaction of DNA upon BSA addition, they do highlight a possible aggregation of DNA/BSA complexes through reduction of intermolecular repulsion between DNA strands as BSA is added. Repulsion between adsorbed DNA molecules has been identified as a limiting factor for adsorption capacity on surfaces, attenuating these interactions in solution could allow for more adsorption of DNA.[79,80] This interpretation lines up with electrophoretic mobilityresults, which show a decrease of net negative charge on formed complexes with increasing BSA addition.

While our results correspond with an increase in adsorbed DNA when the BSA:DNA ratio ≤15.1, when the BSA:DNA ratio increases to 18.9 the amount of DNA adsorbed decreases, with an average ν C-C peak height of 5.95×10^{-4} a.u. Under these conditions, the decrease of ν C-C peak height may be explained by the initial adsorption of loosely bound or free BSA onto goethite, as demonstrated by the adsorption kinetics above DNA binding saturation (**Figure 4.5a**). Bound BSA may subsequently block surface sites on goethite, making them inaccessible for adsorption of DNA/BSA complexes. Blocking of DNA adsorption sites on andosol soils and model minerals by adsorbed α-casein was previously identified as a possible explanation for reduction of DNA adsorption in the presence of protein in solution.[81]

Unlike the relative amount of DNA adsorbed, direct binding of DNA to goethite, as indicated by ν Fe-O-P peak height, does not appear to be influenced by BSA:DNA ratio in solution at ratios ≤15.1. At a BSA:DNA ratio of 18.9, a decrease in ν Fe-O-P peak height is observed (**Figure 4.5b**). When normalized to the ν C-C peak height (amount of DNA adsorbed within DNA/BSA complexes), the extent of direct DNA-goethite coordination at equilibrium decreases with increasing BSA:DNA ratio in solution, even though an increase in adsorbed DNA is observed until a BSA:DNA ratio of 15.1 (**Figure 4.5c**). This indicates that BSA associated with DNA is preventing direct bonding between DNA in DNA/BSA complexes and goethite, possibly through steric hindrance or by direct interaction between BSA and backbone phosphate groups on DNA. This observation provides support for BSA bridging as playing a role in the adsorption of DNA/BSA supramolecular associations on goethite.

Our results are from a study with a set of models in a single solution condition (5 mM KCl at 5 pH = 5.0). To view these results in a broader environmental context, influence of different ionic strength, pH and biomolecular species on both supramolecular association and adsorption on soil minerals should be considered. Generally, supramolecular association of organic matter increases with an increase in ionic strength through reduction in double layer thickness.[82-84] If polyvalent cations are present they may act as a bridge between DOM molecules, enhancing association as well.[82,84] Weaker association would generally be expected as pH values favor greater electrostatic repulsion between constituent molecules.[82-84]This does not, however, suggest that association of like-charged biomolecules within DOM does not occur (as demonstrated by this and previous studies on supramolecular assembly) as localized

charge heterogeneity may favor interaction.[62,85] All of these points would be dependent upon the charge characteristics of constituent molecules. Under aforementioned conditions where supramolecular assembly may not be as favorable, adsorption dynamics may favor adsorption of individual DOM molecules rather than supramolecular complexes. When conditions favor supramolecular association, the influence of intermolecular binding could potentially influence surface adsorption, as demonstrated here. It should be noted that, due to analytical limitations, experimental concentrations used in this study (0.1 mg/mL DNA and 0.1-0.5 mg/mL BSA) correspond with high surface coverage and are higher than would be expected in soil solution.[13,28,29] This may lead to an over-emphasis of the reduction of intermolecular repulsion between adsorbed species on surfaces as shown here. In natural systems where concentrations and subsequent surface coverages would be lower, these findings may not be as relevant. Some influence of supramolecular association on binding directly at the interface could still be likely at lower surface coverages, as they seem to depend more on the binding between molecules within complexes, rather than interactions between neighboring adsorbed biomolecules.

Influence of Supramolecular Assembly on Organic Matter Retention by Minerals. This work demonstrates how solution DNA-BSA binding behavior results in supramolecular associations differing in properties and how this influences the mechanism and amount of retention of constituent biomolecules on a goethite surface. As BSA binds to DNA in solution, intermolecular repulsion between DNA strands is screened (**Figure 4.6**). This is reflected at the aqueous goethite interface by an increase in the amount of DNA adsorbed with increasing BSA content up to a

BSA:DNA ratio of 15.1. Beyond this ratio, CD spectroscopy suggests BSA binding sites on DNA become saturated, resulting free or loosely bound BSA in solution. BSA added in the saturated binding regime appears to adsorb rapidly and before DNA/BSA complexes, blocking surface sites from DNA/BSA complexes. DNA retention is thus reduced when BSA:DNA ratio is 18.9. The mechanism of retention also appears to be influenced by interaction between DNA and BSA in solution, with more pronounced blocking of inner-sphere interaction between DNA and goethite with increasing BSA content in DNA/BSA complexes. Coupled with an increase in the amount of DNA adsorbed with greater extent of BSA binding, this result suggests BSA bridging between DNA and goethite occurs.

These results enhance our understanding of how biomolecules are retained by minerals in natural systems, where association amongst organic molecules in solution occurs before contact with mineral surfaces. Amount and mechanism of organic matter retention may have implications for stabilization of organic matter within organo-mineral associations, as adsorbed organic matter is generally believed to be more stable than DOM. Additionally, the strength of interaction between adsorbed organic matter and mineral surfaces has been linked to stability of adsorbed SOM, with ligand exchange and bond formation believed to be particularly important for organic matter stability.[8] Considering the impact of BSA associated with DNA on the formation of an inner-sphere Fe-O-P bond, it is conceivable that stability of adsorbed biomolecules could be influenced through initial supramolecular association by altering adsorption mechanism on mineral surfaces. Recent results probing the adsorption of model organic molecules to goethite under similar solution conditions

(pH = 6.0 in 10 mM NaCl) demonstrate that functional groups in contact with a mineral surface impacts bond strength, which suggests that altering the ratio of molecules in supramolecular associations could impact bonding energetics at mineral surfaces.[86]

It has been long understood that OM is retained by soils in multilayers, with layering often attributed to successive adsorption of biomolecules onto mineral surfaces.[7,87] This work also demonstrates that multilayers may be formed on mineral surfaces in a single adsorption event of supramolecular complexes, in addition to a series of adsorption events of individual biomolecules. Given the propensity of DOM molecules to form supramolecular complexes in soil solution, these findings may be a particularly relevant, yet overlooked, factor in natural systems. Better understanding these processes in the future may strengthen our concept of organic matter stabilization in soils and global nutrient cycling.

Acknowledgements. This work made use of the Cornell Center for Materials Research Shared Facilities which are supported through the NSF MRSEC program (DMR-1719875). Support was provided by the School of Integrative Plant Science within the College of Agriculture and Life Sciences at Cornell University. Additional support was provided by the Atkinson Center for a Sustainable Future.

Figure 4.1 a) DNA-BSA binding curve from circular dichroism spectroscopic measurements. Data points represent the change in DNA molar absorptivity with respect to a range of BSA:DNA ratios. The dashed red line represents the model fit to the Hill equation. Error bars represent standard deviation of measurements (n=3). **b)** Electrophoretic mobility values for DNA/BSA complexes synthesized with different amounts of BSA at pH=5.0 in 5 mM KCl. The dashed orange and blue lines represent the electrophoretic mobilities of BSA and DNA by themselves, respectively. Error bars represent standard deviation of measurements (n=3). Corresponding BSA:DNA ratios are displayed above data points.

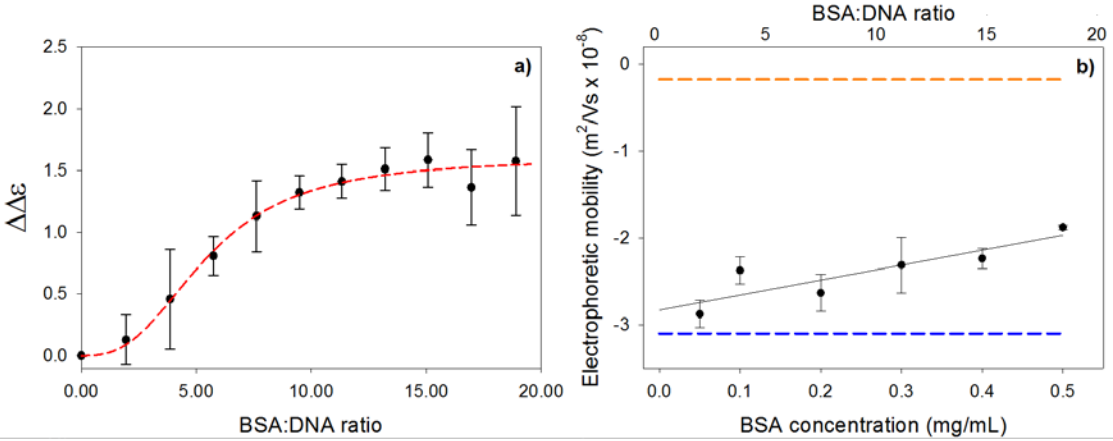

Figure 4.2 a) Relaxation time distributions for DNA, BSA and experimental BSA:DNA ratios. **b)** Diffusion coefficients associated with fast (red circles) and slow (blue triangles) relaxation modes of DNA and DNA/BSA complexes at experimental BSA concentrations. Corresponding BSA:DNA ratios are displayed above data points. The diffusion coefficient for BSA (not delineated here) was determined to be 41.0 x 10^{-8} cm^2/s, relatively higher than coefficients shown for DNA and DNA/BSA complexes.

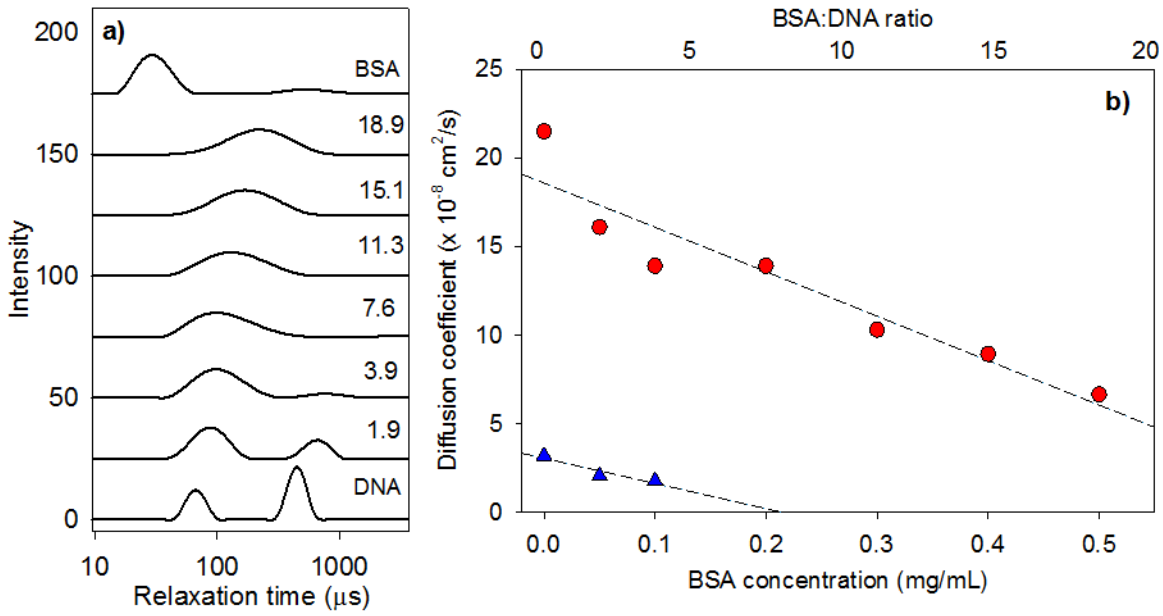

Figure 4.3 ATR-FTIR spectra of BSA and DNA in solution and adsorbed on goethite at equilibrium and DNA/BSA adsorbed on goethite at a BSA:DNA ratio of 7.6. Dashed lines correspond with vibrations from BSA backbone (green), DNA nucleobases (purple) and DNA backbone (red).

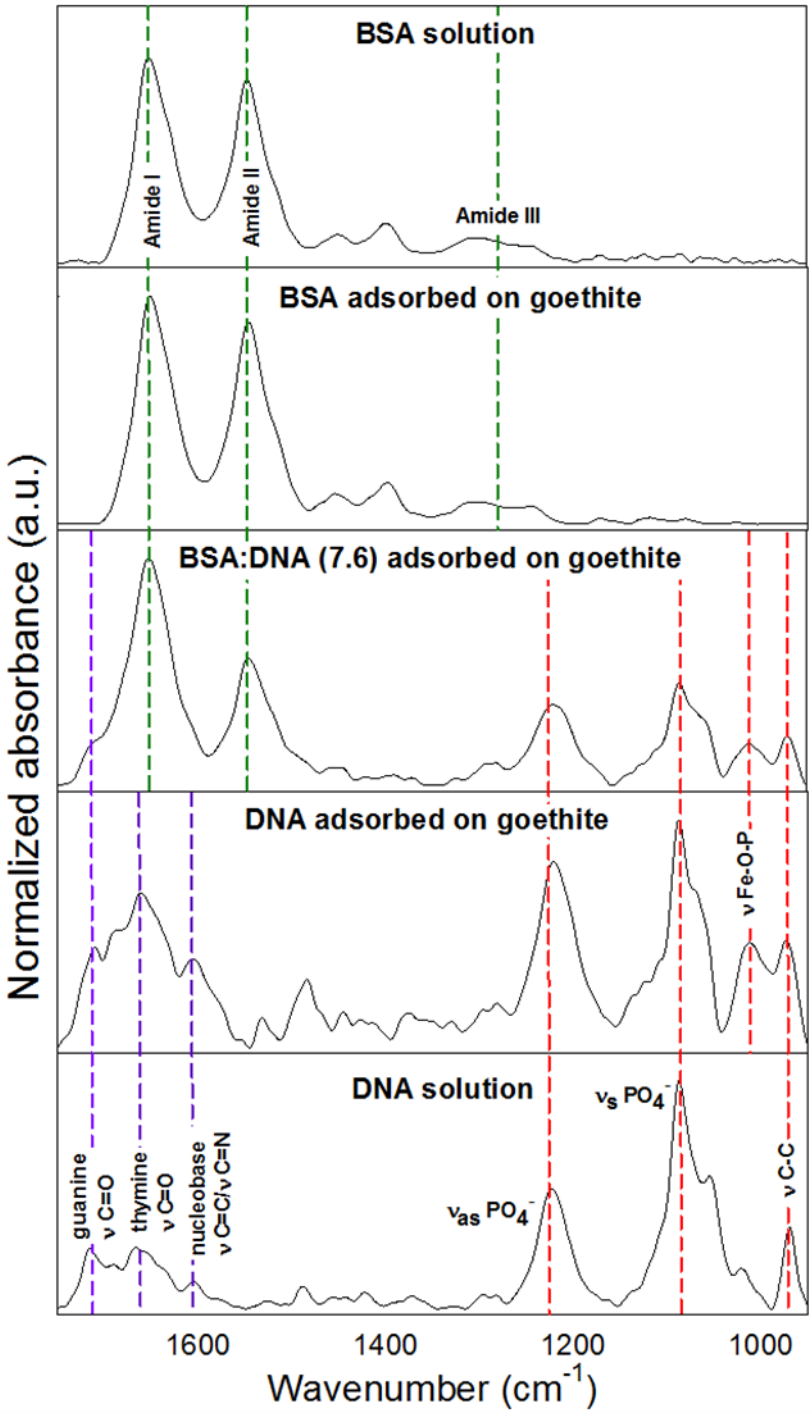

Figure 4.4 ATR-FTIR spectra of biomolecules adsorbed on goethite at 3 (red), 7 (grey), 23 (orange), 67 (green) and 99 (blue) minutes at BSA:DNA ratio of 18.9. Inset shows BSA amide II (red circles) and DNA ν C-C (blue circles) peak heights at time points for shown experiment.

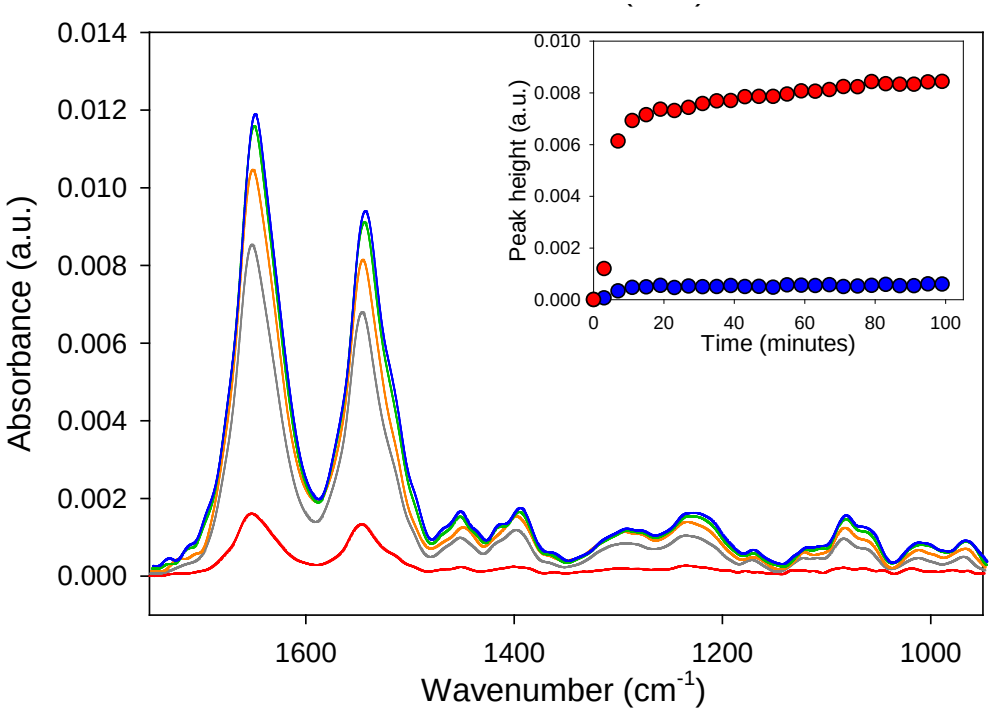

Figure 4.5 a) Amide II : ν C-C peak ratios with adsorption time for BSA:DNA ratios of 3.9 (black x), 7.6 (green circles), 11.3 (upside down red triangles), 15.1 (blue diamonds) and 18.9 (orange squares). **b)** Heights for DNA ν C-C (black) and ν Fe-O-P (green) at equilibrium for experimental BSA:DNA ratios. **c)** ν Fe-O-P/ ν C-C peak height ratios for each BSA:DNA ratio used in experiments. Corresponding BSA:DNA ratios are shown above data points in b) and c). ν C-C and ν Fe-O-P represent the amount of DNA adsorbed and direct coordination of adsorbed DNA, respectively.

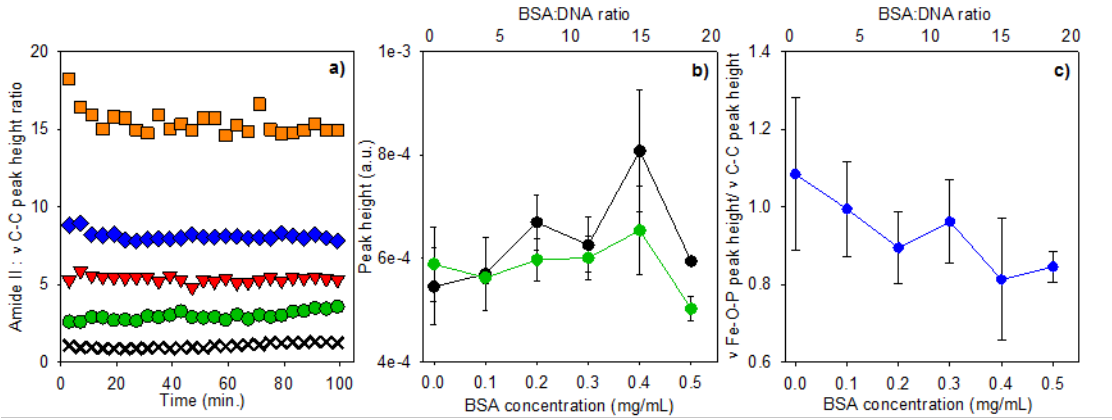

Figure 4.6 Conceptual figure highlighting the influence of associated BSA on the adsorption of DNA on goethite. Helices represent DNA and blue shapes indicate BSA. Green-shaded ovals depict zones of intermolecular repulsion between DNA and DNA/BSA complexes. Dashed red lines correspond with direct coordination between DNA and goethite through Fe-O-P bonding.

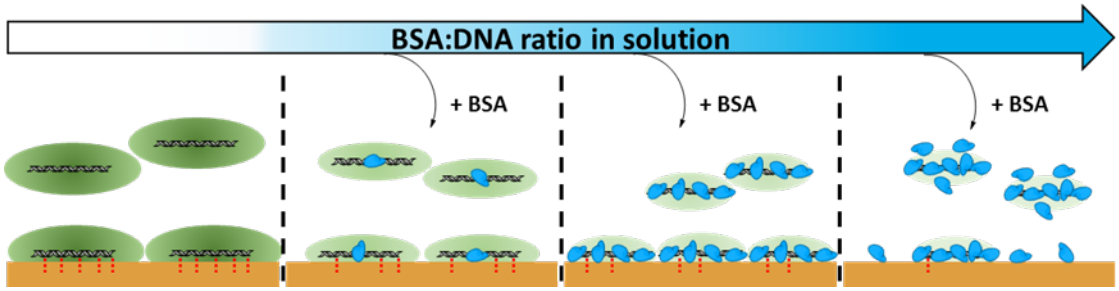

REFERENCES

(1) Baldock, J. A. Composition and cycling of organic carbon in soil. In *Nutrient Cycling in Terrestrial Ecosystems*; Marschner, P., Rengel, Z., Eds.; Springer-Verlag: Berlin, 2007; pp 1-35.

(2) Swift, R. S. Sequestration of Carbon by Soil. *Soil Sci.* **2001,** *166,* 858-871.

(3) Lal, R. Soil Carbon Sequestration to Mitigate Climate Change. *Geoderma* **2004,** *123,* 1-22.

(4) Six, J.; Conant, R. T.; Paul, E. A.; Paustian, K. Stabilization Mechanisms of Soil Organic Matter: Implications for C-saturation of Soils. *Plant Soil* **2002,** *241,* 155-176.

(5) Mikutta, R.; Mikutta, C.; Kalbitz, K.; Scheel, T.; Kaiser, K.; Jahn, R. Biodegradation of forest floor organic matter bound to minerals via different binding mechanisms. *Geochim. Cosmochim. Acta* **2007,** *71,* 2569-2590.

(6) Torn, M. S.; Trumbore, S. E.; Chadwick, O. A.; Vitousek, P. M.; Hendricks, D. M. Mineral Control of Soil Organic Carbon Storage and Turnover. *Nature,* **1997,** *389,* 170-173.

(7) Kleber, M.; Sollins, P.; Sutton, R. A Conceptual Model of Organo-mineral Interactions in Soils: Self-assembly of Organic Molecular Fragments into Zonal Structures on Mineral Surfaces. *Biogeochemistry* **2007,** *85,* 9-24.

(8) Keil, R. G.; Mayer, L. M. *Mineral Matrices and Organic Matter, Treatise on Geochemistry,* 2nd ed.; Elsevier: New York, 2014; pp 337-359.

(9) Kalbitz, K.; Schwesig, D.; Rethemeyer, J.; Matzner, E. Stabilization of Dissolved Organic Matter by Sorption to the Mineral Soil. *Soil Biol. Biochem.* **2005,** *37,* 1319-1331.

(10) Hazen, R. M.; Sverjensky, D. A. Mineral Surfaces, Geochemical Complexities, and the Origins of Life. *Cold Spring Harb. Perspect. Biol.* **2010,** *2,* 1-21.

(11) Lin, Z.; Hu, R.; Zhou, J.; Ye, Y.; Xu, Z.; Lin, C. A Further Insight into the Adsorption Mechanism of Protein on Hydroxyapatite by FTIR-ATR Spectrometry. *Spectrochim. Acta Mol. Biomol. Spectrosc.* **2017,** *173,* 527-531.

(12) Johnston, C.T.; Premachandra, G.S.; Szabo, T.; Lok, J.; Schoonheydt, R.A. Interaction of biological molecules with clay minerals: a combined spectroscopic and sorption study of lysozyme on saponite. *Langmuir* **2012,** *28,* 611-619.

(13) Schmidt, M. P.; Martínez, C. E. Ironing out Genes in the Environment: An Experimental Study of the DNA-Goethite Interface. *Langmuir* **2017,** *33,* 8525-8532.

(14) Givens, B. E.; Xu, Z.; Fiegel, J.; Grassian, V. H. Bovine Serum Albumin Adsorption on SiO_2 and TiO_2 Nanoparticle Surfaces at Circumneutral and Acidic pH: A Tale of Two Nano-bio Surface Interactions. *J. Colloid Interface Sci.* **2017,** *493,* 334-341.

(15) Schmidt, M. P.; Martínez, C. E. Kinetic and Conformational Insights of Protein Adsorption onto Montmorillonite Revealed using in Situ ATR-FTIR/2D-COS. *Langmuir* **2016,** *32,* 7719-7729.

(16) Thyveetil, M. A.; Coveney, P. V.; Greenwell, H. C.; Suter, J. L. Computer Simulation Study of the Structural Stability and Materials Properties of DNA-Intercalated Layered Double Hydroxides. *J. Am. Chem. Soc.* **2008,** *130, 4742-*

4756.
(17) Kolman, K.; Makowski, M.M.; Golriz, A.A.; Kappl, M.; Piglowski, J.; Butt, H.J.; Kiersnowski, A. Adsorption, Aggregation, and Desorption of Proteins on Smectite Particles. *Langmuir* **2014,** *30,* 11650-11659.
(18) Liu, X.; Eusterhues, K.; Theime, J.; Ciobota, V.; Höschen, C.; Mueller, C. W.; Küsel, K.; Kögel-Knabner, I.; Rösch, P.; Popp, J.; Totsche, K. U. STXM and NanoSIMS Investigations on EPS Fractions before and after Adsorption to Goethite. *Environ. Sci. Technol.* **2013,** *47,* 3158-3166.
(19) Nguyen, T. H.; Elimelech, M. Plasmid DNA Adsorption on Silica: Kinetics and Conformational Changes in Monovalent and Divalent Salts. *Biomacromolecules* **2007,** *8,* 24-32.
(20) Cai, P.; Huang, Q.; Zhang, X. Interactions of DNA with Clay Minerals and Soil Colloidal Particles and Protection against Degradation by DNase *Environ. Sci. Technol.* **2006,** *40,* 2921-2926.
(21) Haynes, C. A.; Norde, W. Globular Proteins at Solid/Liquid Interfaces. *Colloids Surf., B* **1994,** *2,* 517-566.
(22) Sutton, R.; Spositio, G. Molecular Structure in Soil Humic Substances: The New View. *Environ. Sci. Technol.* **2005,** *39,* 9009-9015.
(23) Krueger, J. K.; McCrary, B. S.; Wang, A. H. J.; Shriver, J. W.; Trewhella, J.; Edmondson, S. P. The Solution Structure of the Sac7d/DNA Complex: A Small-Angle X-ray Scattering Study. *Biochemistry* **1999,** *38,* 10247-10255.
(24) Tomaszewski, J. E.; Schwarzenbach, R. P.; Sander, M. Protein Encapsulation by Humic Substances. *Environ. Sci. Technol.* **2011,** *45,* 6003-6010.
(25) Giachin, G.; Narkiewicz, J.; Scaini, D.; Ngoc, A. T.; Margon, A.; Sequi, P.; Leita, L.; Legname, G. Prion Protein Interaction with Soil Humic Substances: Environmental Implications. *PLoS One* **2014,** *9,* p. e100016.
(26) Perico, A.; Ciferri, A. The Supramolecular Association of Polyelectrolytes to Complementary Charged Surfactancts and Protein Assemblies. *Chem. Eur. J.* **2009,** *15,* 6312-6320.
(27) Neihardt, F. C.; Ingraham, J. L.; Schaechter, M. *Physiology of the Bacterial Cell: A Molecular Approach;* Sinauer Associate, Inc.: Sunderland, MA, 1990.
(28) Niemeyer, J.; Gessler, F. Determination of free DNA in soils. *J. Plant Nutri. Soil Sci.* **2002,** *165,* 121-124.
(29) Roberts, P.; Jones, D. L. Critical Evaluation of Methods for Determining Total Protein in Soil Solution. *Soil Biol. Biochem.* **2008,** *40,* 1485-1495.
(30) Schulze, W. X. Protein analysis in dissolved organic matter: What proteins from organic debris, soil leachate and surface water can tell us – a perspective. *Biogeosciences* **2005,** *2,* 75-86.
(31) Chourey, K.; Jansson, J.; VerBerkmoes, N.; Shah, M.; Chavarria, K. L.; Tom, L. M.; Brodie, E. L.; Hettich, R. L. Direct Cellular Lysis/Protein Extraction Protocol for Soil Metaproteomics. *J. Proteome Res.* **2010,** *9,* 6615-6622.
(32) Benndorf, D.; Balcke, G. U.; Harms, H.; von Bergen, M. Functional metaproteome analysis of protein extracts from contaminated soil and groundwater. *ISME J.* **2007,** *1,* 224-234.
(33) Rooman, Marianne and Wintjens, René (Mar 2015) Protein-DNA Interactions. In:

eLS. John Wiley & Sons Ltd, Chichester. http://www.els.net/[doi:10.1002/9780470015902.a0001348.pub3]
(34) von Hippel, P. H. From “Simple” DNA-Protein Interactions to the Macromolecular Machines of Gene Expression. *Annu. Rev. Biophys. Biomol. Struct.* **2007,** *36,* 79-105.
(35) Corsaro, A.; Anselmi, C.; Polano, M.; Aceto, A.; Florio, T. De Nobili, M. The Interation of Humic Substances with the Human Prion Protein Fragment 90-231 Affects Its Protease K Resistance and Cell Internalization. *J. Biol. Requl. Homeost. Agents* **2010,** *24,* 27-39.
(36) Nielsen, K.M.; Calamai, L.; Pietramellara, G. Stabilization of Extracellular DNA and Proteins by Transient Binding to Various Soil Components. In *Nucleic Acids and Proteins in Soil*; Nannipieri, P.; Smalla, K., Eds.; Springer-Verlag: Heidelberg, 2006; pp 141-153
(37) Mundunkotuwa, I.A.; Minshid, A.A.; Grassian, V.H. ATR-FTIR spectroscopy as a tool to probe surface adsorption on nanoparticles at the liquid-solid interface in environmentally and biologically relevant media. *Analyst* **2014,** *139,* 870-881.
(38) Pietramellara, G.; Franchi, M.; Gallori, E.; Nannipieri, P. Effect of molecular characteristics of DNA on its adsorption and binding on homoionic montmorillonite and kaolinite. *Biol. Fertil. Soils* **2001,** *33,* 402-409.
(39) Schwertmann, U.; Cornell, R.M. *Iron Oxides in the Laboratory: Preparation and Characterization;* VCH: Weinheim; New York, 1991.
(40) Messer, W. ; Blaesing, F.; Jakimowicz, D.; Krause, M.; Majka, J.; Nardmann, J.; Schaper, S.; Seitz, H.; Speck, C.; Weigel, C.; Wegrzyn, G.; Welzeck, M.; Zkrzewska-Czerwinska, J. Bacterial replication initiator DnaA. Rules for DnaA binding and roles of DnaA in origin unwiding and helicase loading. *Biochimie* **2001,** *83,* 5-12.
(41) Hianik, T.; Ostatná, V.; Zajacová, Z. The study of the binding of globular proteins to DNA using mass detection and electrochemical indicator methods. *J. Electroanal. Chem.* **2004,** *564,* 19-24.
(42) Cary, P. D.; Kneale, G. G. Circular Dichroism for the Analysis of Protein-DNA Interactions. *Methods Mol. Biol.* **2009,** *543,* 613-624.
(43) Papapanagiotou, I.; Streeter, S. D.; Cary, P. D.; Kneale, G. G. DNA Structural Deformations in the Interaction of the Controller Protein C.Ahdl with its Operator Sequence. *Nucleic Acids Res.* **2007,** *35,* 2643-2650.
(44) Goldberg, M. E.; Chaffotte, A. F. Undistorted structural analysis of soluble proteins by attenuated total reflectance infrared spectroscopy. *Protein Sci.* **2005,** *14,* 2781-2792.
(45) Beattie, D. A.; Chapelet, J. K.; Gräfe, M.; Skinner, W. M.; Smith E. In Situ ATR FTIR Studies of SO_4 Adsorption on Goethite in the Presence of Copper Ions *Environ. Sci. Technol.* **2008,** *42,* 9191-9196.
(46) Xia, Y.; Chen, E.; Liang, D. Recognition of Single- and Double-Stranded Oligonucleotides by Bovine Serum Albumin via Nonspecific Interactions. *Biomacromolecules* **2010,** *11,* 3158-3166.
(47) Emperle, M.; Rajavelu, A.; Reinhardt, R.; Jurkowska, R. Z.; Jeltsch, A. Cooperative DNA Binding and Protein/DNA Fiber Formation Increases the

Activity of the Dnmt3a DNA Methyltransferase. *J. Biol. Chem.* **2014,** *289,* 29602-29613.
(48) Greenfield, N. J. Circular Dichroism Analysis for Protein-Protein Interactions. *Methods Mol. Biol.* **2004,** *261*, 55−78.
(49) Lorber, B.; Fischer, F.; Bailly, M.; Roy, H.; Kern, D. Protein Analysis by Dynamic Light Scattering: Methods and Techniques for Students. *Biochem. Mol. Biol. Educ.* **2012,** *40,* 372-382.
(50) Valstar, A.; Almgren, M.; Brown, W. The Interaction of Bovine Serum Albumin with Surfactants Studied by Light Scattering. *Langmuir* **2000,** *16,* 922-927.
(51) Serdyuk, I. N.; Zaccai, N. R.; Zaccai, J. *Methods in Molecular Biophysics: Structure, Dynamics, Function;* Cambridge University Press: New York, 2007.
(52) Cárdenas, M.; Schillén, K.; Nylander, T.; Jansson, J.; Lindman, B. DNA Compaction by Cationic Surfactant in Solution and at Polystyrene Particle Solution Interfaces: A Dynamic Light Scattering Study. *Phys. Chem. Chem. Phys.* **2004,** *6,* 1603-1607.
(53) Borsali, R.; Nguyen, H.; Pecora, R. Small-Angle Neutron Scattering and Dynamic Light Scattering from a Polyelectrolyte Solution: DNA. *Macromolecules* **1998,** *31,* 1548-1555.
(54) Lundberg, D.; Carnerup, A. M.; Janiak, J.; Schillén, K.; Miguel, M. G.; Lindman, B. Size and Morphology of Assemblies Formed by DNA and Lysozyme in Dilute Aqueous Mixtures. *Phys. Chem. Chem. Phys.* **2011,** *13,* 3082-3091.
(55) Costa, T.; Melo, J. S.; Miguel, M. G.; Lindman, B.; Schillén, K. Complex Formation between a Fluorescently-Labled Polyelectrolyte and a Triblock Copolymer. *J. Phys. Chem. B* **2009,** *113,* 6205-6214.
(56) Sedlák, M.; Amis, E. J. Dynamics of Moderately Concentrated Salt-free Polyelectrolyte Solutions: Molecular Weight Dependence. *J. Chem. Phys.* **1992,** *96,* 817-825.
(57) Schmitz, K. *An Introduction to Dynamic Light Scattering by Macromolecules*; Academic Press: San Diego, CA, 1990.
(58) Fulmer, A. W.; Benbasat, J. A.; Bloomfield, V. A. Ionic strength effects on macroion diffusion and excess light-scattering intensities of short DNA rods. *Biopolymers* **1981,** *20,* 1147-1159.
(59) Viadu, H.; Aggarwal, A. K. Structure of BamHI Bound to Nonspecific DNA: A Model for DNA Sliding. *Mol. Cell* **2000,** *5,* 889-895.
(60) Majorek, K. A.; Porebski, P. J.; Dayal, A.; Zimmerman, M. D.; Jablonska, K.; Stewart, A. J.; Chruszcz, M.; Minor, W. Structural and immunologic characterization of bovine, horse and rabbit serum albumins. *Mol. Immunol.* **2012,** *52,* 174-182.
(61) Peters Jr., T. *All about Albumin: Biochemistry, Genetics, and Medical Applications,* 1st ed.; Academic Press: San Diego, 1995.
(62) Mattison, K. W.; Dubin, P. L.; Brittain, I. J. Complex Formation between Bovine Serum Albumin and Strong Polyelectrolyes: Effect of Polymer Charge Density. *J. Phys. Chem. B.* **1998,** *102,* 3830-3836.
(63) Some, D. Light-scattering-based Analysis of Biomolecular Interactions. *Biophys. Rev.* **2013,** *5,* 147-158.

(64) Barth, A.; Zscherp, C. What Vibrations Tell Us about Proteins. *Q. Rev. Biophys.* **2002,** *35,* 369-430.
(65) Ishida, K. P.; Griffiths, P. R. Comparison of the Amide I/II Intensity Ratio of Solution and Solid-State Proteins Sampled by Transmission, Attenuated Total Reflectance, and Diffuse Reflectance Spectrometry. *Appl. Spectrosc.* **1993,** *47,* 584-589.
(66) Cai, S.; Singh, B. R. A Distinct Utility of the Amide III Infrared Band for Secondary Structure Estimation of Aqueous Protein Solutions Using Partial Least Squares Methods. *Biochemistry* **2004,** *43,* 2541-2549.
(67) Arai, T.; Norde, W. The behavior of some model proteins at solid-liquid interfaces 1. Adsorption from single protein solutions. *Colloids Surfaces* **1990,** *51,* 1-15.
(68) Banyay, M.; Sarkar, M.; Gräslund. A. A library of IR bands of nucleic acids in solution *Biophys. Chem.* **2003,** *104,* 477-488.
(69) Calais, T.; Playe, B.; Ducéré, J. M.; Veyan, J. F.; Rupich, S.; Hemeryck, A.; Rouhani, M. D.; Rossi, C.; Chabal, Y. J.; Estève, A. Role of Alumina Coatings for Selective and Controlled Bonding of DNA on Technologically Relevant Oxide Surfaces *J. Phys. Chem. C* **2015,** *119,* 23527-23543.
(70) Pershina, A.G.; Sazonov, A. E.; Ogorodova, M. L. Investigation of the Interaction between DNA and Cobalt Ferrite Nanoparticles by FTIR Spectroscopy *Russ. J. Bioorg. Chem.* **2009,** *35,* 607-613.
(71) Gagnasso, M.; Boero, V.; Franchini, M. A.; Chorover, J. ATR-FTIR studies of phospholipid vesicle interactions with α-FeOOH and α-Fe_2O_3 surfaces *Colloids Surf., B* **2010,** *76,* 456-467.
(72) Parikh, S. J.; Chorover, J. ATR-FTIR Spectroscopy Reveals Bond Formation During Bacterial Adhesion to Iron Oxide *Langmuir* **2006,** *22,* 8492-8500.
(73) Omoike, A.; Chorover, J.; Kwon, K. D.; Kubicki, J. D. Adhesion of Bacterial Exopolymers to α-FeOOH: Inner-Sphere Complexation of Phosphodiester Groups *Langmuir* **2004,** *20,* 11108-11114.
(74) Fink, D.J.; Hutson, T.B.; Chittur, K. K.; Leininger, R. I.; Gendreau, R. M. Quantitative surface studies of protein adsorption by infrared spectroscopy. II. Quantitation of adsorbed and bulk proteins. *Anal. Biochem.* **1987,** *165,* 147-154.
(75) Chittur, K. K. FTIR/ATR for protein adsorption to biomaterial surfaces. *Biomaterials* **1998,** *19,* 357-369.
(76) Tajmir-Riahi, H. A.; N'soukpoé-Kossi, C. N.; Joly, D. Structural Analysis of Protein-DNA and Protein-RNA Interactions by FTIR, UV-Visible and CD Spectroscopic Methods. *Spectroscopy* **2009,** *23,* 81-101.
(77) Ding, X.; Henrichs, S. M.; Adsorption and Desorption of Proteins and Polyamino Acids by Clay Minerals and Marine Sediments. *Mar. Chem.* **2002,** *77,* 225-237.
(78) Pietramellara, G.; Ascher, J.; Ceccherinie, M. T.; Nannipieri, P.; Wenderoth, D. Adsorption of Pure and Dirty Bacterial DNA on Clay Minerals and their Transformation Frequency. *Biol. Fertil. Soils* **2007,** *43,* 731-739.
(79) Melzak, K. A.; Sherwood, C. S.; Turner, R. F. B.; Haynes, C. A. Driving Forces for DNA Adsorption to Silica in Perchlorate Solutions. *J. Colloid Interface Sci.* **1996,** *181,* 635-644.

(80) Cai, P,; Huang, Q.; Zhang, X. Microcalorimetric Studies of the effects of $MgCl_2$ Concentrations and pH on the Adsorption of DNA on Montmorillonite, Kaolinite and Goethite. *Appl. Clay Sci.* **2006,** *32,* 147-152.
(81) Saeki, K.; Sakai, M.; Kunito, T. Effect of α-Casein on DNA Adsorption by Andosols and by Soil Components. *Biol. Fertil. Soils* **2012,** *48,* 469-474.76.
(82) Tsang, D.C.W. Influence of Natural Organic Matter on Contaminant Removal by Permeable Reactive Barrier. In *The Role of Colloidal Systems in Environmental Protection;* Fanun, M., Ed.; Elsevier BV: Amsterdam, The Netherlands, 2014; pp 19-40.
(83) Tombácz, E. Colloidal Properties of Humic Acids and Spontaneous Changes of their Colloidal State Under Variable Solution Conditions. *Soil Sci.* **1999,** *164,* 814-824.
(84) Schaumann, G. E. Soil organic matter beyond molecular structure Part I: Macromolecular and supramolecular characteristics. *J. Plant. Nutr. Soil Sci.* **2006,** *169,* 145-156.
(85) Tomaszewski, J. E.; Schwarzenbach, R. P.; Sander, M. Protein Encapsulation by Humic Substances. *Environ. Sci. Technol.* **2011,** *45,* 6003-6010.
(86) Newcomb, C. J.; Qafoku, N. P.; Grate, J. W.; Bailey, V. L.; De Yoreo, J. J. Developing a molecular picture of soil organic matter-mineral interactions by quantifying organo-mineral binding. *Nat. Commun.* **2017,** *8,* doi:10.1038/s41467-017-00407-9.
(87) Mayer, L. M.; Xing, B. Organic Matter-Surface Area Relationships in Acid Soils. *Soil Sci. Soc. Am. J.* **2001,** *65,* 250-258.

Figure A1.1. Concentration of Fe in crystalline (red), poorly-crystalline (yellow) and organically-bound (blue) forms for MB (top) and NT (bottom) soils.

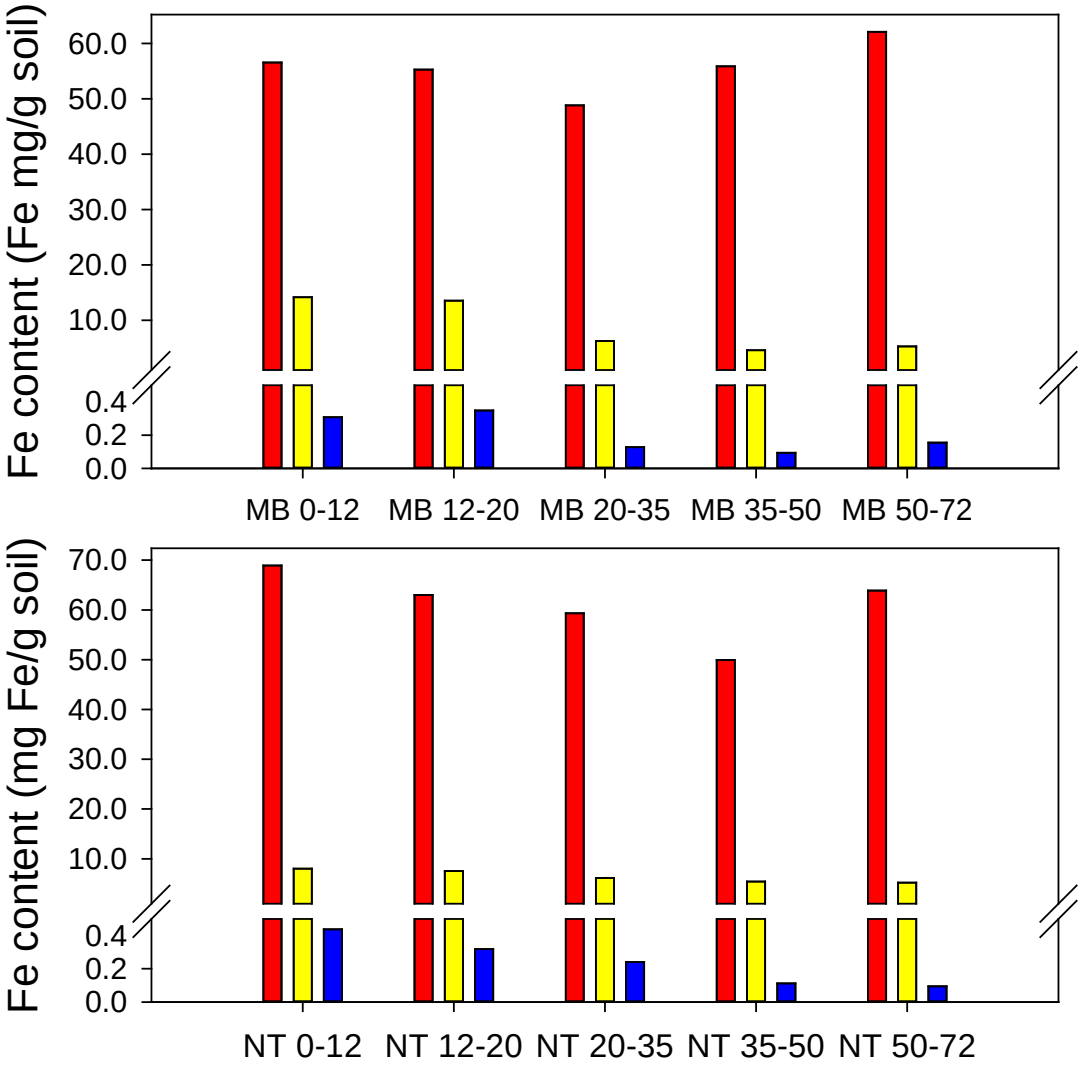

Figure A1.2 Concentration of Fe in crystalline (red), poorly-crystalline (yellow) and organically-bound (blue) forms for MB (top) and NT (bottom) soils.

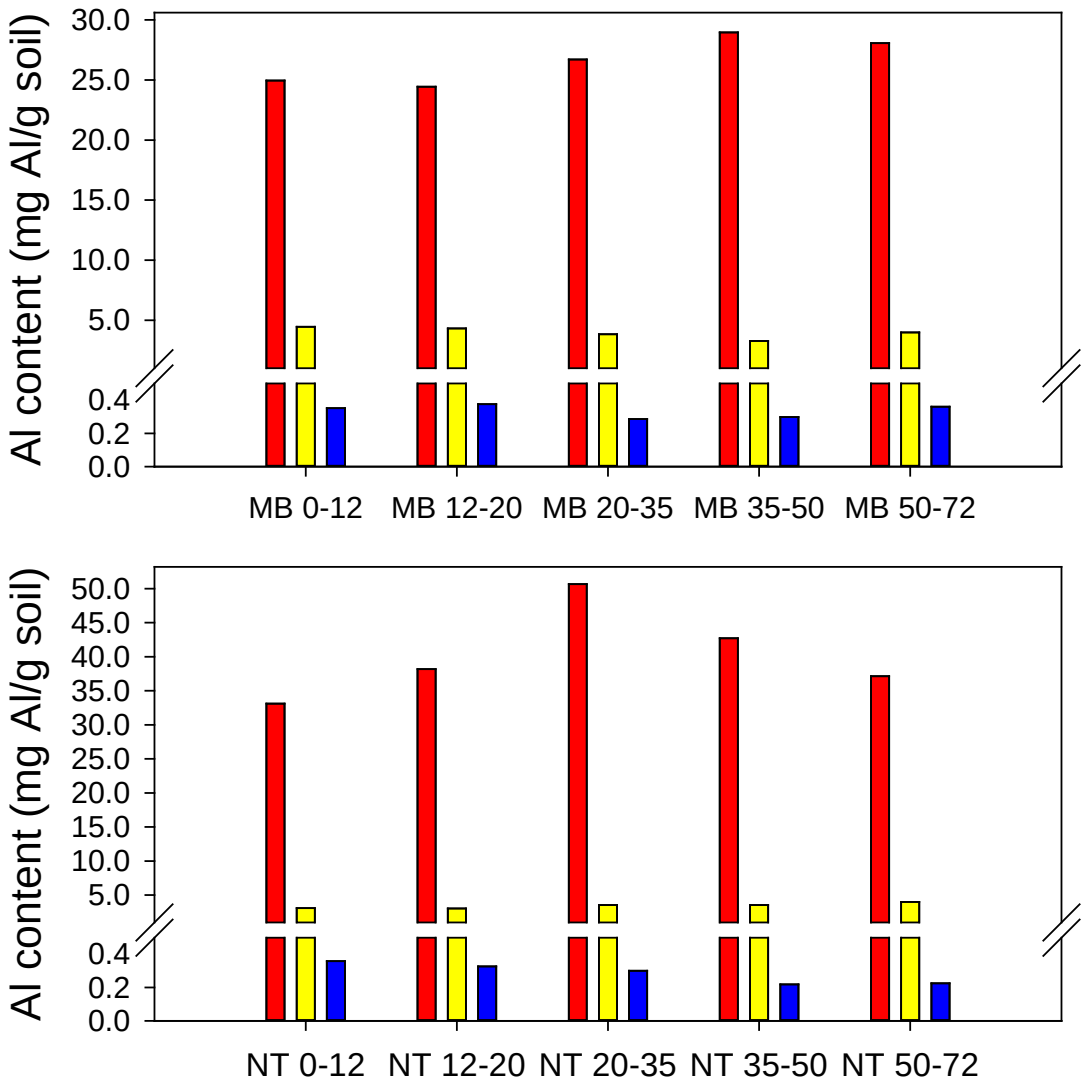

Figure A1.3 FTIR spectra of bulk MB soils

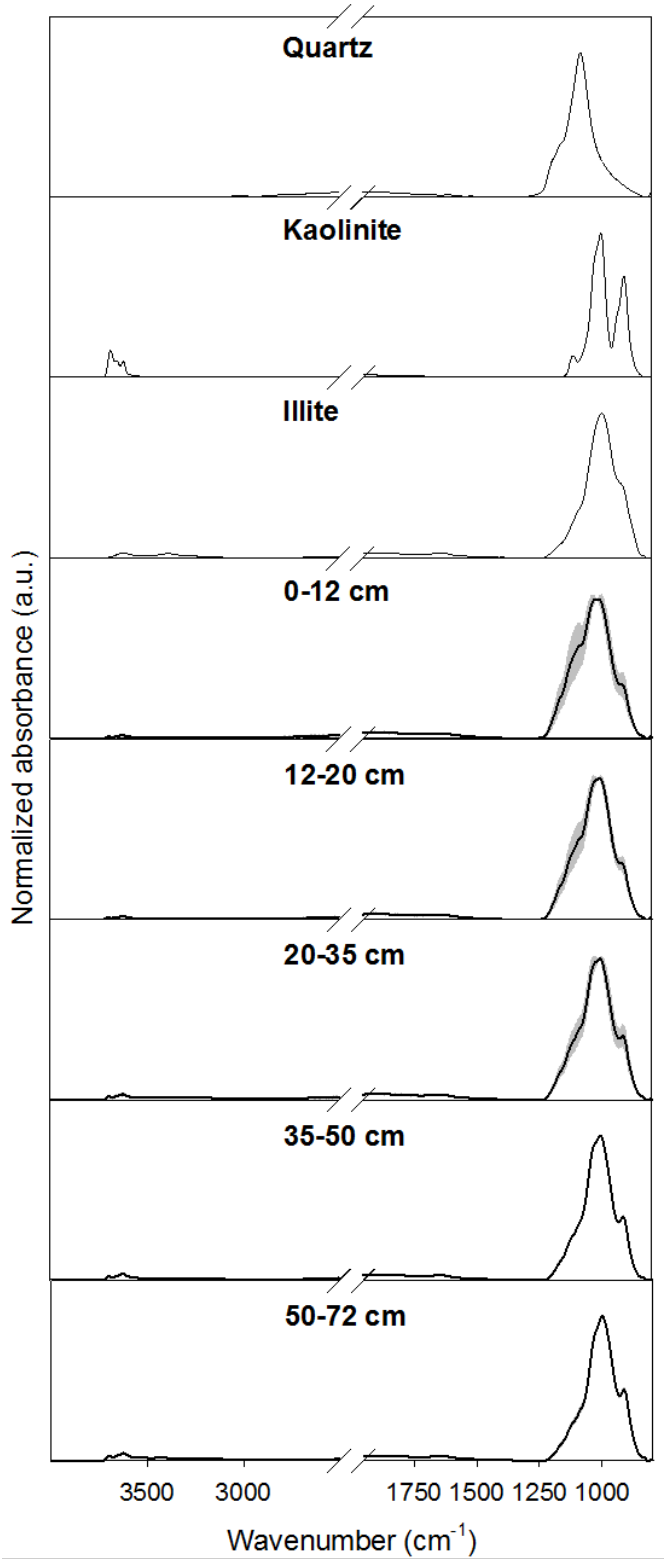

Figure A1.4 FTIR spectra of bulk NT soils

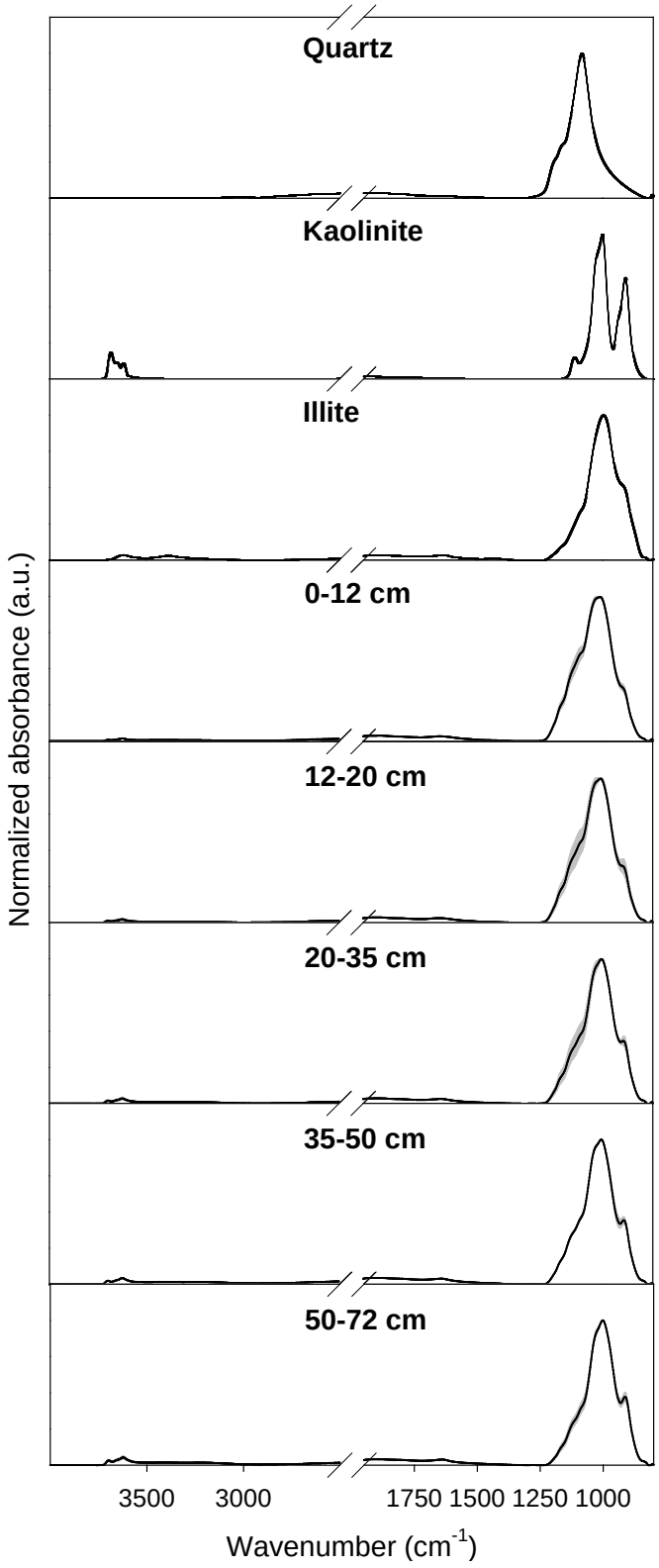

Figure A1.5 Carbon XANES spectra for individual replicates from MB (top) and NT (bottom) soils

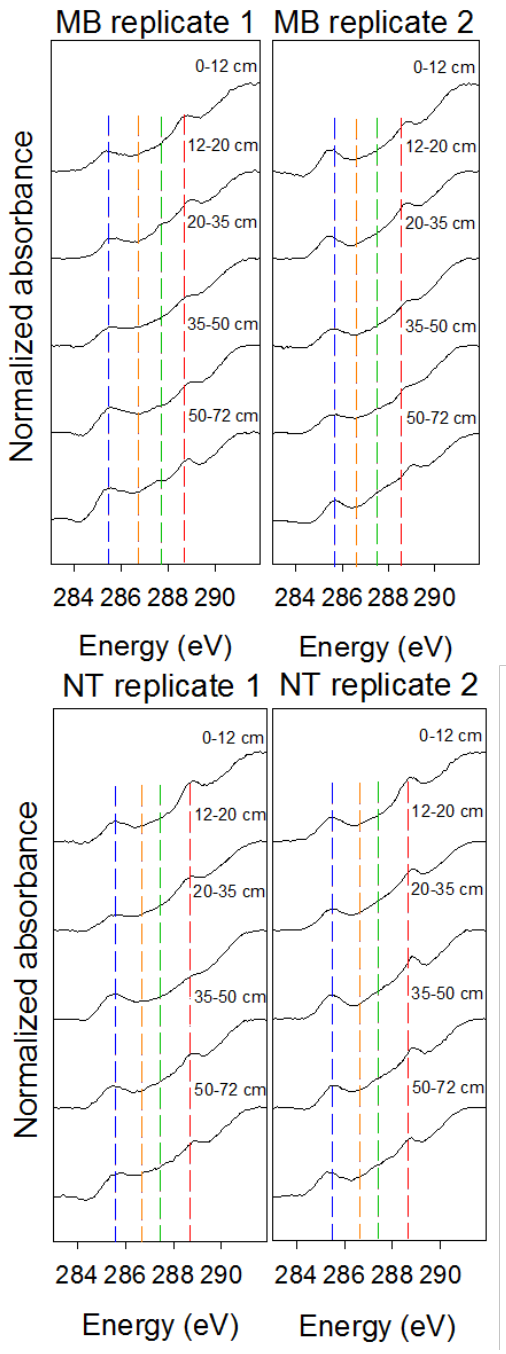

Figure A1.6 Fluorescence EEMs of DOM from all MB replicates

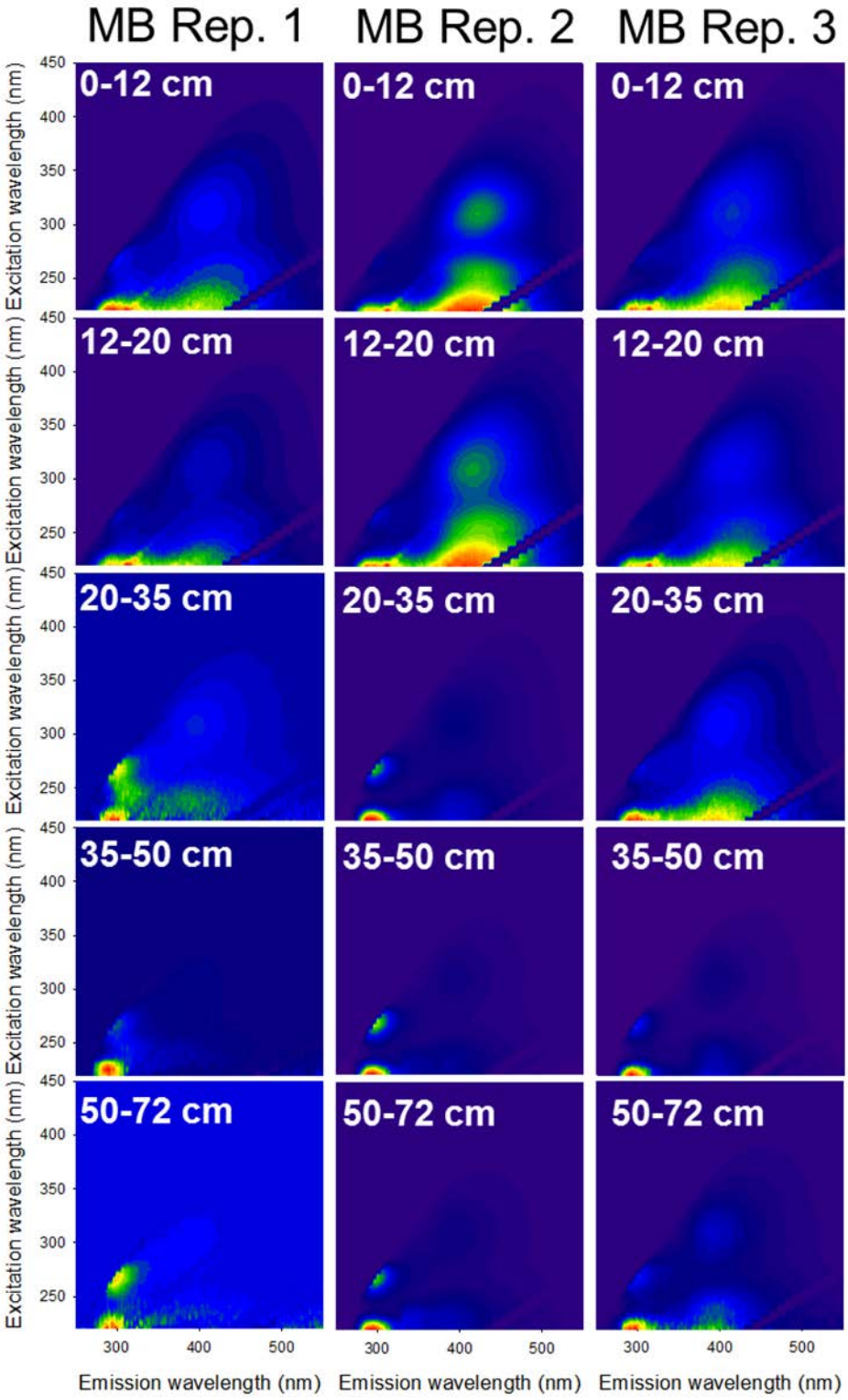

Figure A1.7 Fluorescence EEMs of DOM from all NT replicates

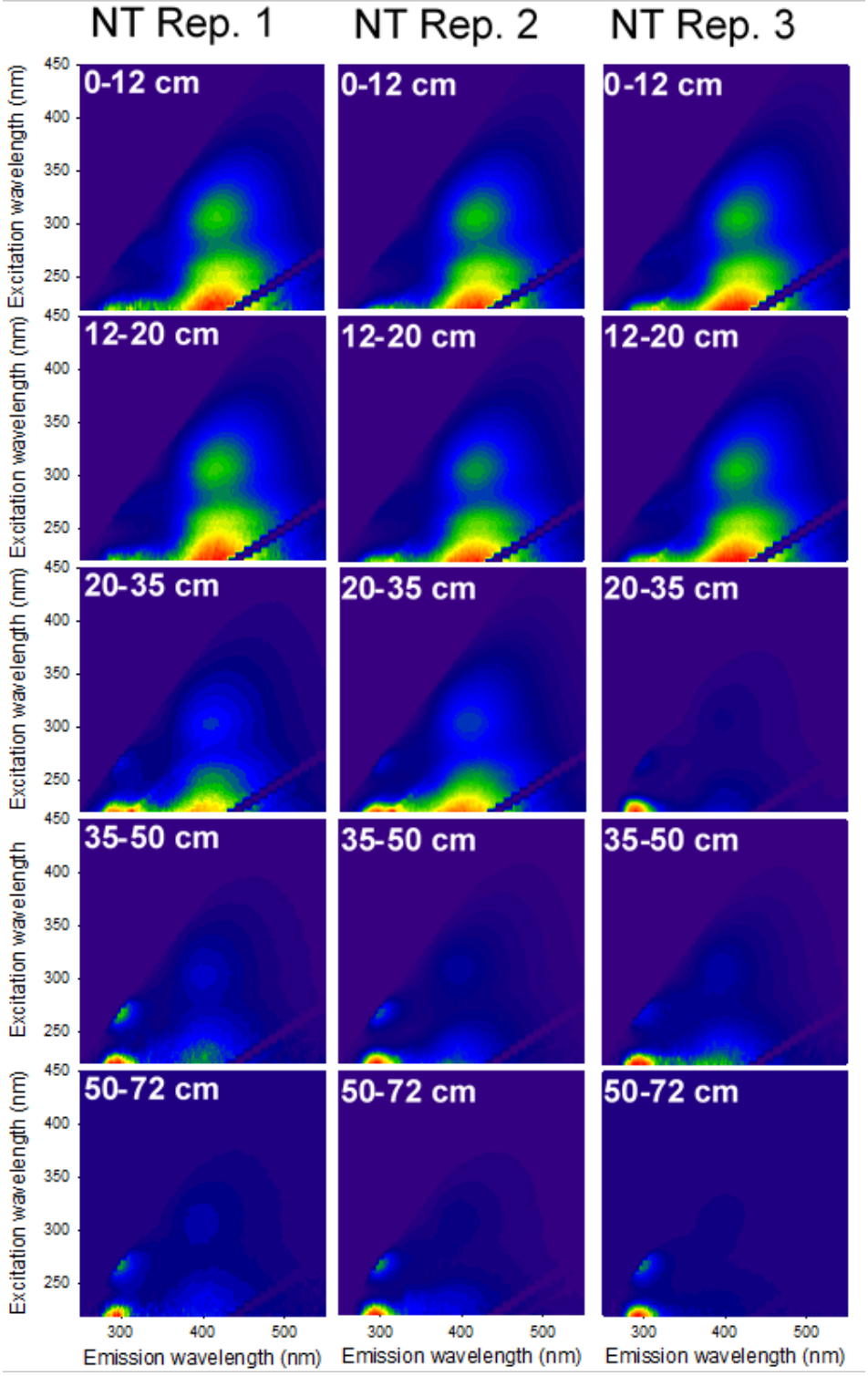

Figure A2.1 FTIR spectrum of cleaned SWy-2 bentonite used in ATR-FTIR experiments

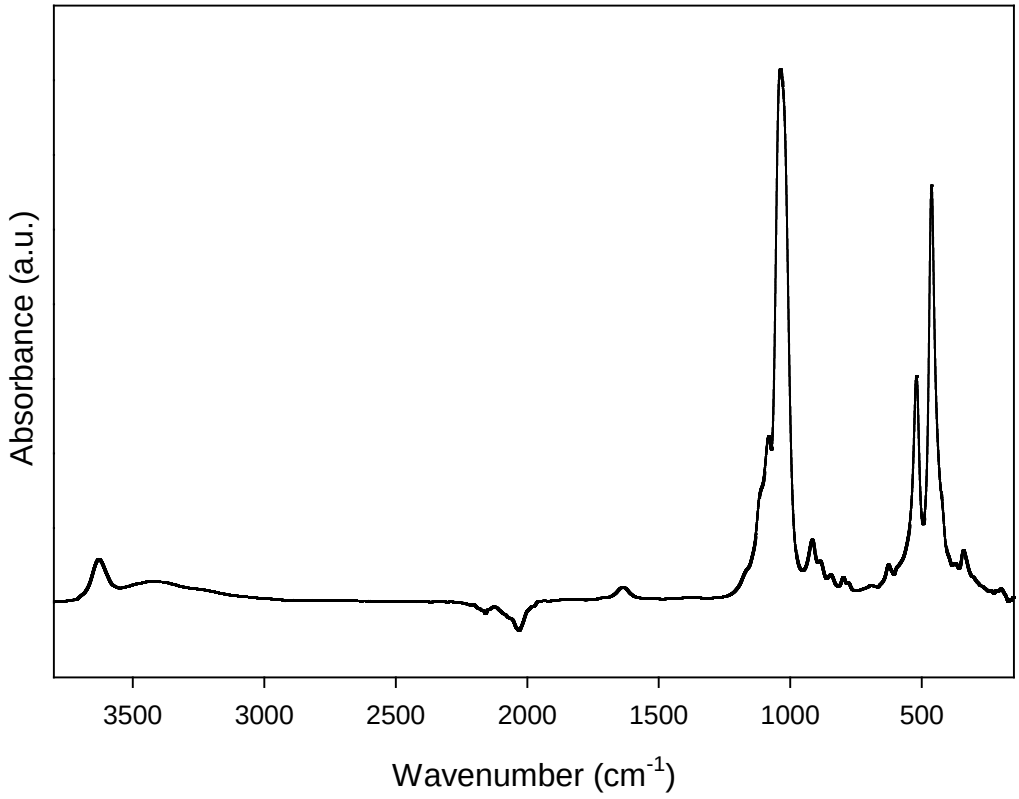

Figure A2.2 FTIR spectra from an adsorption experiment ([BSA] = 15.0 µM). Shown spectra were collected at ≈20 minute intervals from t = 3 minutes until t =120 minutes. The red line represents the FTIR spectrum of 15.0 µM BSA over a bare diamond IRE.

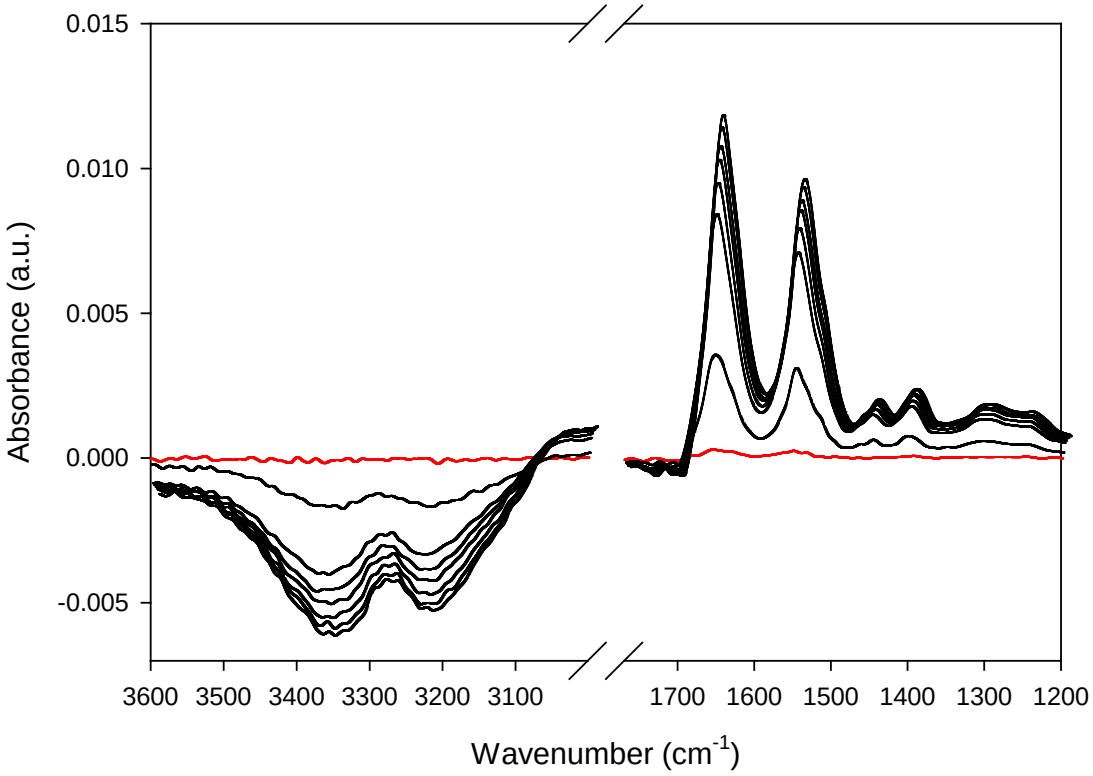

Figure A2.3 Elovich rate plot (q_t vs. ln(t)) for each experimental BSA concentration. [BSA] = 1.50 (yellow squares), 3.75 (red x), 7.50 (green circles) and 15.0 µM (orange triangles). Linear regression for each set is shown as solid line of corresponding color.

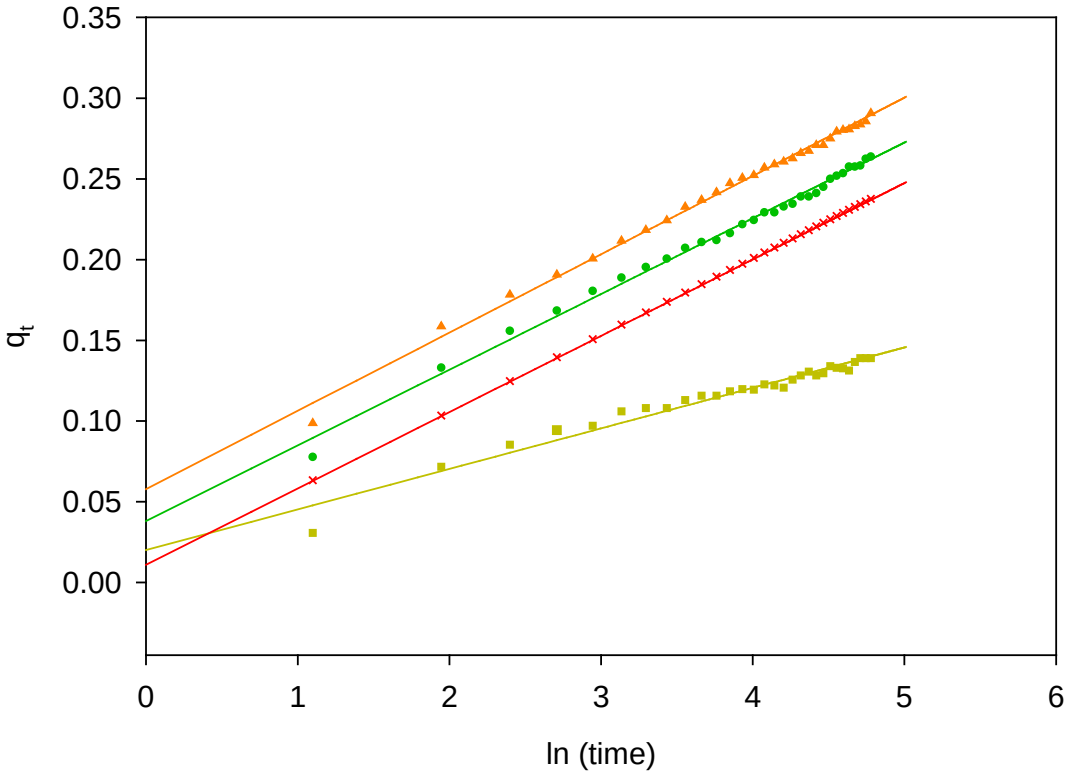

Figure A2.4 Pseudo-first order rate plot ($\ln(q_e-q_t)$ vs. t) for each experimental BSA concentration. [BSA] = 1.50 (yellow squares), 3.75 (red x), 7.50 (green circles) and 15.0 µM (orange triangles). Linear regression for each set is shown as solid line of corresponding color.

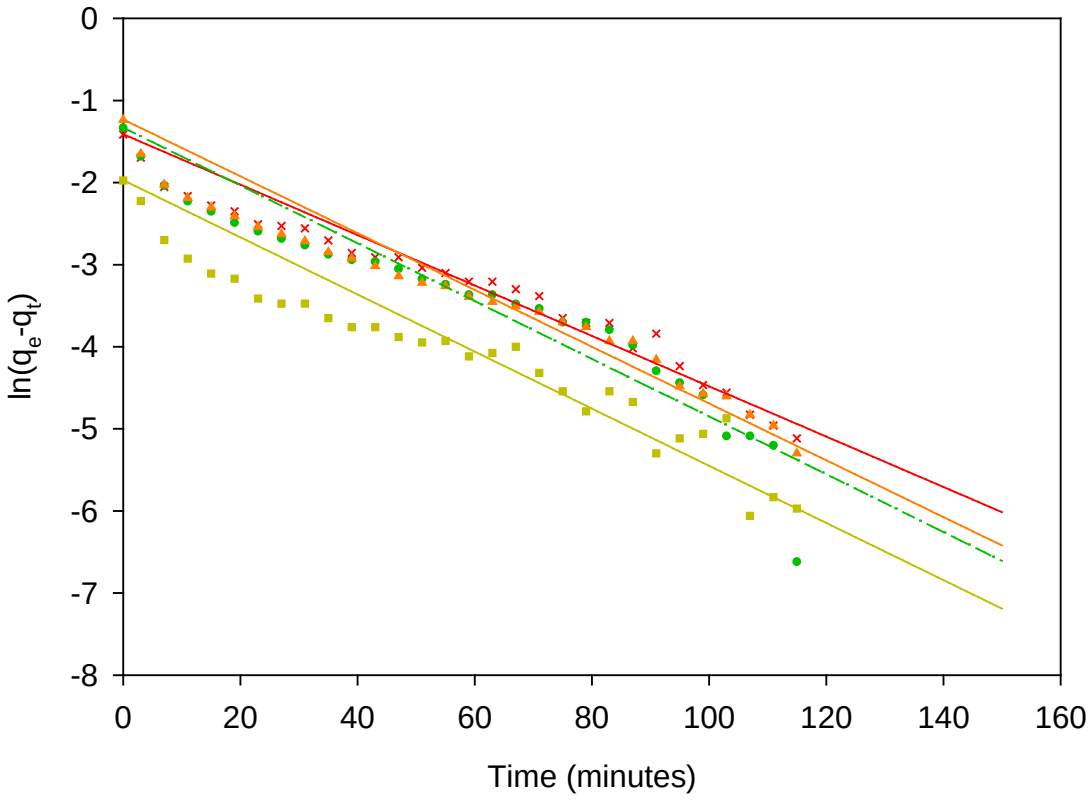

Figure A2.5 Pseudo-second order rate plot (t/q_t vs. t) for each experimental BSA concentration. [BSA] = 1.50 (yellow squares), 3.75 (red x), 7.50 (green circles) and 15.0 µM (orange triangles). Linear regression for each set is shown as solid line of corresponding color.

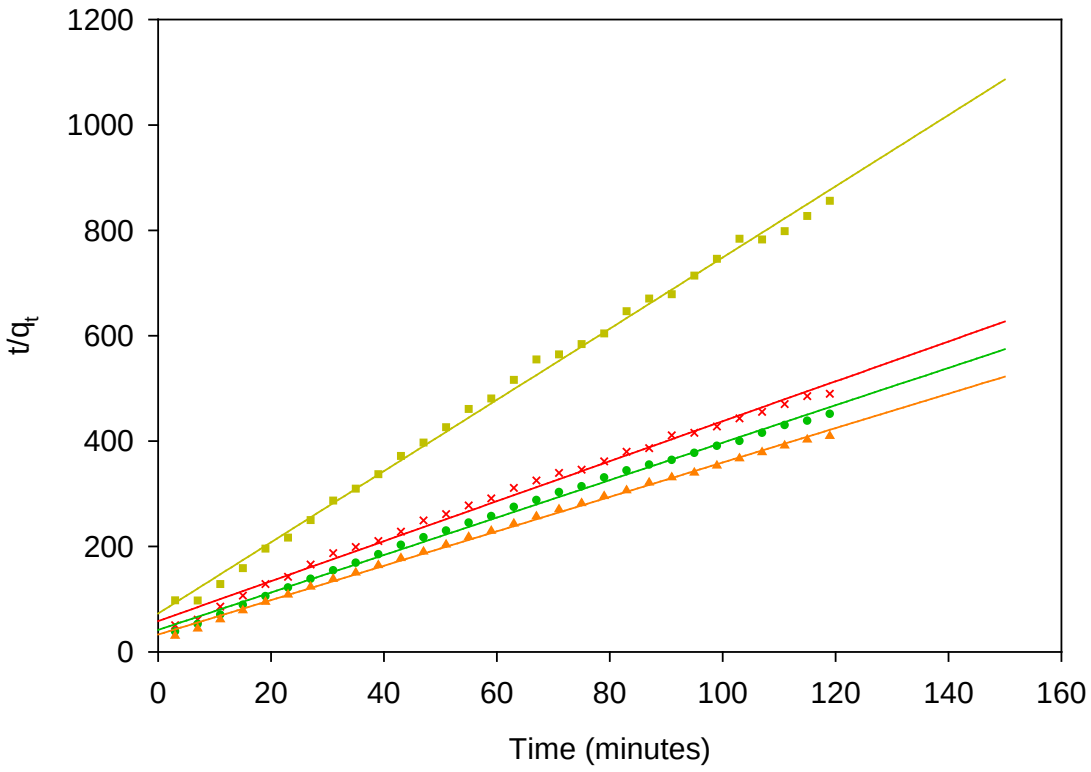

Figure A2.6 Intraparticle diffusion rate plot (q_t vs. $\sqrt{t}$) for each experimental BSA concentration. [BSA] = 1.50 (yellow squares), 3.75 (red x), 7.50 (green circles) and 15.0 µM (orange triangles). Linear regression for each set is shown as solid line of corresponding color.

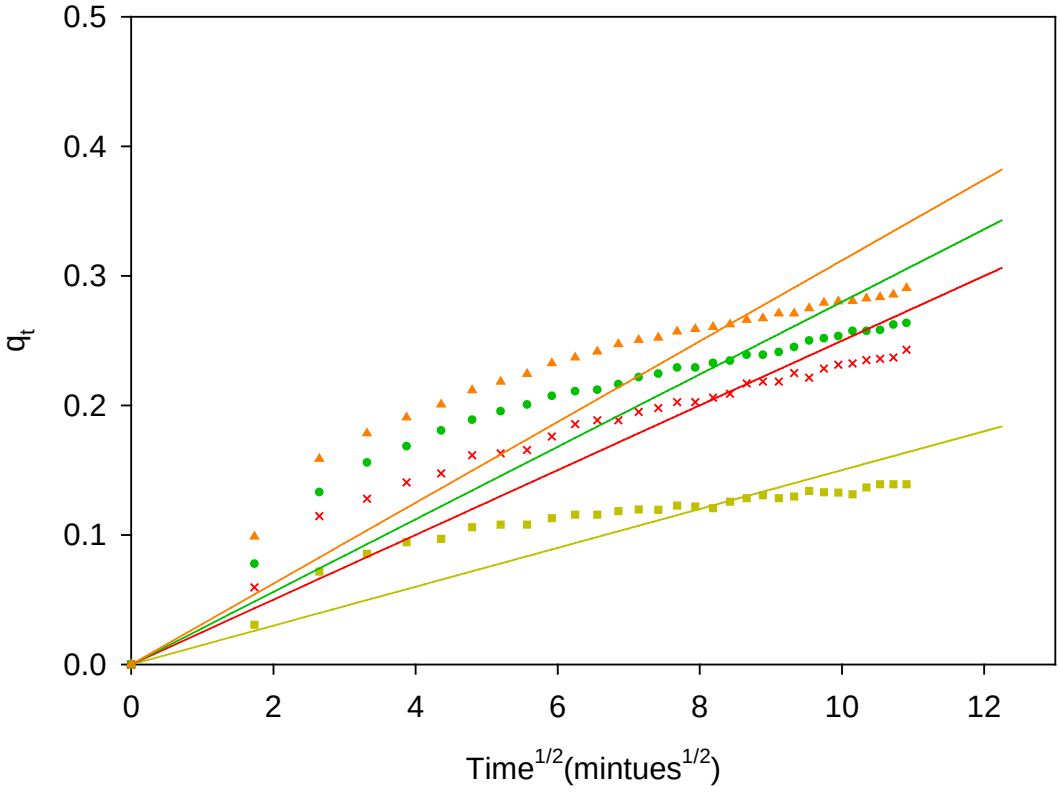

Figure A2.7 a) Synchronous 2D-COS plot for [BSA] = 1.50 µM with corresponding autocorrelation spectrum and labelled peaks in the amide I band. Legend presents correlation values.

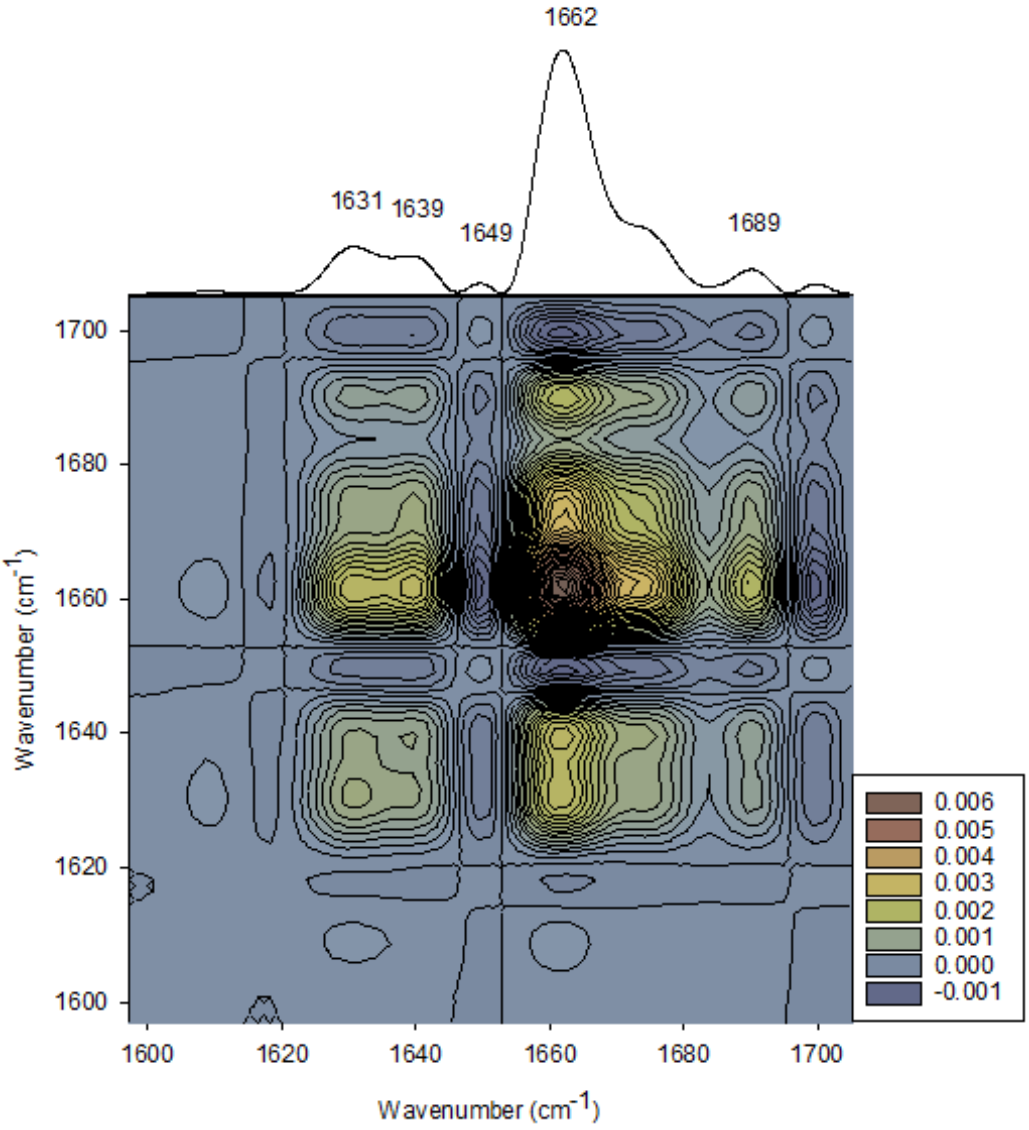

Figure A2.7 b) Asynchronous 2D-COS plot for [BSA] = 1.50 µM. Correlation values are shown in the legend.

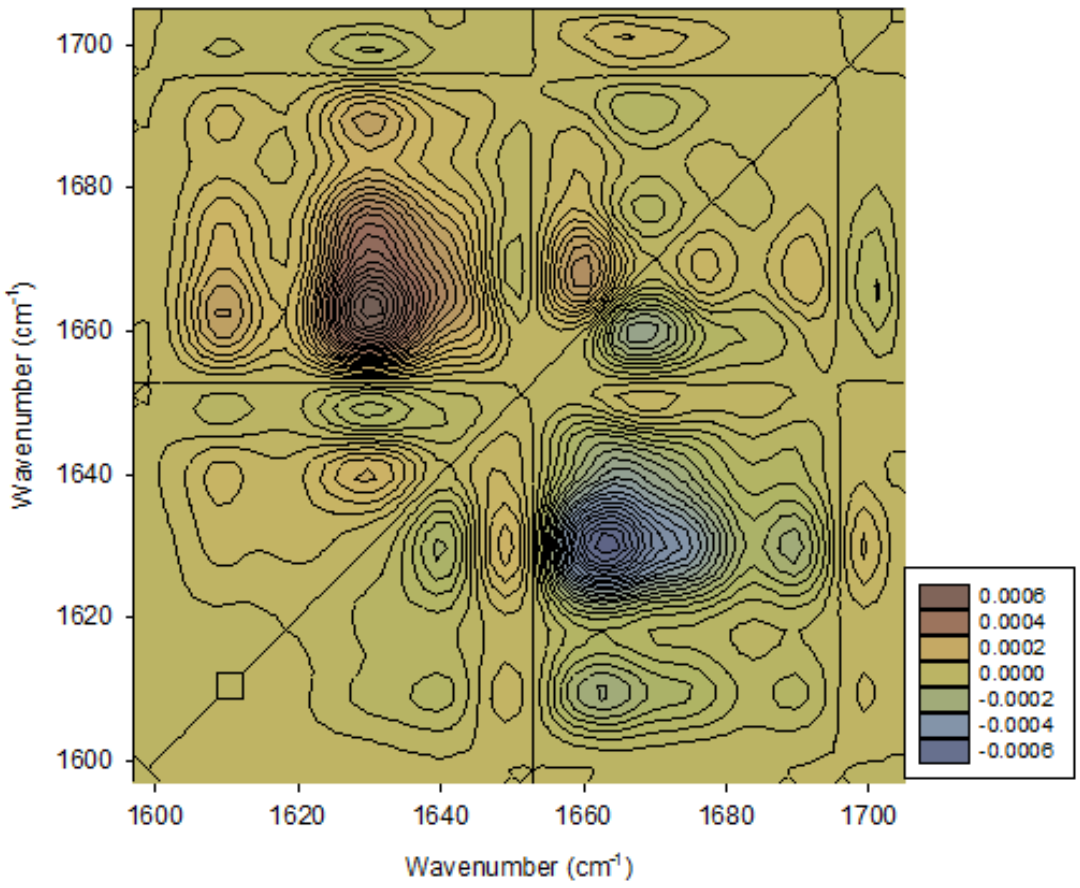

Figure A2.8 a) Synchronous 2D-COS plot for [BSA] = 7.50 µM with corresponding autocorrelation spectrum and labelled peaks in the amide I band. Legend presents correlation values.

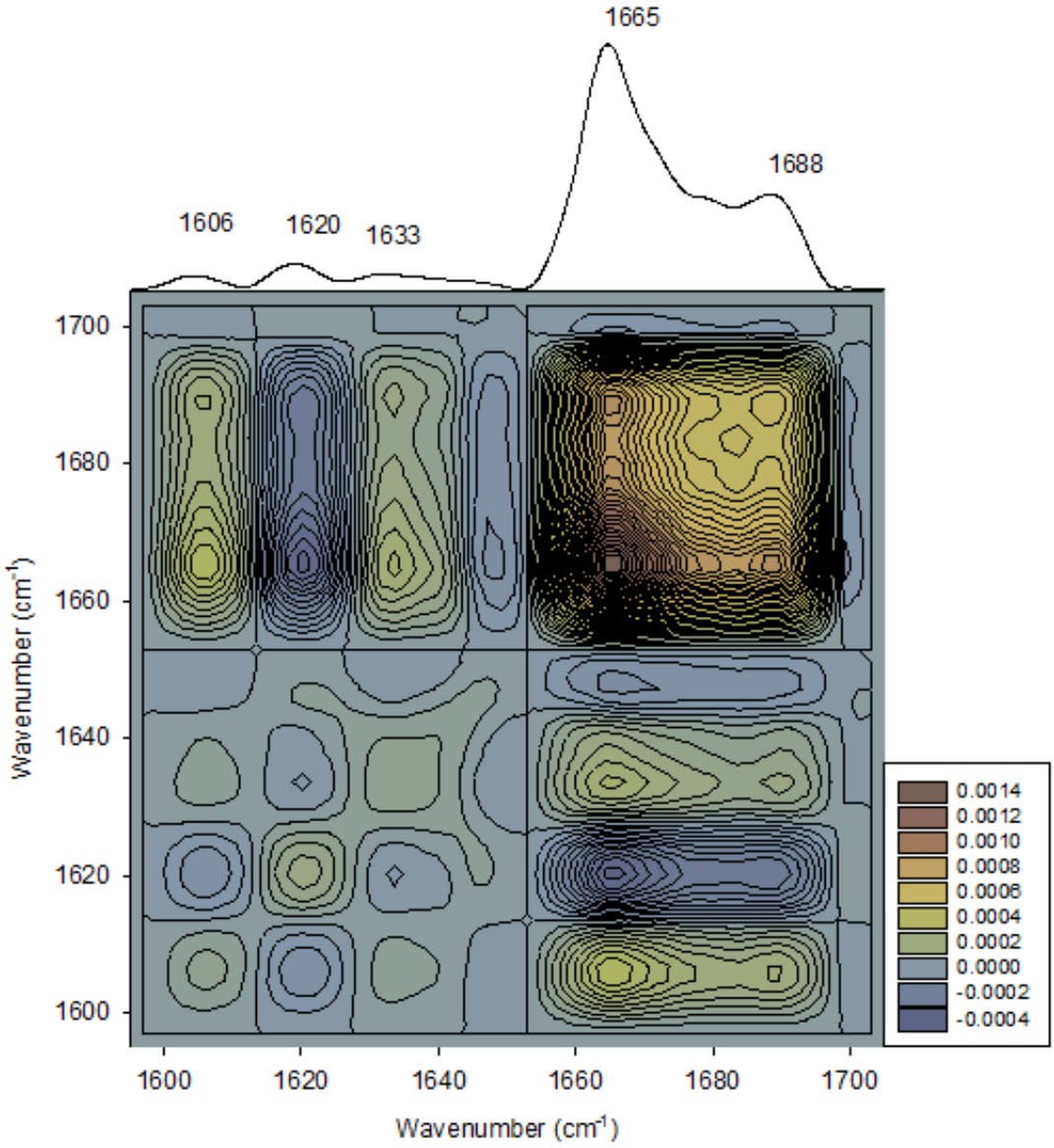

Figure A2.8 b) Asynchronous 2D-COS plot for [BSA] = 7.50 µM. Correlation values are shown in the legend.

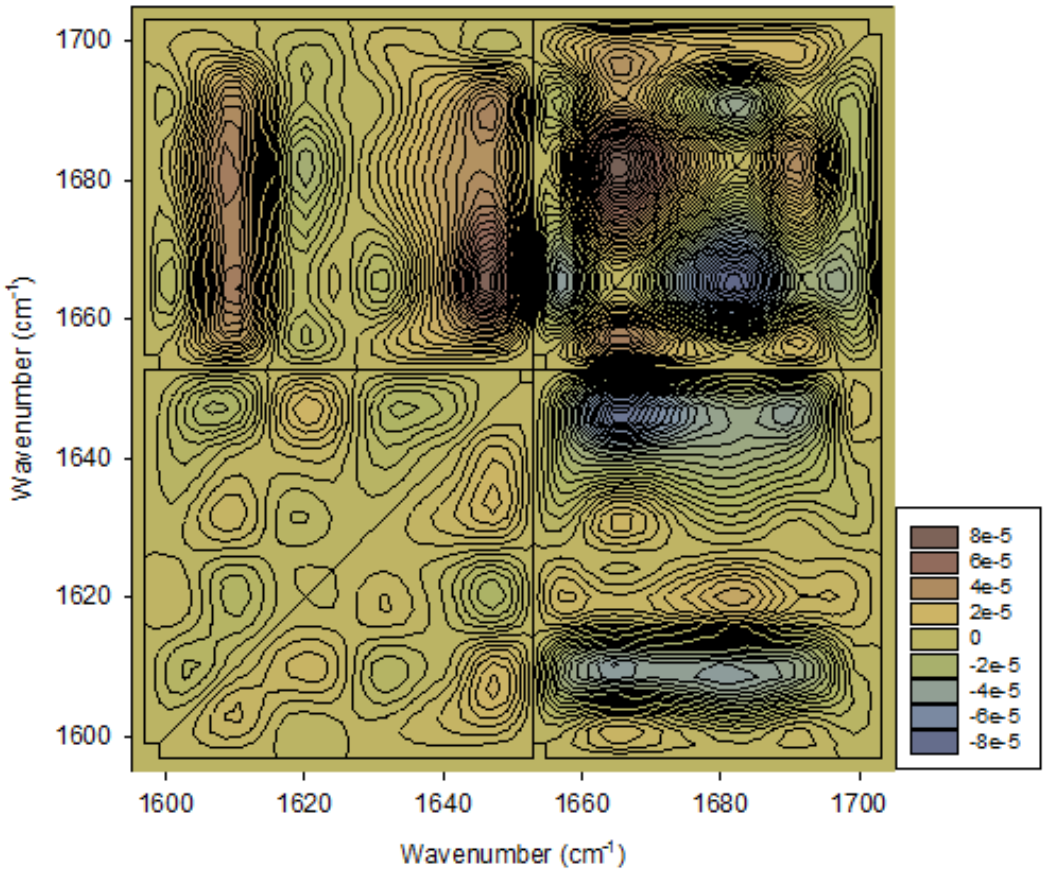

Figure A2.9 a) Synchronous 2D-COS plot for [BSA] = 15.0 µM with corresponding autocorrelation spectrum and labelled peaks in the amide I band. Correlation values are shown in the legend.

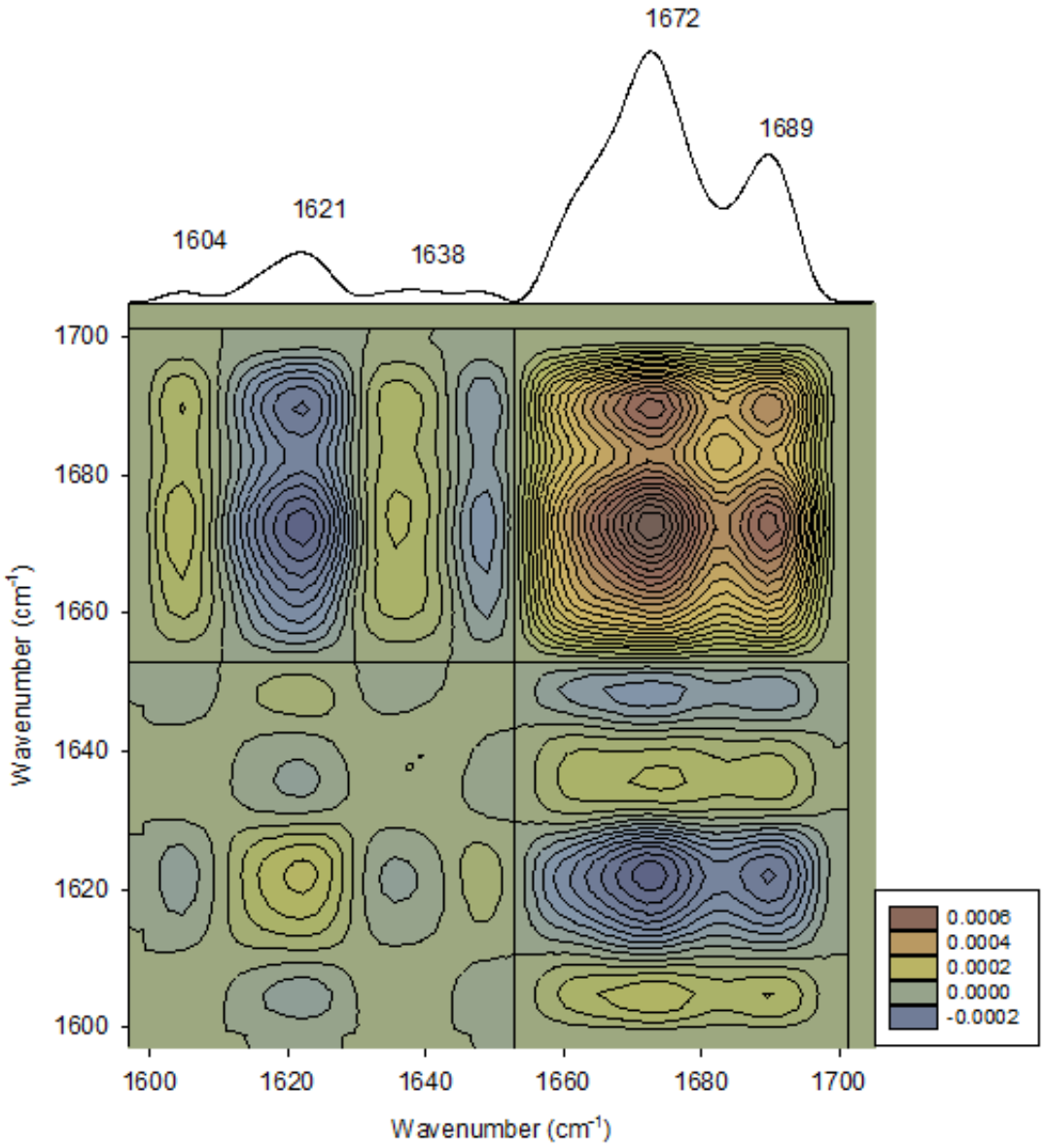

Figure A2.9 b) Asynchronous 2D-COS plot for [BSA] = 15.0 µM. Correlation values are shown in the legend.

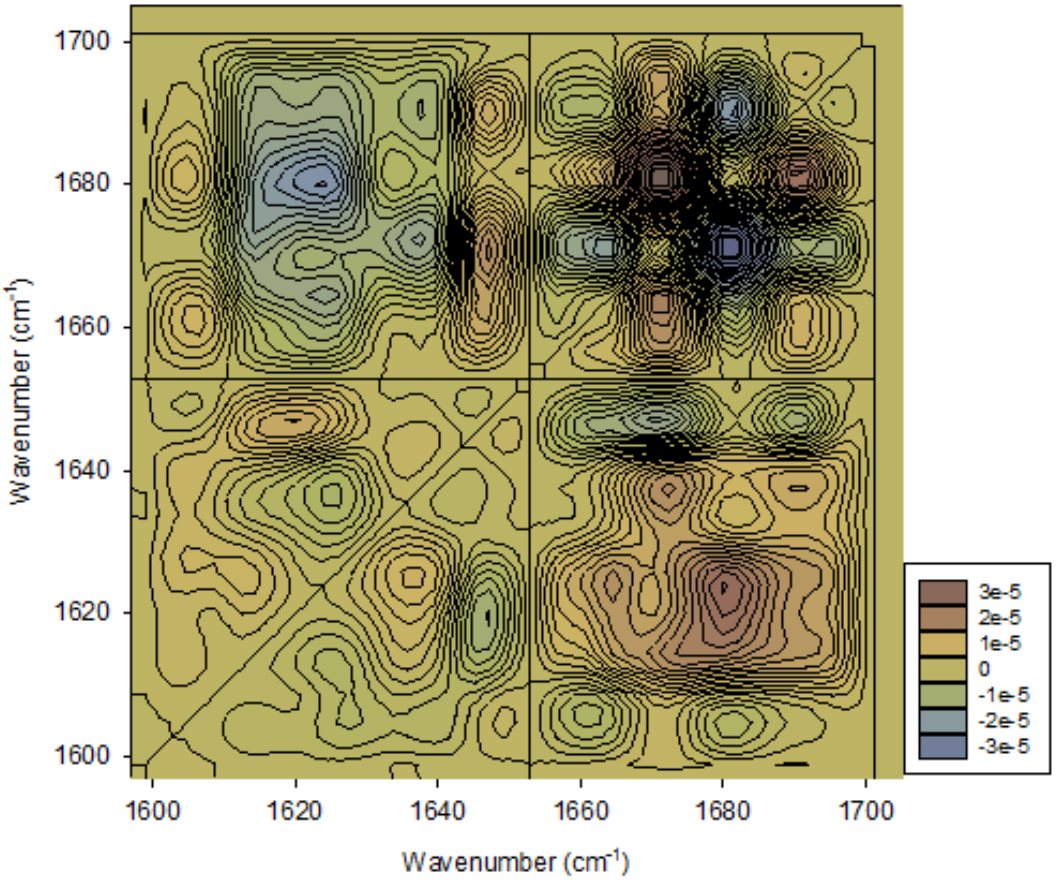

Figure A3.1 Image of 1.5% agarose gel electrophoresis of DNA sheared from 0 to 6 minutes. Far left lane represents a 2 log ladder and far right represents a 100 bp ladder. Pulse time increases from second lane from left to second lane from right in 30 second pulses. The last point represents the size of DNA used in studies.

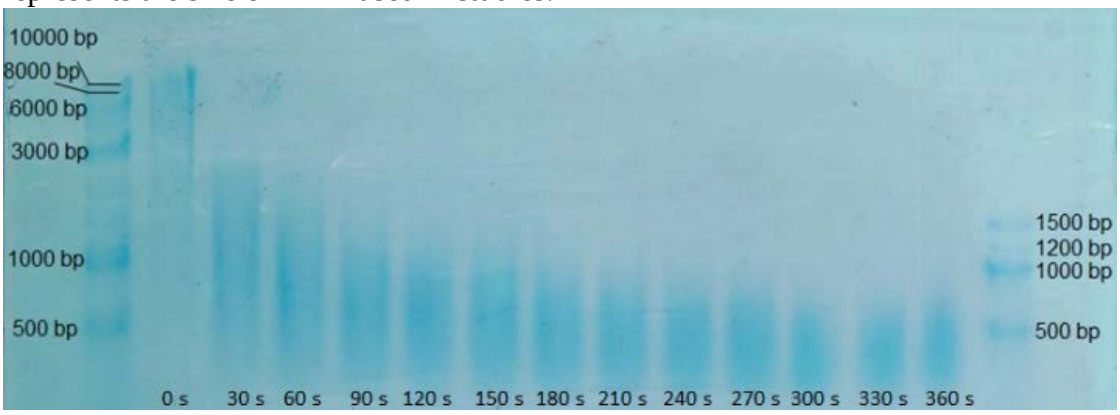

Figure A3.2 FTIR spectrum of synthetic goethite used in adsorption experiments, showing the prominent ν O-H mode (3132 cm^{-1}) and ν Fe-O modes (895 and 794 cm^{-1}) used for normalization of DNA ν C-C signal (895 cm^{-1}).

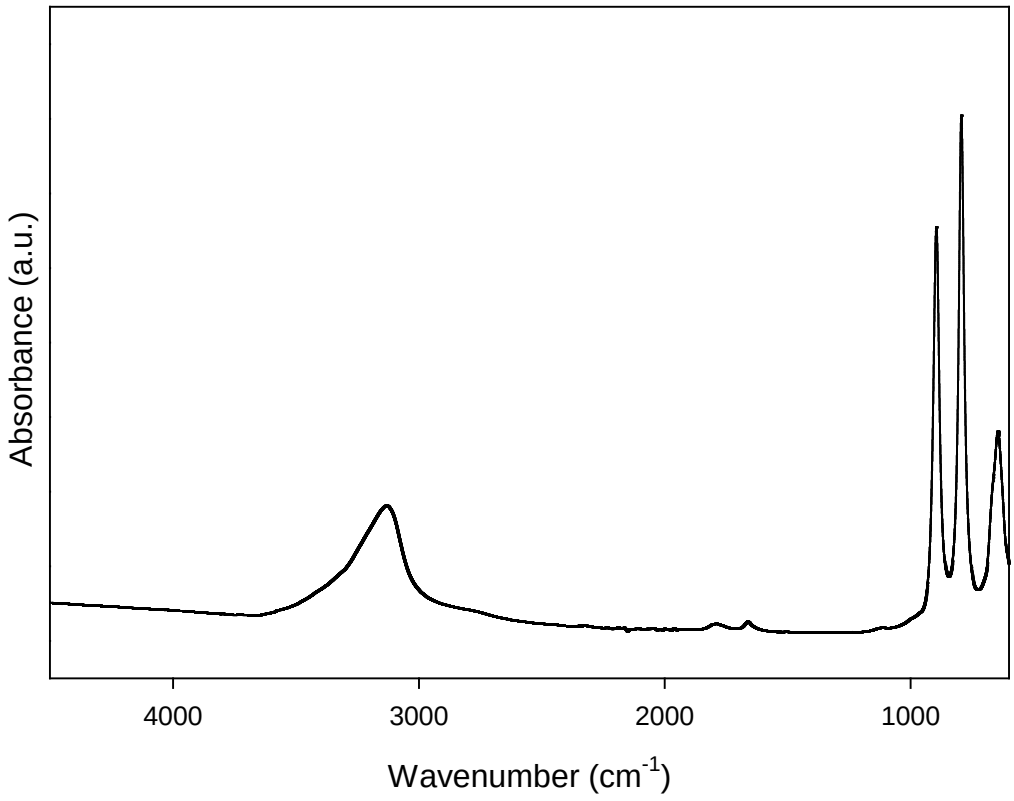

Figure A3.3 XPS survey scans for goethite and DNA/goethite at all experimental equilibrium DNA concentrations. DNA concentrations shown are in units of mg/mL.

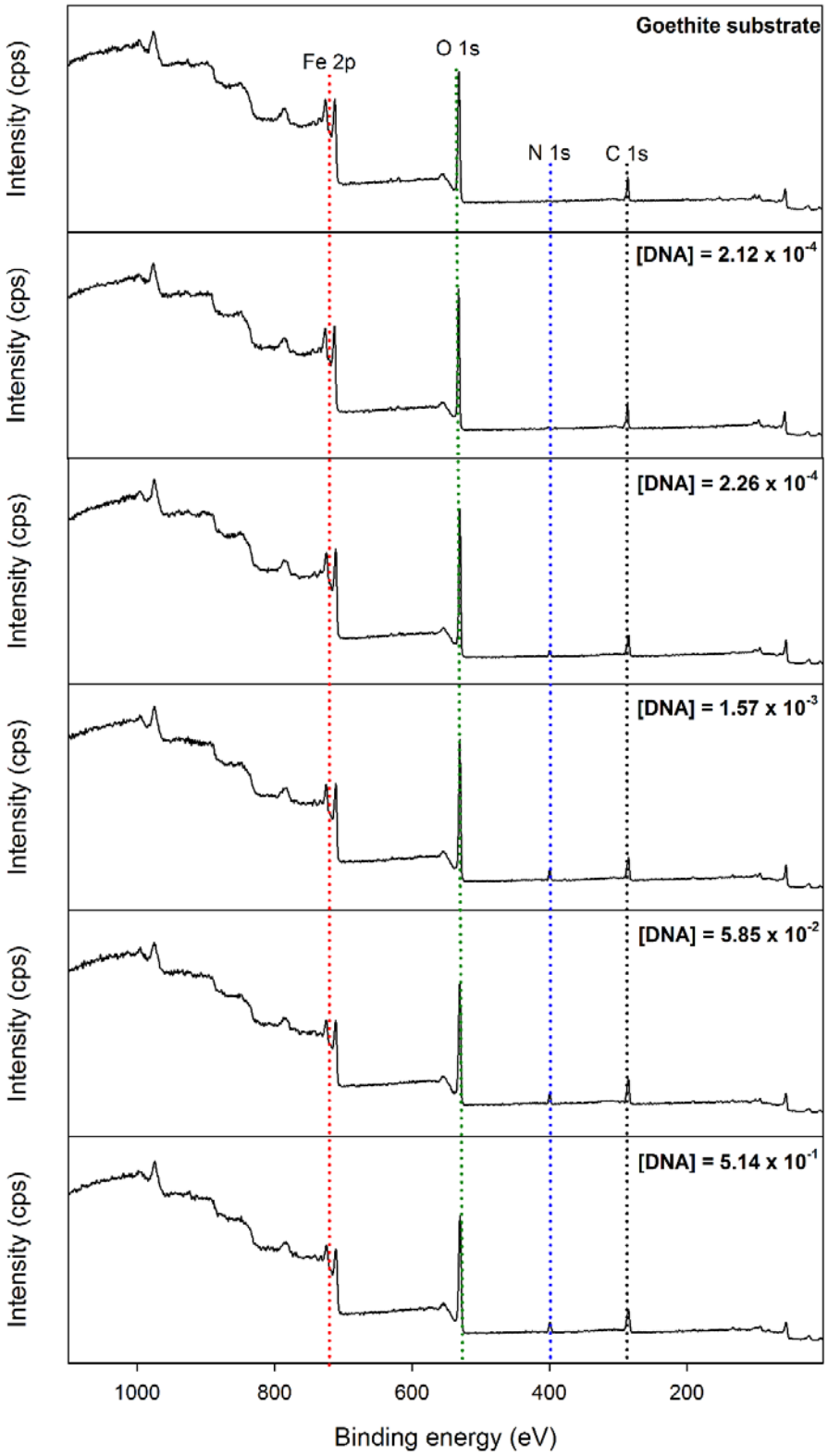

Figure A3.4 Adsorption kinetics for additional experimental DNA concentrations with corresponding pseudo-first order adsorption models (solid lines), including 0.0025 (orange squares) 0.01 (green circles) and 0.1 (blue upside down triangles) mg/mL DNA.

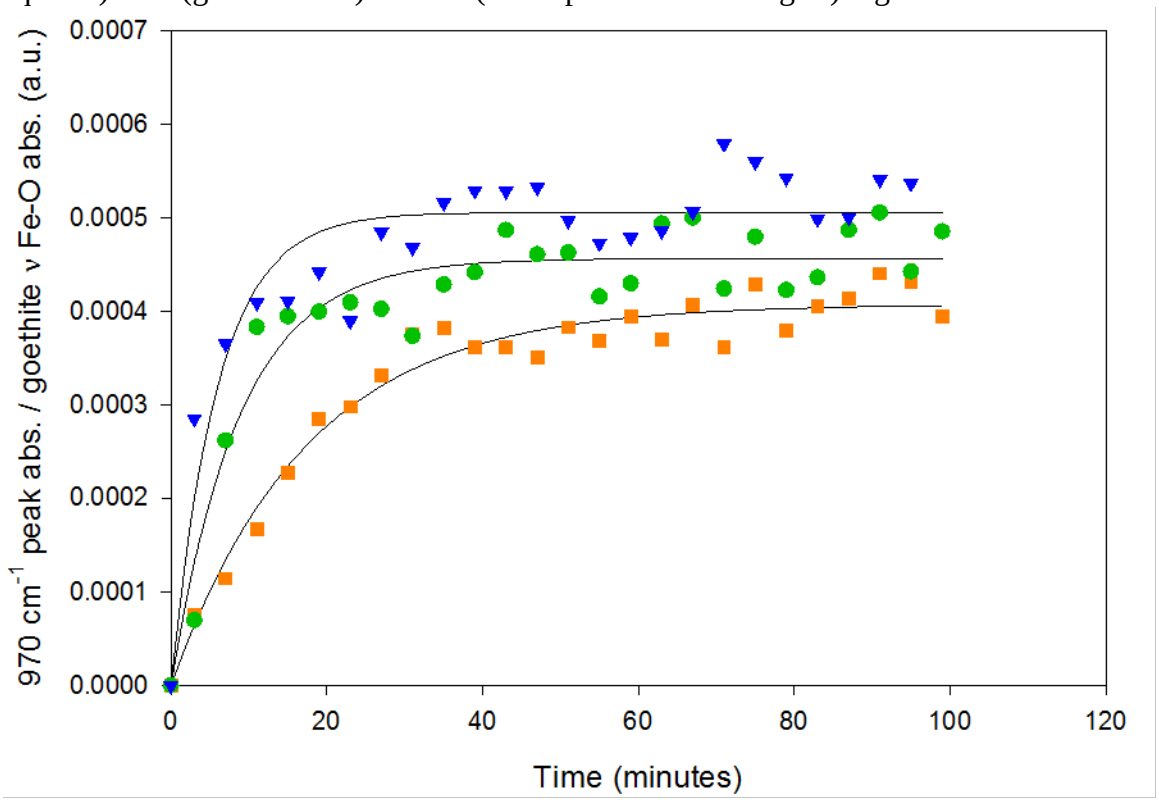

Figure A3.5 High resolution N 1s (left) and P 2p (right) spectra for goethite, DNA and DNA adsorbed on goethite at experimental equilibrium DNA concentrations. Concentrations shown are in units of mg/mL.The lowest value ([DNA] = 2.12 x x10^{-4}) was omitted due to low N and P signals. Dashed vertical lines show peak position of DNA standard.

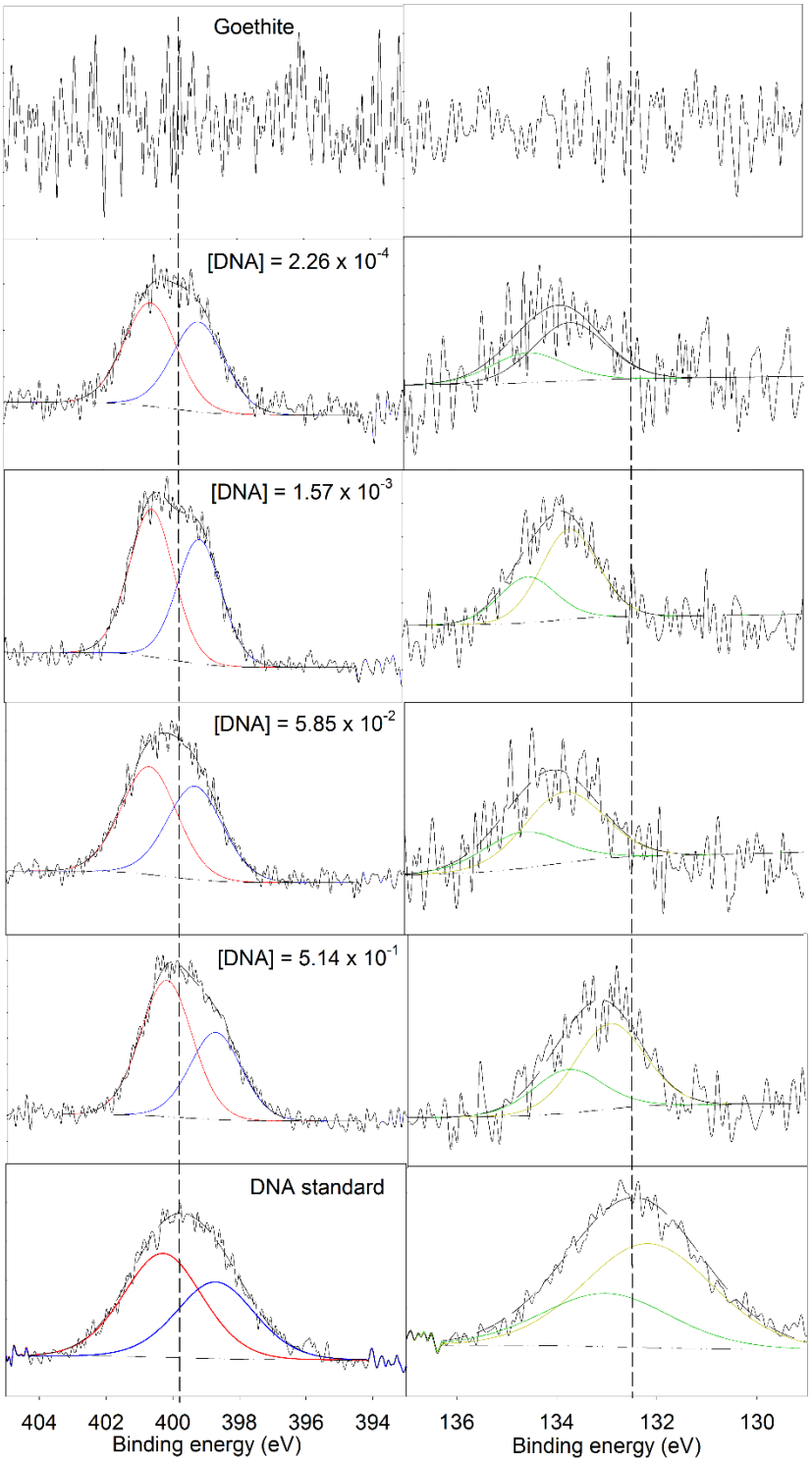

Figure A4.1 Binding curve from circular dichroism studies showing Hill (red) and Langmuir (green) model fits.

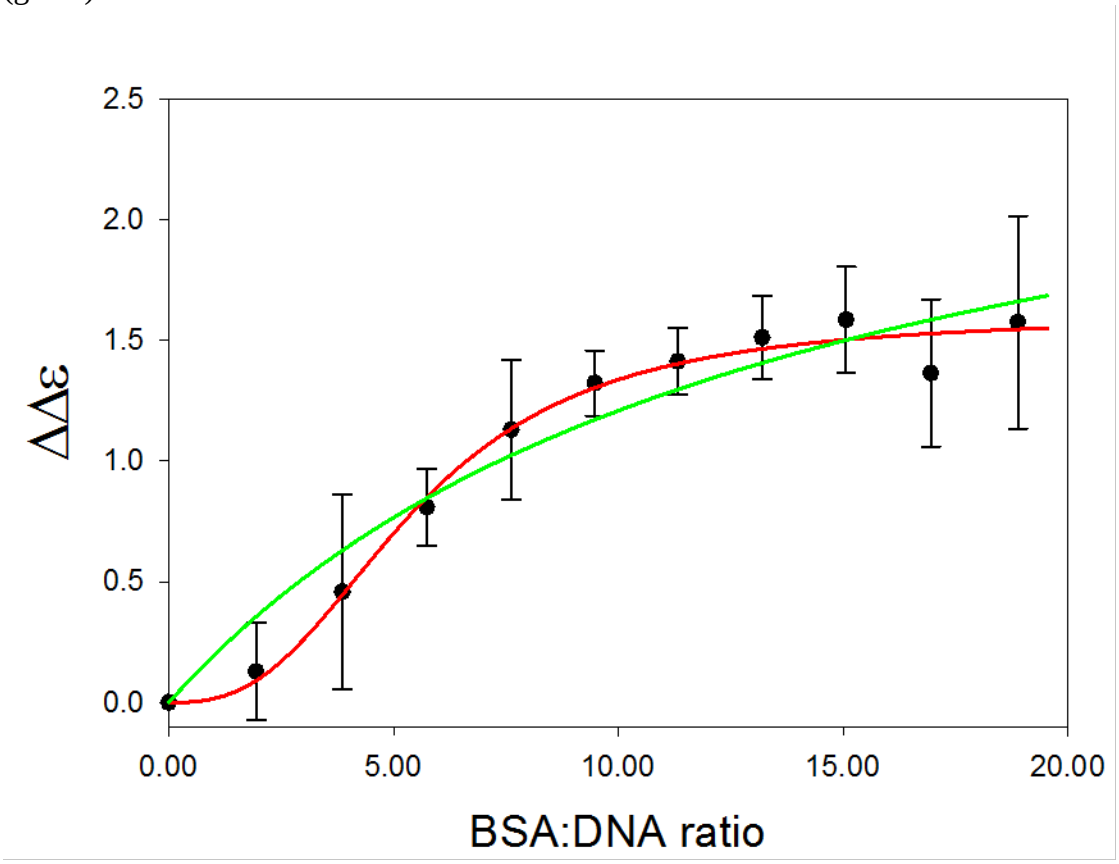

Figure A4.2 ATR-FTIR spectra of BSA and DNA in solution, adsorbed on goethite and adsorbed on goethite as DNA/BSA complexes at all BSA:DNA ratios at equilibrium. For peak assignments, see main text (**Figure 4.3**)

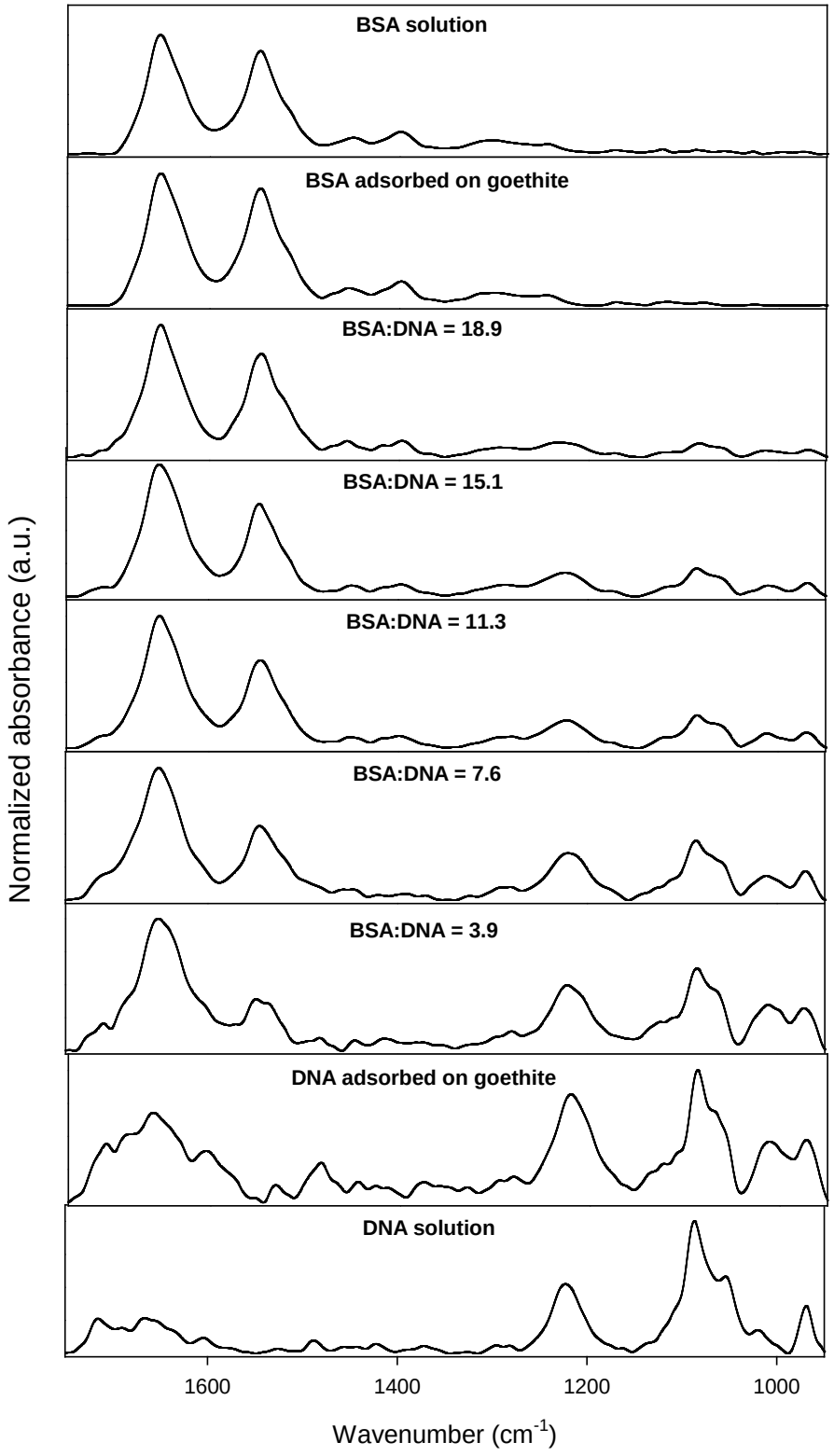

Figure A4.3 ATR-FTIR spectra of biomolecules adsorbed on goethite at 3 (red), 7 (grey), 23 (orange), 67 (green) and 99 (blue) minutes at BSA:DNA ratio of 7.6. Inset shows BSA amide II (red circles) and DNA ν C-C (blue circles) peak heights at time points for shown experiment.

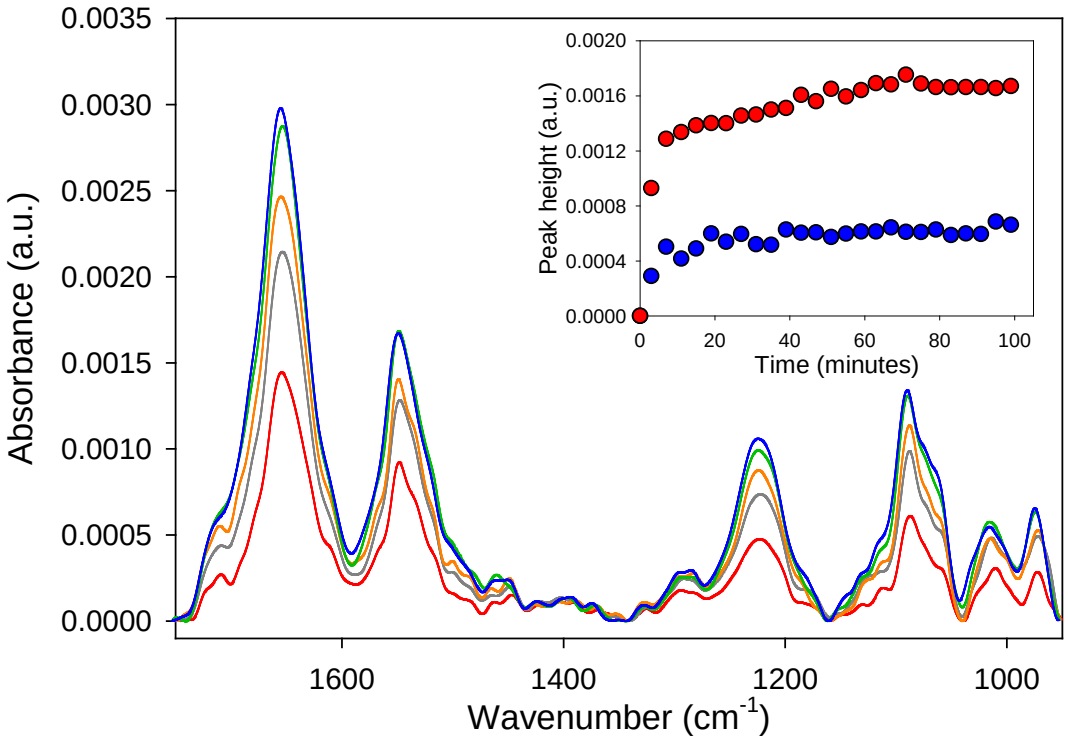

Table A1.2 Tentative peak assignments of organic functional groups and inorganic species in the < 0.2 µm water extractable fraction.

Peak Position (wavenumber (cm^{-1}))	Peak assignment
3350	ν O-H
2930	ν_{as} CH_2
2855	ν_s CH_2
1660-1630	Amide/ketone ν C=O
1600	ν_{as} COO^-/ ν C=C
1415	ν_s COO^-
1355	ν N-O (NO_3^-)
1100	ν S-O (SO_4^{2-})/ ν C-O
1040	ν C-C/C-O

Table A2.1 Pseudo-first order model parameters for each experimental concentration.

Concentration (μM)	k_1 (min^{-1})	RMSE
1.50	0.0274	1.64×10^{-2}
3.75	0.0271	2.37×10^{-2}
7.50	0.0311	2.83×10^{-2}
15.0	0.0282	3.56×10^{-2}

Table A2.2 Pseudo-second order model parameters for each experimental concentration

Concentration (µM)	k_2 (min^{-1})	q_e	h (min^{-1})	RMSE
1.50	0.627	0.148	0.0137	4.38×10^{-3}
3.75	0.246	0.264	0.0171	9.34×10^{-3}
7.50	0.303	0.281	0.0239	8.99×10^{-3}
15.0	0.323	0.306	0.0302	9.64×10^{-3}

Table A2.3 Intraparticle diffusion model parameters for each experimental concentration**.**

Concentration (μM)	k_d (a.u. $min^{-1/2}$)	RMSE
1.50	0.0150	1.98×10^{-2}
3.75	0.0250	2.49×10^{-2}
7.50	0.0280	3.43×10^{-2}
15.0	0.0312	4.13×10^{-2}

Table A3.1 FTIR peaks (cm^{-1}) and assignments for DNA in solution and DNA adsorbed onto goethite.

DNA solution	Adsorbed DNA	Assignment	Reference
1716	1712	ν C=O guanine	28
1667	1663	ν C=O thymine	28, 29
1605	1605	ν C=N, ν C=C nucleobase rings	28
1489	1485	δ CH and CH_2, CH_3 scissoring	29
1224	1218	ν_{as} backbone PO_4^-	28
1088	1087	ν_s backbone PO_4^-	28
	1068	ν Fe-O-P	46
1055	1055	Backbone ν C-O	28
1021	1021	Furanose vibration	28
	1010	ν Fe-O-P	30,31,46
970	970	Backbone ν C-C	28

Table A3.2 Pseudo-first order kinetic parameters for each experimental concentration.

DNA concentration (mg/mL)	A_{max} (a.u.)	Standard Error	k_1 (min^{-1})	Standard Error	R^2
0.001	3.60×10^{-4}	1.65×10^{-5}	0.0329	0.0042	0.926
0.0025	4.07×10^{-4}	6.93×10^{-6}	0.0571	0.004	0.968
0.005	4.04×10^{-4}	6.16×10^{-6}	0.0649	0.0045	0.969
0.01	4.56×10^{-4}	8.38×10^{-6}	0.114	0.0131	0.921
0.05	4.75×10^{-4}	6.26×10^{-6}	0.170	0.0176	0.940
0.1	5.06×10^{-4}	9.79×10^{-6}	0.168	0.0248	0.867
0.5	5.14×10^{-4}	9.46×10^{-6}	0.355	0.0748	0.845

Table A3.3 Langmuir isotherm parameters derived from non-linear fitting of experimental isotherms of FTIR and XPS data.

	FTIR	XPS
K (mL/mg)	1.25×10^{3}	9.48×10^{2}
Maximum adsorption	5.28×10^{-4} (a.u.)	0.714 (%N / %Fe)
RMSD (θ)	0.0504	0.0551

Table A3.4. Component parameters from high resolution N 1s (a) and P 2p (b) XPS spectra for each experimental surface coverage and DNA standard.

a)

Equilibrium DNA concentration (mg/mL)	Component 1 BE (non-conjugated – NH-, saturated N)	Component 1 (area %)	Component 2 BE (conjugated N)	Component 2 (area %)
2.26×10^{-4}	400.6	53.5	399.2	46.5
1.57×10^{-3}	400.6	54.3	399.2	45.7
5.85×10^{-2}	400.7	53.6	399.3	46.4
5.14×10^{-1}	400.2	61.0	398.8	39.0
N/A (standard)	400.3	57.5	398.7	42.5

b)

Equilibrium DNA concentration (mg/mL)	Component 1 BE (P 2p 1/2)	Component 1 (area %)	Component 2 BE (P 2p 3/2)	Component 2 (area %)
2.26×10^{-4}	134.5	50.0	133.7	50.0
1.57×10^{-3}	134.5	50.0	133.7	50.0
5.85×10^{-2}	134.6	50.0	133.8	50.0
5.14×10^{-1}	133.8	50.0	132.9	50.0
N/A (standard)	133.0	50.0	132.2	50.0

Table A4.1 Model parameters for Hill and Langmuir fitting of DNA-BSA binding curve from circular dichroism studies. Associated errors are shown in parentheses.

Model	K_d (μM)	n	$\Delta\Delta\varepsilon_{max}$	Standard Error of Estimate
Hill	2.11 (0.12)	2.71 (0.40)	1.60 (0.07)	0.07
Langmuir	5.28 (2.29)	N/A	2.87 (0.66)	0.15